Production of Hard Tissue Scaffolds Using Three-Dimensional Printing Method

by

Tamás Dávid Szűcs, MSc, MIEI

This thesis is submitted as the fulfilment for the
requirement of the award of degree of

MASTER OF ENGINEERING (MEng)

by research from

DUBLIN CITY UNIVERSITY

Supervisor: Dr. Dermot Brabazon

2008

I hereby certify that this material, which I now submit for assessment on the programme of study leading to the award of Master of Engineering is entirely my own work and has not been taken from the work of others save and to the extent that such work has been cited and acknowledged within the text of my own work.

Signed:_________________________ ID No.: 57100268

Date: 28/01/2009

Acknowledgements

Hereby I would like to acknowledge first of all to my supervisor, Dr. Dermot Brabazon for the his assistance and guidance during my work.

I would like to express my gratitute to Szilvia Eösöly whose patience, love, support, and constant presence helped me through this work.

Furthermore I would like to thank to my collegues in the NovelScaff team at DCU and to Dr. József Gábor Kovács and Dr Philip Reeves for their professional advice.

Also, I would like to thank to Mr. Michael Tyrrell, Mr. Michael May and Mr Chris Crouch for their technical assistance.

This research has been supported by a Marie Curie Early Stage Research Training Fellowship of the European Community's Sixth Framework Programme under contract number MEST-CT-2005-020621.

Abstract

Synthesised bone replacement scaffolds provide the possibility to individually tailor properties, overcome limited donor availability and improve osteointegration. The aim of bone tissue engineering is to provide solutions to these problems by making available high quality transplants that can be supplied in larger quantities. In these applications both the internal and external geometry of the scaffold are very important since they have significant effect on mechanical properties, permeability and cell proliferation. Rapid Prototyping technologies allow the use of customised materials with predetermined and optimised geometries to be fabricated with good accuracy. This work investigates the ability of the 3D printing technology to manufacture intricate bone scaffold geometries from biocompatible calcium phosphate based materials. Initial investigations with the proprietary materials showed that predicted directional mechanical behaviour can be realised. Practical measurements investigating the directional mechanical properties of the manufactured samples showed trends identical with the results of the Finite Element Analysis (FEA). The ability of 3D Printing technology to fabricate tissue engineering scaffold geometries made of biocompatible calcium phosphate cements was also demonstrated in this work. Scaffolds were manufactured by printing aqueous sodium phosphate dibasic solution on the powder bed consisting of a homogeneous mixture of dicalcium phosphate and calcium hydroxide. The wet-chemical reaction of precipitation took place in the powder bed of the 3D Printer. Solid specimens were manufactured in order to measure the bulk compressive mechanical properties of the fabricated Calcium Phosphate Cement (CPC). The average elastic modulus for the so produced parts was 3.59 MPa, and the average compressive strength was 0.147 MPa. Sintering resulted in significantly increased compressive properties ($E = 9.15$ MPa, $\sigma_y = 0.483$ MPa), but it decreased the specific surface area of the material. As a result of sintering, the calcium phosphate cement decomposed to β-Tricalcium Phosphate (β-TCP) and Hydroxyapatite (HA) as confirmed by Thermogravimetric Analysis and Differential Thermal Analysis (TGA/DTA) as well as with X-Ray Diffraction (XRD). The obtained mechanical properties are not sufficient for high load bearing implants, where the required strength in ranging between 1.5 -150 MPa and compressive stiffness is above 10 MPa. However further post processing such as infiltration with biodegradable polymers may allow these structures to be used for scaffold applications.

TABLE OF CONTENTS

ACKNOWLEDGEMENTS **3**

ABSTRACT **4**

1 LITERATURE REVIEW **9**

- 1.1 PROPERTIES OF THE BONE 9
  - *1.1.1 Bone structure and composition 9*
  - *1.1.2 Cortical bone 11*
  - *1.1.3 Trabecular bone 14*
  - *1.1.4 Remodeling and bone fracture healing 18*
- 1.2 MATERIALS FOR SCAFFOLD FABRICATION 20
  - *1.2.1 Calcium phosphate cements (CPC) 20*
  - *1.2.2 Calcium Phosphate Ceramics 20*
  - *1.2.3 Biodegradable polymers 22*
  - *1.2.4 Naturally derived biodegradable polymers 23*
  - *1.2.5 Synthetic biodegradable polymers 24*
- 1.3 PRINCIPLE OF TISSUE ENGINEERING 28
- 1.4 CONVENTIONAL TECHNIQUES FOR SCAFFOLD MANUFACTURING 30
  - *1.4.1 Fibre bonding-unwoven meshes 31*
  - *1.4.2 Solvent casting/particulate leaching 31*
  - *1.4.3 Gas foaming 32*
  - *1.4.4 Phase separation/emulsification 32*
- 1.5 RAPID PROTOTYPING TECHNIQUES IN SCAFFOLD MANUFACTURING 33
  - *1.5.1 The basics of RP 34*
  - *1.5.2 Input for RP systems 35*
  - *1.5.3 Microsyringe (Bioplotting) 39*
  - *1.5.4 Selective Laser Sintering (SLS) 40*
  - *1.5.5 Stereolitography (SLA) 40*
  - *1.5.6 Fused Deposition Modeling (FDM) 41*
  - *1.5.7 3D printing (3DP) 42*
- 1.6 MOTIVATION FOR WORK 43

2 MATERIALS AND METHODS **45**

- 2.1 MECHANICAL TESTING AND FEA ANALYSIS OF 3D PRINTED BONE SCAFFOLDS 45
  - *2.1.1 The designed geometry 47*
  - *2.1.2 Finite Element Analysis 47*
  - *2.1.3 Mechanical Testing 49*
- 2.2 DIMENSIONAL ACCURACY OF 3D PRINTED BONE SCAFFOLD GEOMETRIES 50

2.2.1 The designed geometry *50*
2.2.2 Investigated process parameters *51*
2.2.3 Measuring Accuracy *54*
2.3 3D PRINTING OF CALCIUM PHOSPHATE CEMENTS (CPC) 55
2.3.1 Materials *55*
2.3.2 3D Printing of CPC samples *56*
2.3.3 Post processing *56*
2.3.4 Mechanical characterization *57*
2.3.5 Thermal analysis *57*
2.3.6 XRD analysis *57*
2.4 EFFECTS OF SATURATION AND POST PROCESSING ON POROSITY AND MECHANICAL PROPERTIES OF PRINTED CALCIUM PHOSPHATE SCAFFOLDS 59

3 RESULTS.. 60

3.1 MECHANICAL TESTING AND FEA ANALYSIS OF 3D PRINTED BONE SCAFFOLDS 60
3.1.1 FEA results *60*
3.1.2 Mechanical testing results *61*
3.2 DIMENSIONAL ACCURACY OF 3D PRINTED BONE SCAFFOLD GEOMETRIES 63
3.2.1 Particle size *63*
3.2.2 Analysis of variance *64*
3.2.3 Factors and their interaction *65*
3.3 3D PRINTING OF CALCIUM PHOSPHATE CEMENTS (CPC) 70
3.3.1 SEM *70*
3.3.2 Mechanical testing *71*
3.3.3 Thermal analysis *71*
3.3.4 XRD analysis of CaP phase evolution *73*
3.4 EFFECTS OF SATURATION AND POST PROCESSING ON POROSITY AND MECHANICAL PROPERTIES OF PRINTED CALCIUM PHOSPHATE SCAFFOLDS 74
3.5 3D PRINTER MODIFICATIONS 58

4 DISCUSSION.. 77

5 CONCLUSIONS AND FURTHER DIRECTIONS.. 82

REFERENCES.. 84

APPENDICES.. 93

APPENDIX A 93
APPENDIX B 94

LIST OF FIGURES

Figure 1.1 Structure of compact and cancellous bone [11]. 11

Figure 1.2 Scanning electron microscope photograph of (a) normal and (b) osteoporotic cancellous bone [19]. 15

Figure 1.3 Stress strain curve of trabecular bone 16

Figure 1.4 Structure of PLGA, were x is the number of units of lactic acid and y is the number of units of glycolic acids. 27

Figure 1.5 Scaffold use for cell proliferation to produce a functional implant. 29

Figure 1.6 Building the part layer-by-layer. 35

Figure 1.7 A sample STL file [77]. 36

Figure 1.8 the factors that are having influence on the accuracy of the stl file (where D-chord error, γ-largest centre angle) [77]. 36

Figure 1.9 The surface profiles of prototype. 38

Figure 1.10 The highest divergence between the cad model and the actual prototype 39

Figure 1.11 Cell printer and the image of a printed cell structure [79] 39

Figure 1.12 Schematic of the operating principles principle of SLS [80]. 40

Figure 1.13 SLA builds up the parts by solidifying photocurable resin with UV laser light [80] 41

Figure 1.14 Schematic of the operating principles of the FDM process [84]. 42

Figure 1.15 The 3D Printing sequence. 43

Figure 2.1 General process of scaffold manufacturing by 3DP 45

Figure 2.2 Cubic, cylindrical, and reinforced unit cells used for generating porous scaffolds. 47

Figure 2.3 Increase of compressive modulus as a result of the increase in the number of unit cells perpendicular to loading. 48

Figure 2.3 Different packing of cubic unit cells into the cubic frame showing loading direction on their (a) flat surfaces, (b) their edges, and (c) their vertices. 48

Figure 2.4 Schematic of the fabricated test frame geometry. 51

Figure 2.5 (a) Picture of build chamber and co-ordinate system used and (b) indication of the locations of the specimens within the build chamber. 53

Figure 2.6 Schematic of the orientation of the printed test frames in location three, six and nine 54

Figure 2.7 The process of measuring accuracy 54

Figure 2.8 Photographs of 3D Printed specimens after removal from the powder bed (a) solid block for mechanical testing and (b) test scaffold 56

Figure 3.1 FEA determined normalized compressive modulus of all structures with relative density of 20% in three different directions with unit cells are loaded on their flat, edge and vertex surfaces. 61

Figure 3.2 3DP scaffolds built from cubic, cylindrical and reinforced cubic unit cells, where the unit cells were loaded in three different directions (flat surface, edge plane, and vertex plane) 62

Figure 3.3 Mechanical testing results of the infiltrated (a) and uninfiltrated (b) loading the unit cell patterns in the three directions and for the cubic, cylindrical and reinforced structures. *Note: The values are only connected for better* 63

Figure 3.4 Particle size distributions for (a) zp102 and (b) zp130 powders with the x-axis in micrometers and the secondary y axis shown in percentage. 64

Figure 3.5 Contribution of the factors in the model for (a) zp102 and (b) zp130. 65

Figure 3.6 Size and saturation factor influence on accuracy for (a) zp102 and (b) zp130 66

Figure 3.7 Percentage beam accuracy in relation to beam size and orientation at a saturation of 100% for (a) zp102 and (b) zp130. 67

Figure 3.8 Actual measured beam sizes in the z direction at 100% saturation in position five 67

Figure 3.9 Percentage beam accuracy in relation to beam size and orientation at a saturation of 75% for (a) zp102 and at a saturation of 125% for (b) zp130 68

Figure 3.10 Accuracy map of the build chamber for zp102 in (a) x, (b) y, and (c) z orientations. 68

Figure 3.11 Accuracy map of the build chamber for zp130 in x (a), y (b), and z (c) orientations. 69

Figure 3.12 SEM images of scaffold before (a) and after (b) sintering 71

Figure 3.13 (a) DTA and (b) TGA curve for the 3D printed CPC scaffolds and post-processed (sintered) β-TCP scaffold. 72

Figure 3.14 DTA (a) and TGA (b) curve for 3D printed CPC scaffolds at different heating rate. 73

Figure 3.15 XRD patterns for raw materials and scaffold samples. 74

Figure 3.16 SEM images before (a) and after (b) sintering 76

Figure 3.17 Schematic image of the modifications 58

1 Literature review

Recent trends in tissue engineering (TE) are demonstrating an increasing interest to apply rapid prototyping techniques in artificial tissue production. Although there are many techniques and approaches that have been published for various TE applications this thesis is intended to focus on the biodegradable bone scaffold production with the application of the 3D Printer.

Finite element method is the most commonly used engineering tool to optimize complex geometries hence is preferred for developing complex scaffold geometries as well. However the production of the previously designed and analysed model with a parameter sensitive rapid prototyping machine, like the 3D printer, is not straight forward. Questions like dimensional accuracy and its dependence on the parameter settings and the printer's general behaviour with new materials will be investigated here in detail. Since suitable mechanical properties are also crucial for the final application, the scaffold strength and stiffness behaviour and the possibilities to improve these with post processing will also be investigated. This work is also intended to extend the applications of the calcium phosphate based biodegradable powders in conjunction with the 3D printer.

1.1 Properties of the bone

Bone is an intricate, living, constantly changing tissue with complex hierarchical structure and remarkable mechanical behaviour. Understanding its properties is essential for creating artificial bone tissue engineering products. As a part of the skeleton bone fulfils complex functions. In the body: provide supporting framework, protects vital organs like the brain and bone marrow and facilitate movement as they are connected with muscles.

1.1.1 Bone structure and composition

Bones serve as a reservoir for calcium ions and are involved in calcium metabolism and cell formation [1, 2]. Bones and teeth contain almost 99% of total body calcium and 85% of total body phosphorous [3]. The term bone includes a family of materials built up of mineralized collagen fibrils [4] . It consists mainly of two phases, an inorganic phase mostly built up of calcium phosphates (50-60 wt %) and an organic matrix primarily composed of type I collagen (30-40 wt %), in addition, it contains water up to 10 wt% [3]. Bone is also a living tissue, its organic matrix contains about 15 wt% of cells including osteocytes (bone cells), osteoclasts (bone resorbing cells), osteoblasts (bone building cells) and bone lining cells [5].

The organic matrix of bone mainly consists of type I collagen, however a series of non-collagenous proteins and lipids are also present. Type I collagen is a large fibrous protein with a repetitive amino-acid sequence, allowing three polypeptide chains to fold into a triple helix structure [6]. Collagen may not have significant influence on the strength and stiffness of bone, given the respective elastic modulus of collagen (1.5 GPa) compared to hydroxyapatite (114 GPa) [7]. However, it is crucial to toughness and post-yield behaviour of bone. Furthermore, collagen prevents crack progression, inhibiting their growth to critical dimensions [8].

The inorganic component of bone consists of poorly crystallized, calcium deficient hydroxyapatite ($Ca_{10}(PO_4)_6(OH)$) with ionic substitution, such as, magnesium, sodium, potassium, fluorine, chlorine, and carbonate ions. Impurities in biological apatite make bone more reactive and less stable by introducing significant stresses to its crystal structure. Especially the presence of 4-8% carbonate substitution and 0.5-1.5% magnesium substitution has special importance leading to increased strain and solubility [3]. Crystals of biological hydroxyapatite are very small and soluble compared to pure artificial HA or even to calcium deficient HA. Plate like apatite crystals occur within the discrete spaces within the collagen fibrils, which forces the plates to be discontinuous and of discrete size of around 50 x 25 nm [9].

At the macrostructure level, as illustrated in Figure 1.1, bone can be distinguished into cortical, (also called compact) and cancellous (also called trabecular) bone. In long bones, such as the femur or tibia, a dense cortical outer layer surrounds the inner cancellous bone that has a reinforcing function. In case of flat bones, like the calvaria, a sandwich structure can be observed with dense outer layers and lightweight cancellous interior [9]. The architecture and composition of cancellous and cortical bone allow the skeleton to perform its essential mechanical functions. The stiffer cortical bone responds more slowly to changes in loads while cancellous bone has a much larger surface area per unit volume and a greater rate of metabolic activity [10].

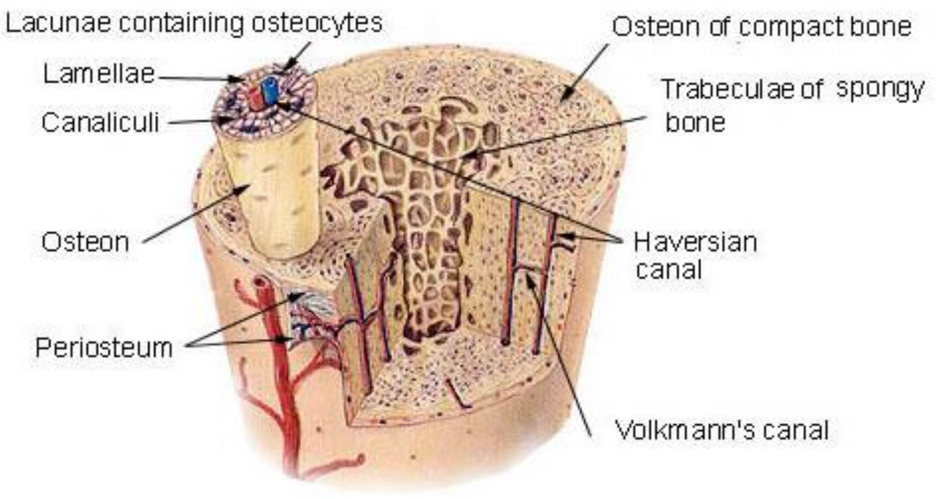

Figure 1.1 Structure of compact and cancellous bone [11].

1.1.2 Cortical bone

The hierarchical structure of compact bone is shown Figure 1.1. The structural unit of compact bone is called the osteon. Each osteon is an elongated cylinder oriented parallel to the long axis of bone, and is about 200-250 μm in diameter. Cortical bone is made up of closely packed osteons that consists of a central canal called the Haversian canal, which is surrounded by concentric rings (lamellae) of bone matrix. Each of the matrix tubes is a lamella therefore compact bone is often called lamellar bone. Collagen fibres in one lamella are aligned in a single direction, while in the neighbouring lamella fibres run in the opposite direction. This reinforcing pattern can withstand great torsion stresses and protects the central canal that contains blood vessels and nerve fibres serving the needs of the osteons. Ascenzi et al. examined mechanical properties of 50μm osteon segments [12]. In tension these had an average elastic modulus of 5.5-12 GPa and strength of 102-120 MPa, and in compression a modulus of 6-7 GPa and a compression strength of 110-130 MPa respectively. Bending stiffness was around 2-3GPa while bending strength was approximately 350-390 MPa. The torsional modulus and strength were 16-20 GPa and 160-200 MPa, respectively.

A second type of canal can also be found in cortical bone, these connect the Haversian canals, lie perpendicular to the long axis of bone, and are called Volkmann’s canals. Between the rings of matrix, the osteocytes are located in small cavities, called lacunae. Small channels (canaliculi) radiate from the lacunae to the Haversian canal to provide passageways through the hard matrix, see Figure 1.1. The osteonic canals contain blood vessels that are parallel to the long axis of the bone. These blood vessels interconnect with vessels on the surface of the bone [13].

Cortical bone is a large portion of skeletal bone; it has high density and low surface area [3]. The density of this type of bone lies in range of 1800-2000 kg/m^3. The mechanical properties of cortical bone are greatly influenced by mineralization level, porosity and organization of the solid matrix. These vary with skeletal region and local positioning [14]. The mechanical properties of compact bone have been measured in many studies, and were reviewed by Reilly and Burstein [15]. Elastic properties and strength of cortical bone reported by various authors are summarized Table 1.1 and Figure 1.2 respectively. The studies indicated below did not test bones as a whole but rather tested specimens cut from the cortex of bone. These had a cross sectional area in range of 4-20 mm^2, containing multiple osteons or lamellae. The treatment of cortical bone specimens during storage and testing has been shown to have a significant effect on the reported mechanical properties. Fresh, dried or embalmed bone exhibited significantly different mechanical behaviour. Bone in-vivo is not dry, and although its exact state of hydration is not fully known, its conditions may be closer to wet then dry testing conditions. Dried bone has an increased elastic moduli, and decreased strength and strain to failure. Completely dry bone does not yield at all. In many studies rewetted dry bone was used, but it must be noted that drying can induce cracks, that changes the stress-strain response [15].

Type of loading	**Elastic constants [GPa]**	**Comments**
Compression, low strain	E=8.69 $E_{radial}=3.76$ $E_{transverse}=4.19$	Small cubes of rewetted dry femur, tibia, humerus
Compression, low strain	E=14.1	Cylinders of rewetted dry femur, tibia, humerus
Tension, low strain	E=14.1	Dry, rewetted femur, tibia, humerus
Compression, low strain	E=10.4	Femur
Tension, low strain	E=17.3	Femur
Torsion, low strain	G=0.31	
Bending	E=15.5	Femur, mid-portion
Tension	E=6	Femur, mid-portion
Tension	E=14.1	Femur

Table 1.1 Elastic properties of cortical bone, where E is the elastic modulus and G is the torsional modulus. (Loading was parallel to the long axis of bone unless stated otherwise) [15].

The above data is hard to compare as procedures for storage and testing are not standardized. In many cases the exact strain rate is not reported, although strain rate can significantly influence the obtained elastic constants. Data reported in Table 1.2 summarizes the measured strength values using tension, compression, torsion and bending. In case of tension and compression, the ultimate strength values are reported. Parallel to the long axis of bone, that is in the longitudinal direction, both in tension and compression, bone is linearly elastic up to ~0.7 % of strain, beyond this point it is yields plastically up to strains of about 3%. In the transverse direction, compact bone is less stiff, less ductile and less strong, and in case of tensional loading, it fails at around 0.6 % of strain [16].

Type and direction of loading	Strength [MPa]	Comments
Tensile, low strain, longitudinal	$\sigma_u=78.8$	Femur, tibia, humerus, dry, rewetted
Compressive, longitudinal	$\sigma_u=131$	Femur, tibia, humerus, dry, rewetted
Compressive, transverse	$\sigma_u=106$	Femur, tibia, humerus, dry, rewetted
Compressive, radial	$\sigma_u=117$	Femur, tibia, humerus, dry, rewetted
Tensile, low strain, longitudinal	$\sigma_u=122\pm1.1$	Femur
	$\sigma_u=140\pm1.2$	Tibia
	$\sigma_u=146\pm1.5$	Fibula
Tensile, longitudinal	$\sigma_u=95.3\pm27$	Tibia, dry rewetted
Tensile, transverse	$\sigma_u=9.9\pm2.9$	Tibia, dry rewetted
Tensile, longitudinal	$\sigma_u=138$	Tibia, less than 60 years old
Tensile, low strain, longitudinal	$\sigma_u=118$	Tibia, more than 60 years old
Tensile, low strain	$\sigma_u=151\pm18$	Femur
Compressive, low strain, longitudinal	$\sigma_u=159\pm4.1$	Femur
Torsion, low train	$\sigma_{shear}=53.1$	Femur
Single shear	$\sigma_{shear}=82.4$	Femur
Bending	$\sigma_{bending}=157$	Femur
Bending, low strain	$\sigma_{bending}=164\pm29$	Femur
Bending, low strain	$\sigma_{bending}=181$	Femur

Table 1.2 Strength of cortical bone, where σ_u is the tensional ultimate strength, σ_{shear} is the shear strength, and $\sigma_{bending}$ is the bending strength [15]

1.1.3 Trabecular bone

In contrast to compact bone, that has a dense and solid appearance; trabecular or cancellous bone has an open, meshwork or foam-like structure as shown in Figure 1.2. Trabecular rods are about 50-300 μm in diameter. It has a high surface area, but forms only a smaller portion of the skeletal mass [3]. Cancellous bone is made up of a repeat of rods and struts called trabeculae, and looks like a poorly organized, arbitrary or random structure. In fact, the trabeculae align precisely along lines of stress and help bone resists stress [13]. It has long been established that bone grows in response to stress [17], as comparisons between the depositions of trabeculae and direction of principle stresses, suggest that trabeculae develop along principle stress trajectories of the loaded bone [18]. Trabeculaes are only a few cell layers thick, and contain irregularly arranged lamellae and osteocytes interconnected by caneliculi. There are no osteons present in cancellous bone [13]. In general, trabecular bone is significantly more active metabolically, and therefore is remodelled more often, consequently, is younger than cortical bone. The mechanical properties of bone may differ due to differences in their age [9].

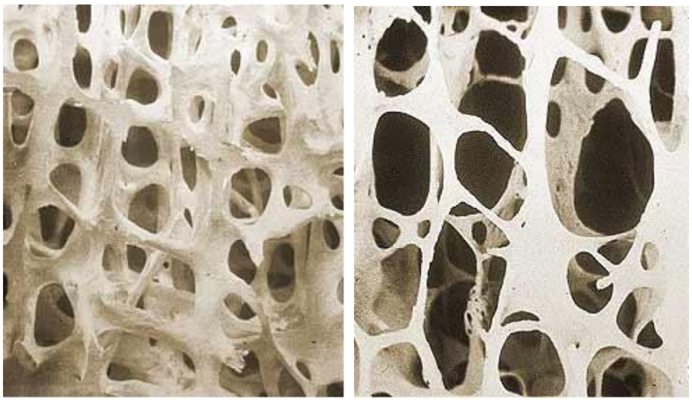

(a) (b)

Figure 1.2 Scanning electron microscope photograph of
(a) normal and (b) osteoporotic cancellous bone [19].

Properties of cancellous bone vary widely according to the anatomical location of the specimen. This reflects the strong dependence of these properties on the volume fraction and architecture of the bone. The relative density of cancellous bone is typically between 0.05 and 0.7. The average density of individual trabeculae taken from cancellous bone is 1820 kg/m^3 [16]. The mechanical properties of individual trabeculae have been assumed to be the same as those of compact bone, however direct testing in tension or bending is difficult as these specimens are curved along their length and their cross sectional area also varies. Table 1.3 shows that reported values for the elastic modulus of individual trabeculae vary from 0.8 to 20 GPa.

Type of loading	Elastic modulus [GPa]	Comments
Tensile testing	E = 0.76	Specimens from femur
Three point bending	E = 3.17	tibia
Three point bending	E = 5.35±1.35	Proximal tibia, wet
Tensile	E = 10.4±3.5	Dry
Ultrasound test method	E = 14.8±1.4	Wet
Nanoindentation	E = 19.6±3.5 E = 15±3.0	Dry, longitudinal Dry, transverse

Table 1.3 Elastic properties of individual trabeculae [9, 16].

Studies on the mechanical behaviour of cancellous bone material, demonstrated that it acts as a porous engineering material due to its open pore structure and energy absorption capabilities. The stress-strain curve of cancellous bone can be characterized by three distinct regions (Figure 1.3). First, a linear elastic region can be observed that results from the elastic bending or extension of the trabeculae. At around 0.1 % of strain the trabeculae start to deform non-linearly. Beyond this curve, there is an extended plastic region where constant stress is maintained due to collapse within the cellular framework. As the pores continue to collapse, the stiffness may again increase [16]. Studies in literature demonstrated huge variations in strength and modulus that has been shown to be a function of anatomic location, loading direction, and method of storage and testing [20].

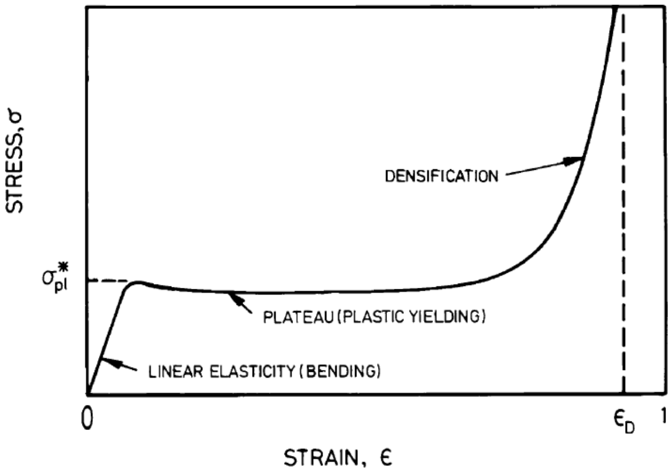

Figure 1.3 Stress strain curve of trabecular bone

Table 1.4 gives an overview of the mechanical properties of human cancellous bone at different anatomical locations.

Properties (Strength/Modulus)	**Comments**	**Type of bone**
E=1.4-79 MPa σ=1.5-45MPa	Fresh frozen, uniaxial strain	Proximal tibia
E=8-457 σ=1-13	Fresh frozen, uniaxial stress	Proximal tibia
E=5-552 σ=0.52-11	Fresh frozen, uniaxial stress	Proximal tibia
E=413-1516	Fresh frozen, uniaxial stress	Distal femur
E=58.8-2942 σ=0.98-22.5	Fresh frozen, uniaxial stress, variable strain rate	Distal femur
E=7.6-800 σ=0.56-18.6	Fresh frozen, uniaxial stress	Distal femur
E=20.68-965 σ=0.15-13.5	Fresh, uniaxial stress	Proximal femur
E=344.7 (average) σ=120-310 MPa	Fresh frozen, tested at 37 ºC	Proximal femur
E=10-428 σ =0.06-15	Fresh frozen, uniaxial stress	Vertebral bodies
E=158-378 G=58-89	Fresh, ultrasound	Vertebral bodies
E=15-30	Fresh frozen, uniaxial stress	Vertebral bodies
E=121-580	Fresh, orthogonal moduli	Patella
E=1.1-448 σ =0.03-6.3	Fresh frozen, uniaxial stress	Humerus, distal radius
E=5-282 σ=0.12-82	Fresh frozen, uniaxial stress	Iliac crest

Table 1.4 Mechanical properties of human trabecular bone as a function of anatomic location, where E is the elastic modulus and σ is the ultimate strength [20].

Elastic modulus in tibia is within the range 1-550 MPa, in the distal femur it varies between 7 and 2900 MPa; and for the patella, humerus and iliac crest it varies greatly, but remains below 500 MPa [20]. Strength in the proximal tibia is reported to be between 1.5 and 45 MPa, and for the femur between 0.15 and 310MPa. It was found to be the lowest in the humerus where strength of cancellous bone was between 0.03 and 6 MPa.

1.1.4 Remodelling and bone fracture healing

Bone is a dynamic and active tissue that continuously goes through small scale architectural changes. Unlike other mineralized tissues, bone continuously undergoes remodelling, as it is resorbed by osteoclasts that are bone-destroying cells and formed by osteoblasts (bone lining cells). Physiologic remodelling does not change bone shape and consists of bone resorption followed by bone deposition in approximately the same location. Adaptive remodelling is the response of the bone to altered loads and may alter the strength, density and shape of bone [10]. Since it continues throughout life, it appears to be important for maintenance of the skeleton. The purpose of remodelling is the release of calcium and the repair of micro-damaged bone from everyday stress. The iteration of remodelling processes shapes and sculptures bone during growth and afterwards [3].

Osteoblasts contain an alkaline phosphate that is a weak base. It increases the local pH that results in precipitation of biological apatite, into which osteocytes have migrated, become trapped and surrounded by bone matrix. Osteoclasts mature and migrate to specific bone surfaces, activate enzymes – such as acid phosphates – and are secreted against the mineral substrate that causes dissolution. This process is called resorption that allows stored calcium to be released into systemic circulation, and is an important process in regulating calcium balance. The iteration of remodelling processes shapes and sculptures bone during growth and afterwards [21].

It has been shown that CaP ceramics can integrate into the remodelling process as osteoclasts are able to resorb and phagocytose CaP bone substitutes similarly to the in-vivo mechanism of natural bone degradation [21]. Substitution of CaP scaffolds by normal bone is essential for the regeneration of bone defects and depends on many cellular events especially upon a resorption rate. Osteoclasts are able to resorb CaP ceramics furthermore osteoclasts play a role in phagocytosis. CaP ceramic surfaces are resorbed by an acidic microenvironment and the resorbed CaP crystals are subsequently phagocytosed and degraded by the osteoclasts [21].

This continuously ongoing remodelling process is regulated by two control loops. One is a negative feedback hormonal mechanism maintaining calcium homeostasis in the blood, while the other involves responses to gravitational and mechanical forces acting on bone as described by Wolff’s law [13]. Bone is a tissue that is fully capable of regeneration. From tissue engineering point of view it is of outstanding importance to understand the mechanism of this regeneration, as this remodelling and regeneration mechanism is going to help the integration of the scaffold.

The healing time for simple fractures is six to eight weeks, however it can be longer for large weight-bearing bones, and for fractures at an older age. Despite their remarkable mechanical properties, bones can fracture or break. When bone breaks, blood vessels in bone and in the surrounding tissue are torn. As a result a mass of clotted blood forms at the fracture site [13]. This is the first step of the healing process as this newly formed fibrin clot becomes the host of inflammatory cells, fibroblasts and invading capillaries [22].

The next stage of the process is the repair stage (4 to 40 days) when the early granulation tissue (soft callus) unites the fractured bone ends, thus providing a foundation for repair. The increase of vascularity and cellularity play key roles in the healing process. In the meantime, fibroblasts and osteoblasts migrate into the fracture site and begin reconstructing the bone. Fibroblasts excrete collagen fibres that connect the broken bone ends. Some fibroblasts differentiate into chondroblasts, which secrete collagen matrix. Meanwhile osteoblasts begin forming cancellous bone. This tissue, that now splints the broken bone is called fibro cartilaginous callus [13, 22]. Then, as a result of osteoblastic activity, new bone trabeculae begin to appear in the fibrocartilaginous callus and gradually convert it to a hard callus of the cancellous bone. This hard callus formation begins three to four weeks after injury and continues for two-three month. Remodelling is also present from the beginning of hard callus formation. As remodelling is part of normal bone turnover, and the remodelled region responds to the same set of mechanical stresses, the healed bone resembles that of the original [22].

1.2 Materials for scaffold fabrication

1.2.1 Calcium phosphate cements (CPC)

In the mid 1980’s Brown and Chow introduced low temperature Calcium Phosphate Cements (CPC) that opened up new possibilities for the use of CaPs for the treatments of bone defects [23]. CPCs are a mixture of CaP powders and water, where the CaP(s) dissolves and precipitates into a less soluble CaP. As a result of the precipitation reaction, CaP crystals grow and become entangled, so the cement gains some mechanical rigidity.

The most investigated end-product of the precipitation is PHA – a precipitated hydroxyapatite. PHA is poorly crystalline, is of submicron dimensions and it resembles the apatite of natural bone except for the absence of impurities (Na-, Mg-, carbonate) in its structure. It has the molar Ca/P ratio between 1.5 and 1.67. If the molar Ca/P ratio is below 1.67 it is called Calcium Deficient Hydroxypatite (CDHA). It is also known for its large specific surface area (25-100 m^2/g), which also makes it a promising candidate as a tissue engineering scaffold material. However, in general CPCs are fragile materials [24]. Depending on composition there is great variance in mechanical properties. The main determining factor is the ratio between the amount of cement powder and mixing liquid (P/L). A high P/L ratio results in low porosity and increased mechanical properties as mechanical properties increase exponentially with decrease in porosity. Most CPCs have an initial compressive strength of 10-100 MPa that is 5-20 times higher than their tensile strength, however their mechanical properties increase continually with implantation time [25]. Therefore, these cements are favoured for non-load bearing applications or in combination with metal implants. CPCs are used for maxillofacial surgery, distal radius and hip fractures, and reinforcements of cancellous bone screws. Depending on the Ca/P composition at temperatures above 700 ºC CPCs can be transformed to calcium phosphate ceramics such as β -TCP or HA [24].

1.2.2 Calcium Phosphate Ceramics

Calcium Phosphate (CaP) ceramics are attractive as bone substitutes for numerous reasons. Most importantly marrow cells are known to attach and proliferate on these materials and there is a successful clinical history behind the use of these materials in orthopaedic sites [26]. They are also favourable synthetic materials for tissue engineering applications due to their biocompatibility, similarity to the mineral phase of natural bone and bioactivity that promotes direct bone growth onto their surfaces resulting in direct bonding to hard tissues. For this reason, metal prostheses are coated with hydroxyapatite to ensure direct biological fixation of the prosthesis into the bone [24]. Hydroxyapatite ($Ca_{10}(PO_4)_6(OH)_2$, HA) and β - Tricalcium Phosphate ($Ca_3(PO_4)_2$, β-TCP) are the most commonly used and most widely investigated of high-temperature calcium orthophosphates for bone defect repair in clinical practice. HA and β-TCP can only be obtained by thermal treatment above 600-700 °C, where they crystallise and become less soluble than the mineral component of bone. β - TCP has a calcium-phosphate (Ca/P) ratio of 1.5, while HA has a Ca/P ratio of 1.67 and the dissolution rate of β-TCP is 3-12 times faster than that of HA. All traditional CaPs used in bone reconstruction are high temperature CaPs [24].

Only certain CaP compounds are useful for implantation in the body as both their solubility and speed of hydrolysis increase with decreasing Ca/P ratio. Drissens indicated that CaP ceramics with a Ca/P ratio less than one are not suitable for biological implantation [27]. Resorption or biodegradation of CaP ceramics is caused by physiochemical dissolution depending on the solubility of the materials and on the local pH. Physical disintegration into smaller particles is a result of chemical attacks of the grain boundaries, and biological factors, such as phagocytosis, which decreases local pH concentrations.

Tricalcium-phosphates has two polymorphs, α and β-TCPs that are commonly used as bioceramics. X-ray diffraction indicates that β polymorphs transforms to α polymorph at temperatures between 1120 and 1290ºC. β-TCP is degradable, degradation occurs by osteoclastic activity. α and β-TCP have the same chemical compositions, but a different crystallographic structure, and for that reason the α polymorph is much more soluble. In general, the degradation rate of CaPs increases as the surface area or crystal imperfection increases. Degradation also increases if the crystallinity or crystal grain size decreases. Furthermore, if there are ionic substitutions like CO_2^{-3}, Mg^{2+} or Sr^{2+} in HA it degradation rate is also increased. [28]

1.2.3 Biodegradable polymers

The development of synthetic biodegradable polymers has in recent years enabled the design and development of temporary three-dimensional templates or scaffolds for tissue engineering products to support, reinforce and in some cases guide the regeneration of healing tissues [29]. These biodegradable polymers are suitable for those tissue engineering applications where the goal is tissue repair or remodelling. These scaffolds require a temporary structure with interconnected porosity and favourable chemical properties [30]. As the polymer will degrade over time in the body during which the tissue is growing, the need for a second surgery to remove the implant is eliminated [31]. In terms of biocompatibility, biodegradable materials must fulfil more requirements than highly stable materials, as not only the implant itself has to be biocompatible but potential toxicity of degradation products and metabolites should also be considered, in terms of both local tissue response and systemic response.

After implantation, when polymeric surfaces are in contact with body fluids, they immediately absorb proteinaceous components, and the bulk material begins to absorb soluble components, like water, ions, lipids and proteins. Cellular elements attach to the surface and initiate chemical processes [28]. It has been indicated that biodegradable polymers go through hydrolysis as an essential component of the degradation process [32]. Hydrolysis is the scission of molecular functional groups by reaction with water that may be catalysed by acids, bases, salts, or enzymes. Functional groups of hydrolysable polymers consist of carbonyls bonded to heterochain elements (O, N, S). Esters, amides, urethans, carbonates and anhydrates are examples of hydrolysable polymers with potential applications in tissue engineering. Hydrolytically susceptible groups exhibit different degradation rates, which are dependent on intrinsic properties of the functional group and on molecular and morphological characteristics. Anhydrites display the fastest hydrolysis rate, followed by esters and carbonates. If contained in a hydrophobic backbone or in a highly crystalline morphologic structure some carboxyl groups, such as urethanes, imides or amides may demonstrate long term stability in vivo. Factors that can further increase the rate of hydrolysis of biodegradable polymers are listed below [28]:

- High number of hydrolysable groups in the main or side chains
- Other polar groups that enhance hydrophobicity

- Low crystallinity
- Low cross link density
- High surface to volume ratio
- Mechanical stress

Human body implants may be designed to function at isothermal temperature (37 ºC), neutral pH level (pH 7.4) and in an aseptic aqueous steady state. However, complex interactions of body fluid components like activators, receptors, and inhibitors produce aggressive response to foreign bodies. Extracellular body fluids contain proteins, lipids, organic acids and ions such as H^+, OH^-, Na^+, Cl^-, HCO_3^-, PO_4^{-3}, K^+, Mg^{2+}, Ca^{2+}, and SO_4^{2-} and it has been shown that certain ions catalyze hydrolysis and increase reaction rates by several order of magnitudes [33].

Depending on the hydrophylicity of the polymers these ions may have a surface or a combined surface-bulk effect. Hydrophobic polymers absorb only a negligible concentration of ions while hydrogels absorb large amounts of water resulting in high ion concentrations and therefore bulk hydrolysis. Besides, the effects of ionic concentrations, pH changes in the vicinity of the implanted device during inflammation or infection can also act as a catalyser of hydrolysis. Enzymes are also catalysts that can alter reaction rate; however their effect varies on different functional groups. They have strong catalytic effect on ester groups while urethane and ether groups that are otherwise hydrolytically susceptible do not show significant hydrolysis [34]. Due to the large molecular size of enzymes, their predominant effect is on the surface of the material. However as degrading surface becomes fragmented, or if the material is porous with high surface to volume ratio (like in the case of tissue engineering scaffolds), enzymatic effects may be enhanced [28].

1.2.4 Naturally derived biodegradable polymers

Naturally derived protein or carbohydrate polymers have been used as scaffolds for the growth of several tissue types. By far the most popular natural polymer used for tissue engineering scaffolds is collagen as it is the main component of human connective tissues including bone. Collagen is a basic constituent of natural bone, it has been used many studies for fabricating bone tissue engineering scaffolds [35, 36]. However, there are other biologically derived biodegradable polymers that may be of interest in these applications.

Starch

Starch is a polysaccharide that can be produced from plants like potato, corn and rice. The starch molecule has two important functional group, the –OH and the C-O-C groups. The former group is susceptible to substitution reactions and the latter to chain breakage [37]. This material is thereby biodegradable. The melting temperature of starch, in the order or 450 ºC, is significantly higher than that of other polymers [38]. In biomedical applications starch is mostly used as a filler or reinforcing material with other biodegradable polymers [39].

Polyhydroxyalkanoates (PHA)

Polyhydroxyalkanoates (PHA) is degradable, biocompatible and thermoplastic polyester that is made by several micro-organisms [40, 41]. They are intracellular storage polymers with a function to provide a reserve of carbon and energy to micro-organisms, that is similar to the role of starch in plant metabolism [42]. PHB (poly(3-hydroxybutyrate)) is the simplest and the most extensively studied PHA. The manufacture of PHB is based on the fermentation of sugars by the bacterium caligenes eutrophous. These polymers are highly crystalline, relatively hydrophobic and extremely brittle, resulting in in-vivo degradation rates in the order of a few years [40]. Copolymers of PHB with hydroxyvaleric acid have similar degradation rate, but are more flexible, processable and are less crystalline. PHB and hydroxyvaleric acid copolymers are already available and are applied in field of controlled drug release and are attractive for orthopaedic applications.

1.2.5 Synthetic biodegradable polymers

The advantage of synthetic over natural biodegradable polymers is that they can be easily mass-produced, and their properties the degradation rate or mechanical behaviour, can be tailored to suit specific applications [30]. A large number of polymeric compositions and structures have been suggested as biodegradable polymers, however up to date, detailed toxicological studies in-vivo are only available for a fraction of possible biodegradable polymers. A large percentage (80%) of currently approved synthetic polymers for clinical use are polyesters including poly(lactic acid), poly(glycolic acid), and poly(caprolactone) [28]. This review is limited to the most commonly investigated biodegradable polymers.

Polyanhydrates

Polyanhydrates are extensively studied biodegradable materials. Due to rapid degradation and limited mechanical properties, the main application for this class of polymers is in short-term controlled delivery of bioactive agents [43]. Polyanhydrites degrade by surface erosion that allows the delivery of drugs at a known rate, its degradation products are non-toxic [28]. Their limited mechanical properties – tensile modulus 1-50 MPa [44, 45] and tensile strength of less than 5 MPa [44] - restrict their use in load bearing orthopaedic applications. To improve mechanical properties, photo crosslinkable polyanhydrates have been developed for orthopaedic applications, investigating both UV and visible light curing methods [46]. Depending on the used monomers, mechanical properties varied, but values for compressive strength reached 30-40 MPa and values for tensile strength reached 15-27 MPa [47].

Polyorthoesters

Polyorthoesters are hydrophobic polymers that are mainly used in drug delivery systems because their degradation can be well controlled as they also degrade by surface erosion [48]. Surface erosion is more favourable for load bearing applications as these implants degrade only at their surface, become thinner over time, and keep their mechanical properties and integrity for a longer period of time. Tensile and flexural modulus of polyorthoesters are in range of 800 and 950 MPa, respectively, and its tensile strength is approximately 20 MPa [44], these mechanical properties qualify this material for orthopaedic applications, as these values are in range of the properties of cancellous bone. In vivo studies showed that compared to PLGA, polyorthoesters improve bone growth [49].

Polyurethanes

Polyurethanes are synthetic elastomers used for a variety of long term medical implants [50]. They have good biocompatibility and excellent mechanical properties. Polyurethanes can be designed to have chemical linkages that are degradable in biological environment and are of interest for applications in tissue engineering [51]. Polyurethanes have the structural characteristics of both polyesters and polyamides. Therefore, their susceptibility to biodegradation is similar to polyesters and polyamides, with differences in degradation rates. Degradation rate of polyurethanes is dependent on the pre-polymer. Polyether based polyurethanes are non-degradable, while polyester polyurethanes are biodegradable. The tensile strength of degradable polyurethanes varies between 8-40 MPa [52]. A number of studies investigated the biocompatibility of degradable polyurethanes, and in-vivo and in-vitro studies were statisfactory. Animal studies showed no adverse tissue reactions and rapid tissue ingrowth. However, the effect and removal of degradation products from the body is not clearly understood [52].

Polylactic-acid (PLA)

PLA is a biodegradable, thermoplastic, aliphatic polyester derived from renewable resources. Corn starch and sugarcanes are the commonly used to produce lactic acid by bacterial fermentation. Due to the chiral nature of lactic acid, four morphologically distinct forms of polylactide exist. The most widely used are the stereoregular forms (D-PLA and L-PLA) that are semi-crystalline, while the optically inactive D,L-PLA is amorphous [53]. L-PLA melts around 173-178 ºC and has a glass transition temperature between 60-65 ºC [52]. Its tensile and flexural modulus are approximately 1.2 and 1.4 GPa, respectively, while its tensile strength is around 30 MPa [44]. It has a degradation time of around two years [52]. Due to its amorphous nature, D,L-PLA does not have melting temperature, however its glass transition temperature is around 55-60 ºC [52]. Its tensile modulus and flexural modulus are approximately 1.9 and 2 GPa, respectively, while its tensile strength is also around 30 MPa [44]. D,L-PLA has a degradation time around 12-16 month.

Polyglicolic-Acid (PGA)

PGA is a biodegradable, thermoplastic polymer and the simplest linear, aliphatic polyester. It can be prepared starting from glycolic acid by means of polycondensation or ring-opening polymerization. PGA has been known since 1954 as a tough fibre forming polymer, however, owing to its hydrolytic instability its use has initially been limited. PGA has a glass transition temperature between 35-40 ºC and its melting point is reported to be in the range of 225-230 ºC. PGA also exhibits an elevated degree of crystallinity, around 45-55%, thus is insoluble in water [54]. Its tensile modulus is approximately 7 GPa and it has an approximate degradation time of 6-12 month [52].

Polylactic-co-glycolic acid *(PLGA)*

PLGA is synthesized by means of random ring-opening co-polymerization of two different monomers of glycolic acid and lactic acid, see Figure 1.4.

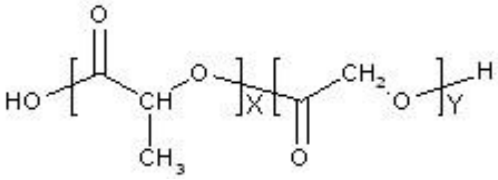

Figure 1.4 Structure of PLGA, were x is the number of units of lactic acid and y is the number of units of glycolic acids.

Depending on the ratio of lactide to glycolide used for the polymerization, different forms of PLGA can be obtained: these are usually identified with respect to the used monomers ratios (e.g. PLGA 75:25 identifies a copolymer whose composition is 75% lactic acid and 25% glycolic acid). All PLGAs are amorphous rather than crystalline and show a glass transition temperature around 45-60 °C [52]. It is generally accepted in literature that intermediate copolymers are more unstable with respect to hydrolysis than the homopolymers. Elastic modulus of these copolymers is approximately 2 GPa.

The degradation mechanism of PGA, PLA and their copolymers is random hydrolysis of their ester bonds. The lactic acid and glycolic acid then enter the tricarboxylic cycle and are excreted as water and CO_2. However, the rate of degradation is determined by the configurational structure, copolymer ratio, crystallinity, molecular weight, morphology, stresses, porosity and site of implantation. PLA, PGA and their copolymers are considered to be biocompatible, non-toxic and non inflammatory [55, 56] and are among the few biodegradable polymers approved by the FDA for clinical applications. However, concerns have been raised, when PLA and PGA implants with considerable size produced toxic solutions, indicating that critical size implants may result in release of degradation products with high local acid concentrations.

Polycaprolactone (PCL)

PCL is a simple, linear, aliphatic polyester with degradation rate in the order of one year. PCL is a semi-crystalline polymer with remarkably low glass transition temperature (- 60 ºC). Its melting temperature is also relatively low, 60 ºC. An interesting characteristic of PCL is its remarkable thermal stability, while other aliphatic polyesters have a decomposition temperature around 250 ºC, the decomposition temperature of PCL is over 350 ºC. In the semi-crystalline state the high-molecular-weight polymer is tough and flexible [57, 58]. PCL is highly permeable for many therapeutic drugs and is highly tissue and osteoblast compatible [59]. Since it is highly hydrophobic, it has lower biodegradation in vivo than poly(lactic acid). Its degradation time is in the order of two years, for this reason it is favoured as a drug delivery device that remain active for over one year [28]. For other applications, copolymers have been synthesized to accelerate the rate of bio-absorption. Copolymers of PCL with dl-lactide have yielded materials with more-rapid degradation rates. PCL has modest mechanical properties; its tensile and flexural modulus is in the order of 400 and 500 MPa, respectively and its strength is around 20 MPa [44]. It has been used in different biomedical applications, such as scaffolds for tissue engineering of bone and cartilage and is favoured material of drug delivery devices [31, 53, 60, 61].

PCL can be easily processed by conventional procedures, due to its relatively low melting point and high thermal stability. Therefore, PCL may be easily filled with stiffer materials (particles or fibres) and processed by melting techniques. The major drawback of PCL is poor cell adhesion and proliferation on their surfaces due its high hydrophobicity that limits its biomedical applications [39]. However, the addition of osteoconductive ceramics as fillers can overcome this problem and make the surface more attractive for cell attachment. An interdisciplinary group in Singapore has studied and patented the production of PCL and several PCL based composites (PCL/HA, PCL/TCP etc.) using FDM [61]. These bone tissue-engineering scaffolds confer favourable mechanical and biochemical properties, including strength via the ceramic phase, toughness and plasticity via the polymer phase, favourable degradation and resorption kinetics and graded mechanical stiffness. Shor et al. has also tested these PCL/HA composite scaffolds for bone engineering and reported encouraging results [60].

1.3 Principle of tissue engineering

After serious trauma or disease when the bone suffers large segmental defects, it will not be able to regenerate itself without external intervention. Damaged or lost tissue or organ therapies include transplantation, surgical reconstruction, drug therapy, synthetic prostheses. The shortage of donors and cell morbidity limits transplantation, synthetic prostheses cannot replace all functions of the damages/lost tissue and may produce chronic rejection, drug therapies may have crucial side-effects [62, 63].

The need of artificial bone replacements, due the limited donor availability is an emerging problem in orthopaedic surgery. The aim of bone tissue engineering is to overcome these problems by providing high quality heterogenous transplants that can be supplied in larger quantities {Hutmacher, 2000 #6}. Furthermore currently used orthopaedic implants fail to meet critical characteristics of natural living tissues, they lack the ability of self repair, maintenance of blood supply, and are unable to modify their structural and properties as a function of environmental factors like mechanical loading [64]. These associated problems have elicited the development of new alternatives. And in recent years, there has been a change in thinking, focus from tissue replacement shifted to regeneration of tissues to their original state and function.

The revolutionary idea of Tissue Engineering (TE) is to produce artificial biological substitutes by using suitable cells in combination with various materials and state-of-the-art engineering solutions. A main approach in TE is to use the patient's own cells to build up an implant that can augment or replace a tissue function or a complete organ. The fundamental problem is that the cells can proliferate into larger colonies; however they are incapable of forming three-dimensional tissues/organs in vitro [65]. To form a three-dimensional organized tissue the cells need complex mechanical, chemical, and electrical signals which are present in their natural environment [66]. For this reason it is necessary to use a porous matrix called a scaffold to which the cells can attach, proliferate and differentiate (initiate bone formation) in vitro and afterwards this can be inserted to the anatomical defect, see Figure 1.5. This matrix is only necessary until the cells form the desired anatomical shape and gain sufficient mechanical properties to withstand the physiological loading, therefore scaffolds are ideally made from bioresorbable materials [67].

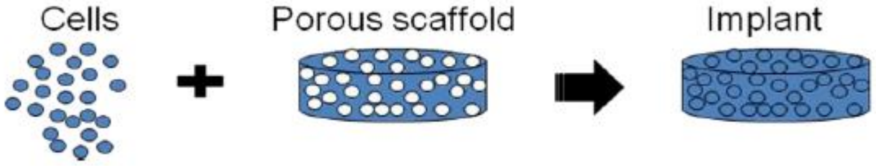

Figure 1.5 Scaffold use for cell proliferation to produce a functional implant.

Due to its complex role the scaffold needs to fulfil requirements in many aspects. Appropriate micro and macro geometry including high porosity (50-80%) is required to enhance mass transport of nutrients and metabolic waste to and from the cells [68]. Moreover the pore structure has to be interconnected to promote tissue integration and vascularisation [69]. The macro geometry of the scaffold has to fit into the complex three-dimensional anatomic defect. To satisfy this condition medical imaging technologies like Computed Tomography (CT), μCT or Magnetic Resonance Imaging (MRI) can be used for mapping the defect site [70]. Scaffolds should also possess sufficient mechanical properties that provide structural support for the cells until the native tissue builds up . The scaffold is ideally made of bioresorbable material, with appropriate degradation profile that will dissolve in the body without toxic by-products, thus providing space for new tissue formation. Furthermore appropriate surface chemistry is of high importance in ensuring cell attachment, differentiation and proliferation [71].

Tissue engineered scaffolds should aid the growth of relevant cells into their 3D tissue. For this, and since cells randomly migrate to 2D layers, the application of a 3D porous scaffold that replaces the extracellular matrix of the tissue and into which the cells can be seeded is required [65]. With this structure in place, cells can then adhere to the scaffold, proliferate and initiate bone formation.

1.4 Conventional techniques for scaffold manufacturing

Several techniques have been developed to process synthetic and natural scaffold materials into porous structures. These so-called conventional scaffold fabrication techniques are defined herein as processes that create scaffolds having a continuous, uninterrupted pore structure [65]. Traditional methodologies of scaffold fabrication include fibre bonding, solvent casting and particulate leaching, membrane lamination, melt moulding and gas foaming. However, the quality of the scaffolds that are manufactured with these techniques are often compromised. The drawbacks of these techniques include the extensive use of highly toxic organic solvents, long fabrication periods, labour-intensive processes, incomplete removal of residual particulates in the polymer matrix, poor repeatability, irregularly shaped pores, insufficient interconnectivity of pores and thin structures. In addition, most of these methods bear restrictions on shape control. For example, casting is dependent on the shape of the mould and it is not possible to independently and easily control the porosity and pore size of the scaffolds [73]. Table 1.5 gives an overview over the conventional scaffold manufacturing techniques.

Method	Porosity	Advantages	Disadvantages	Pore size (µm)
Fibre bonding Unwoven mesh	81%	Highly porous scaffolds with interconnected pores	Solvents are poisonous to cells	500
Solvent casting / Particulate leaching	87%	Structure has strength or electrical conductivity	Organic solvents used that contaminates the polymer	100
Gas foaming	93%	Biocompatible	Organic solvents used that contaminates the polymer	100
Phase separation / emulsification	95%	Pore size and porosity easily changed	Solvents are poisonous to cells	13-35

Table 1.5 Scaffold properties produced by various conventional techniques.

1.4.1 Fibre bonding-unwoven meshes

Early scaffolds (1993) were produced from PGA fibres by Mikos et al. using the fibre bonding technique [74]. To produce a scaffold, the PGA fibres were first immersed in a PLLA solution, after evaporation of the solvent, the network of PGA fibres is embedded in a PLLA matrix. The composite was then heated above the melting temperature of PGA. The PLLA has a lower melting temperature, so it melted first and filled the spaces left by the fibres. This helped to maintain the architecture of fibres so that when the PGA began to melt, the fibre structure was conserved and fibres at the meeting-points were melted together. The PLLA was then dissolved with methylene-chloride (PGA is insoluble in it). The porosity of these foams was as high as 81% and pore diameters were approximately 500 µm. Scaffolds with the above described spatial arrangement are suitable for cell implantation and promote cell interaction [75, 76]. Although positive results have been reported on fibre bonding techniques, it must be emphasized that this method involves the use of toxic solvents that must be extracted. To completely remove these solvents, the scaffolds must be vacuum dried for several days which inhibits the immediate clinical application of the manufactured scaffold.

1.4.2 Solvent casting/particulate leaching

This method uses water-soluble porogens, such as sieved particles of salt (NaCl) to create highly porous scaffolds. First the polymer (PLLA or PLGA) is dissolved in chloroform or methylene-chloride and then cast into a petri-dish filled with the porogen. Then the solvent is evaporated and the composite is leached in deionised water at 25 °C for 48 h to remove the NaCl. Porosity can be controlled by the amount of salt added, and pore size by the size of the salt crystals. Scaffolds with more than 70 w% salt exhibited high interconnectivity. Foams fabricated in this manner have been used extensively with various cell types and have shown no adverse effects on new tissue formation, but this technique also involves the use of toxic solvents.

A modification of this method intends to avoid morphological differences between the parts on the surface and inside the petri-dish. It involves compression moulding of the composite into cylindrical form at temperatures just above the melting (PLLA) or glass transition temperature (PLGA). Cylinders are then cut into discs of desired thickness before leaching in water. This allows more precise control of scaffold thickness and increases uniformity of the foam surface. However, thermal degradation of the polymer during the compression moulding step could be a concern [76].

1.4.3 Gas foaming

Gas foaming, also known as gas saturation, eliminates the need for organic solvents during pore-making, and uses gas as a porogen. First solid discs of PGA, PLLA or PLGA are formed using compression moulding. The discs are exposed to high pressure CO_2 (5.5 MPa) for 72 hours at room temperature, than the pressure is rapidly decreased to atmospheric level. This creates thermodynamic instability for the CO_2 dissolved in the polymer disks, and results in the nucleation and growth of gas cells within the polymer matrix. The method resulted in scaffolds with porosities of up to 93% and pore sizes of up to 100 μm. The advantage of this method is that toxic chemicals are not used. The high temperatures during compression moulding, however still prohibit the incorporation of cells or bioactive molecules during processing. Furthermore, the pores are unconnected, especially on the surface of the compression moulded disks [76].

1.4.4 Phase separation/emulsification

Two methods are known, emulsification/freeze-drying and liquid-liquid phase separation. With emulsification/freeze-drying, PLGA is dissolved in methylene-chloride and then distilled water is added to form an emulsion. The mixture is then cast in a mould and quenched in liquid nitrogen. After that, the scaffolds are freeze-dried at -55 °C, to remove the dispersed water and polymer solvents. Scaffolds are reported to own large porosities (up to 95%), but small pore sizes (13-35 μm). A persisting challenge of this method is to increase pore size, in order to make the scaffold suitable for cell implantation.

Liquid-liquid phase separation takes advantage of thermodynamic principles to create polymer-rich and polymer-poor phases within a polymer solution, the polymer poor phase is then removed. The polymers are dissolved in naphthalene, phenol or 1,4-dioxane. These solvents have a low melting point and are easy to sublime. Water can be added to induce phase separation. The polymer solution is cooled below the melting point of the solvent and then vacuum dried for several days to promote complete solvent sublimation. Cooling parameters have critical importance in determining scaffold morphology. Foams up to 90% porous, with pores of approximately 100 μm, have been reported using this technique [76].

1.5 Rapid Prototyping techniques in scaffold manufacturing

By using rapid prototyping (RP) techniques in scaffold manufacturing both the external and internal geometry can be designed in advance using computer aided design (CAD), and mechanical properties can be analysed and optimised by Finite Element Analysis (FEA). Various RP techniques have been investigated in scaffold manufacturing [7-9]. In general, the dimensional accuracy, mechanical properties, and applicable materials are restricted by the particular technology. These systems, such as 3 dimensional printing (3DP) and selective laser sintering (SLS), can produce porous scaffolds for tissue engineering. In these systems, particles are selectively bonded in a thin layer of powder material by adhesive droplets and by laser radiation respectively. The thin 2D layers are bonded on top of each other to form the 3D solid structure. The built object in both cases is supported by the unprocessed powder, thereby allowing the fabrication of overhanging features such as porous structures with designed internal architecture. A key advantage of both technologies is that a large variety of materials can be used as long as they are available in the form of powder. Dimensional accuracy is limited in these processes by the nozzle size / laser diameter, control over the printhead / laser movement and positioning, and the particle size of the powder. Limitations of both technologies include: the ability to fabricate of features of the required scale, the difficulty of removal of the unbounded powder from the porous internal architecture, and poor mechanical properties that may require post processing.

Preceding the development of rapid prototyping methods numerous conventional techniques including solvent casting particulate leaching, fibre bonding, membrane lamination, and gas foaming were invented to fabricate porous structures. For example, in solvent casting/particulate leaching, pores are formed by evaporative solvent and pore-forming agent particles that are mixed and cast into a mould and leached out afterwards. This method just like other conventional techniques is incapable of precisely controlling pore size, geometry and spatial distribution. With these techniques, the internal architecture cannot be accurately designed in advance. Moreover there may be no guarantee of the required pore interconnectivity [65]. Using conventional techniques the size of the scaffold can be limited due to difficulties in removal of the porogens. Another important disadvantage is that some these techniques are applying organic solvents during the process that may remain in the scaffold afterwards. These are unfavourable in medical applications due to their carcinogenicity and toxicity. These techniques are also labour intensive, not repeatable and often do not control well the micro and macro geometry of the scaffold. Most of the above listed problems could be overcome by using RP techniques [73].

Probably the most significant advantage of RP techniques over the so called conventional scaffold manufacturing techniques is that they can produce more intricate, previously designed and analyzed geometries. Taking advantage of the possibilities of RP we can have strict control on the porous architecture size, shape and interconnectivity. 3D printing (3DP) is one prospective RP technique that may be used in manufacturing hard tissues. 3D printing (3DP), Selective laser sintering (SLS) and Fused deposition modelling (FDM) are the most promising techniques that can be used in hard tissue manufacturing.

1.5.1 The basics of RP

Rapid prototyping is a group of manufacturing technologies that create three-dimensional objects layer-by-layer, directly from CAD data sources. These methods bind materials selectively, and involve several advantages compared to the classical subtractive fabrication techniques. When designing for rapid prototyping objects can have complex internal and external geometries, while the time to market is reduced quick machine setup and since complex assemblies can be replaced by one single part.

RP allows the application of various materials and reduces the costs as no tools or moulds are required. Most of the RP systems add and bond materials in layers to form three-dimensional objects. Therefore such systems are also known by the names additive fabrication, three dimensional printing, Solid Freeform Fabrication (SFF) and layered manufacturing, see Figure 1.6.

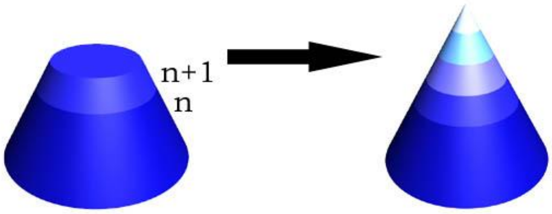

Figure 1.6 Building the part layer-by-layer.

1.5.2 Input for RP systems

After a three-dimensional model is created in CAD it is used to produce segments with a predefined layer thickness. In order to reduce the computing time of the segment creations an “stl” file is created. The layers are built up on each other, thus a three dimensional model is created. By using this method, hollow objects, intricate geometries and overhanging parts can be created

The stl files can be created from a 3D CAD file, using three-dimensional scanner, CT or MRI. The stl file contains a list of data on each triangle that describe the surface of the model. The list of data is made up from coordinates of vertices of each triangle, and a unit vector that shows an outward direction (normal vector), as shown in Figure 1.7**.** The method by which the triangles make up the surface is an important issue. More triangles does not necessarily result in better accuracy since, for instance, in the case of flat surfaces more triangles would result only in larger computing time for the slicing algorithm, but it would make no difference to accuracy [77].

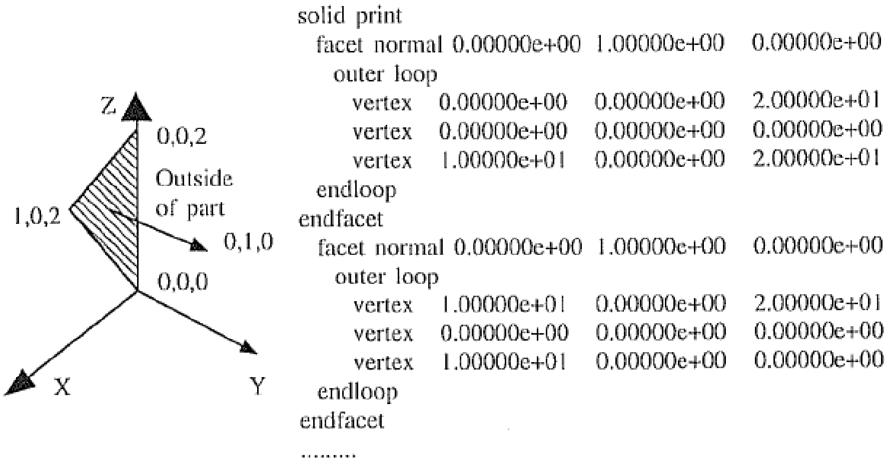

```
solid print
  facet normal 0.00000e+00 1.00000e+00  0.00000e+00
    outer loop
      vertex   0.00000e+00  0.00000e+00  2.00000e+01
      vertex   0.00000e+00  0.00000e+00  0.00000e+00
      vertex   1.00000e+01  0.00000e+00  2.00000e+01
  endloop
endfacet
  facet normal 0.00000e+00 1.00000e+00  0.00000e+00
    outer loop
      vertex   1.00000e+01  0.00000e+00  2.00000e+01
      vertex   0.00000e+00  0.00000e+00  0.00000e+00
      vertex   1.00000e+01  0.00000e+00  0.00000e+00
  endloop
endfacet
.........
```

Figure 1.7 A sample STL file [77].

*Factors that influencing the *.stl file accuracy*

When an stl file is generated, the accuracy of the model depends on two main factors. The chord error is the biggest distance between the real chord and the generated triangles (D). The second is the largest centre angle that can be drawn for the edge that approaches the contour curve (γ), see Figure 1.8.

.

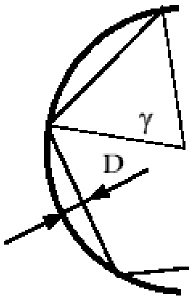

Figure 1.8 the factors that are having influence on the accuracy of the stl file
(where D-chord error, γ-largest centre angle) [77].

The accuracy of the stl file and the amount of triangles required depend mainly on the surface of the part that has to be represented. For instance representation of a cylinder's surface can be approached with a straight line and a curve perpendicular to it, while in case of a sphere two perpendicular curves are required. The difference in accuracy can be multiple when the same number of triangles was applied. The accurate stl file generation requires several other conditions. The triangles must form a closed volume and all edges must be bounded with two triangles. To check this condition, the Euler-rule can be applied.

$$-\frac{F}{2}+V=2\ (B-P) \qquad (1.1)$$

where: F – The number of sides, that is in this case the number of triangles

V – Number of vertices

B – The number of separate solids

P – The number of through passing bores

Compliance with the Euler equation is a necessary requirement however it is not satisfactory. To ensure that the stl file is suitable for accurate scaffold manufacturing mesh integrity should be checked with appropriate programs.

Surface quality on RP produced parts

For a better result surface roughness should not differ from the original model, although every RP technology has its limitation, as shown in Table 1.6.

Technology	Material	Error (mm)			Ra (µm)	
		Mean	**σ**	**P**	**Z**	**x-y**
SLA	Epoxy	-0,08	0,3	0,02	3,7	1,7
SGC	PES	0,15	0,35	0,01	9,8	5,0
LOM	Paper	0,35	0,47	0,11	4,0	2,4
FDM	P300	-0,24	0,43	0,00	11,0	1,2
	P200	-0,03	0,32	0,00	11,2	5,0
SLS	PC	0,15	0,42	0,15	16,6	15,3
	PA55	-0,05	0,7	0,51	18,4	14,8

Table 1.6 The surface coarseness for each RP technology
(Ω is the standard deviation and P is the probability) [78].

Resolution error

This mistake originates from the resolution limit of the equipment, since all RP technology deals with limited number of addressable coordinates either in x,y,z direction.

Accuracy error

All errors that are arising from the defects of the stl file as well as from the inaccuracy and arrangement dependent factors.

Error that depends on the layer thickness

This error occurs when the side of the model is not perpendicular to the base, thus the side of the prototype will be rough, see Figure 1.9.

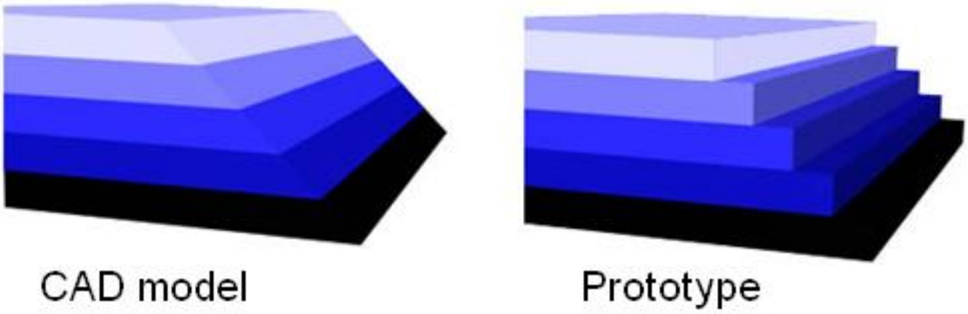

Figure 1.9 The surface profiles of prototype.

The coarseness of the surface can be described by the difference compared to the prescribed surface. If we indicate the layer thickness with t then the highest divergence (R_{max}) can be calculated with the following equation (Figure 1.10):

$$R_{\max} = \frac{t}{2\sqrt{2}} \tag{1.2}$$

The average divergence ($R_{average}$):

$$R_{average} = \frac{t}{4\sqrt{2}} \tag{1.3}$$

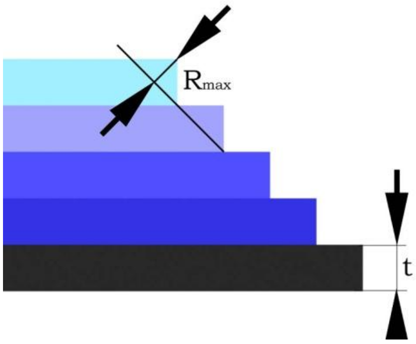

Figure 1.10 The highest divergence between the cad model and the actual prototype

If the angle between the side and the base of the model indicated with ω then R_{max} and $R_{average}$ can be calculated as the following:

$$R_{\max} = \frac{t}{2}\cos\omega \qquad R_{átl} = \frac{t}{4}\cos\omega \qquad (1.4)$$

1.5.3 Microsyringe (Bioplotting)

Microsyringe is a recently developed technique that is mainly used in the manufacture of porous scaffolds. During the process a microsyringe expels a dissolved polymer under low and constant pressure to form the desired pattern. The resolution of this method is on a cellular scale, which is remarkably high compared to the techniques described in the following chapters. However, capillaries with a very small diameter require careful handling to avoid any tip breakage. Higher pressure is also needed to expel the material from a small orifice [65].

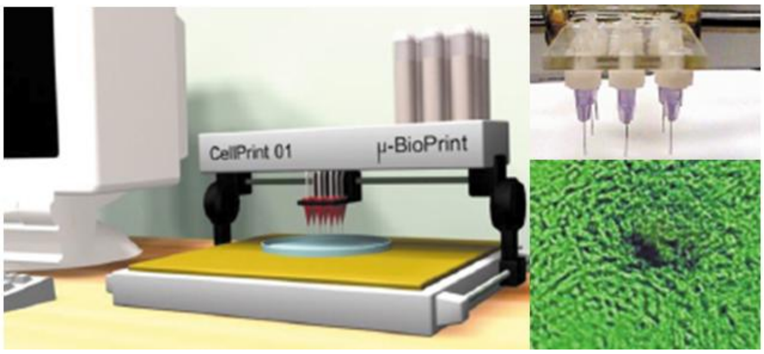

Figure 1.11 Cell printer and the image of a printed cell structure [79]

1.5.4 Selective Laser Sintering (SLS)

SLS uses a deflected laser beam selectively to scan over the powder surface following the cross-sectional profiles carried by the slice data. It constructs scaffolds by sequentially fusing regions in a powder bed, layer by layer, via the computer controlled scanning laser beam. The interaction of the laser beam with the powder elevates the powder temperature to reach the glass-transition temperature, causing surfaces in contact to deform and fuse together Figure 1.12.

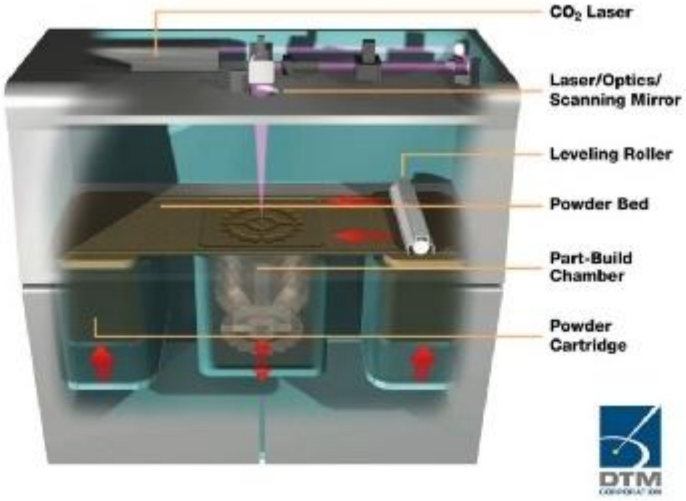

Figure 1.12 Schematic of the operating principles principle of SLS [80].

1.5.5 Stereolitography (SLA)

SLA involves selective polymerization of a liquid photo-curable resin by an ultraviolet laser beam. The UV beam is guided (x- and y-axis control) onto the liquid resin surface in accordance to the CAD cross-sectional data, and it solidifies the model’s cross-section while leaving the remaining areas in liquid form. After the first layer is built, the elevator holding the model is lowered along the z axis to allow the liquid photopolymer to cover the surface. A ‘wiper arm’ is then displaced over the liquid to flatten the surface. The procedure is repeated until the model is completed. This system requires support structures to be added to the model, to prevent any overhanging or unconnected features from falling to the bottom of the liquid-filled vat [65].

A UV laser traces out the first layer of photocurable resin, solidifying the model’s cross-section while leaving the remaining areas in liquid form. The elevator then drops by a sufficient amount to cover the solid polymer with another layer of liquid resin. A sweeper recoats the solidified layer with liquid resin and the laser traces the second layer atop the first. Chu et al. have produced HA-based porous implants using SLA-built epoxy moulds [81]. A thermal curable HA–acrylate suspension was cast into the mould to obtain a scaffold with interconnected channels. The resolution of channel width achieved was as low as 366 mm. In another study, investigators carried out an in vivo study using two different architecture designs, orthogonal and radial channels. The preliminary results showed that controlling the overall geometry of the regenerated bone tissue was possible through the internal architectural design of the scaffolds [82].

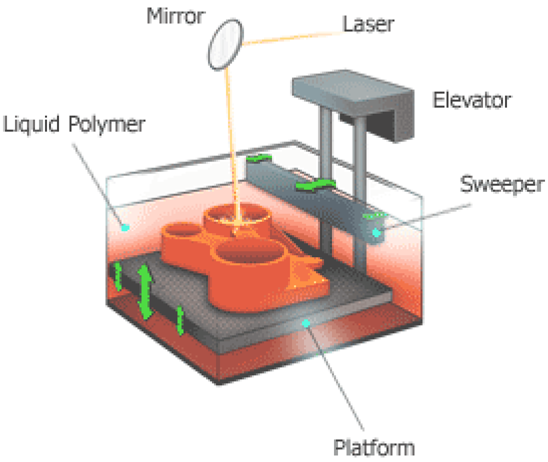

Figure 1.13 SLA builds up the parts by solidifying photocurable resin with UV laser light [80]

1.5.6 Fused Deposition Modelling (FDM)

FDM is a melt-dissolution deposition technique where a suitable material is fed into a heated liquefier where it is melted and then deposited through a moving nozzle. The nozzle is controlled in the x and y axis while the model is lowered along the z axis. The procedure is repeated layer by layer until the part is fully completed (Figure 1.14). The model is created in a temperature controlled environment that ensures sufficient fusion between the subsequent layers. Although overhanging or unconnected features can be manufactured, external structures have to be deposited to support such features [82, 83]

Drawbacks of the FDM technique include the need for input material of a specific diametric size and material properties to allow feed through the rollers and nozzle. Any changes in the properties of the material require effort to recalibrate the settings of the feeding parameters. As a result, FDM has a narrow processing window. The resolution of FDM is relatively low, at 250 mm. In FDM, a limited range of materials can be used, with almost complete exclusion of natural polymers, as the material used must be made into filaments and melted into a semi-liquid phase before extrusion.

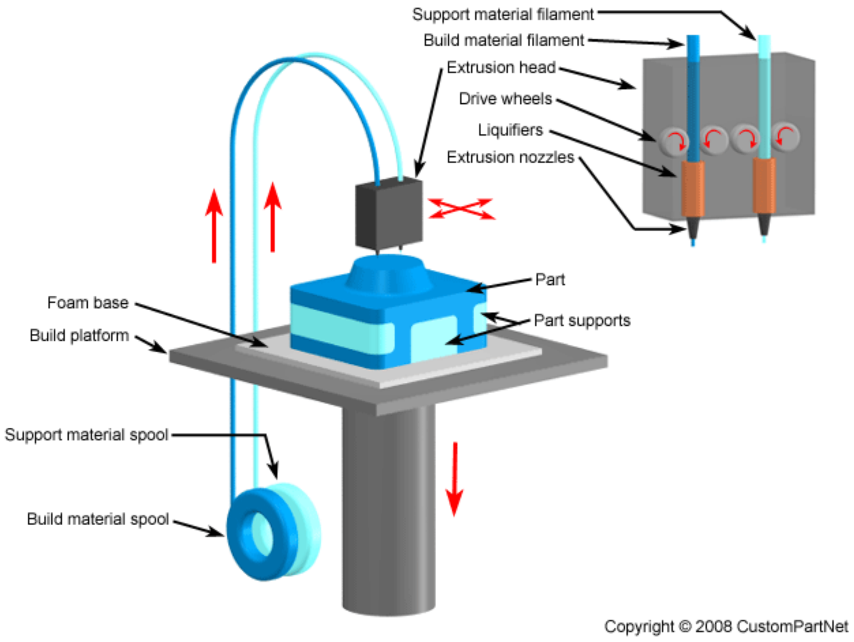

Figure 1.14 Schematic of the operating principles of the FDM process [84].

The operating temperature of the system is too high to incorporate biomolecules into the scaffold, hence limiting the biomimetic aspects of the scaffold produced. Moreover, the material deposited solidifies into dense filaments, blocking the formation of microporosity. Microporosity is an important factor in encouraging neovascularization and cell attachment [82].

1.5.7 3D printing (3DP)

3D printing was developed at MIT in 1989. The 3D printer joins the particles together with a liquid binder that is selectively deposited to the powder through a conventional ink-jet printer head. The ejection of the liquid binder follows the sliced two-dimensional profile of a computer model. The subsequent stacking and printing of powder layers on previously printed layers generates the complete the 3dimensional structure of the desired object. The function of the binder is to join adjacent powder particles of the same and of neighbouring layers [85]. Currently 3DP is successfully used in various applications including rapid tooling and appearance modelling. However in these cases requirements are often not complex and there are several specific barriers that need to be overcome for hard tissue engineering.

The printing process builds up the parts layer by layer (Figure 1.15). In the first step the feed piston is raised while the build piston is lowered. A roller moves the powder from the feed chamber to the build chamber and lays it down as an even layer. In the next step the printerhead deposits the binder according to the actual cross section that was obtained from the CAD model. This sequence is repeated until the part is fully ready. After removal from the powder bed the part needs to be “depowdered” where the loose particles are removed from the surface and from the internal cavities.

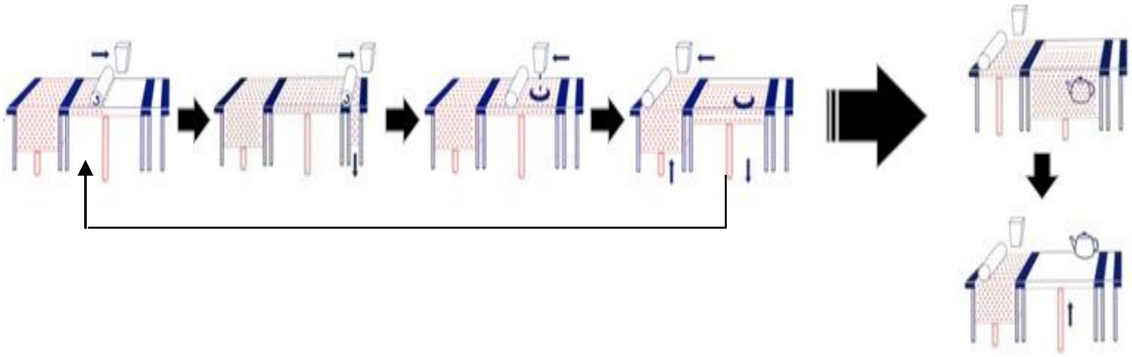

Figure 1.15 The 3D Printing sequence.

The built object is supported by the unprocessed powder therefore it is possible to fabricate overhanging features allowing for porous structures with designed internal architecture. A key advantage of both technologies is that a large variety of materials can be used given that they are available in the form of powder. Dimensional accuracy is limited by the nozzle size, control over the printer head and positioning, and the particle size of the powder. Limitations include the ability to fabricate features of the required scale, the removal of the unbound powder from the porous internal architecture, and poor mechanical properties that may require post processing.

1.6 Motivation for work

The principle of achieving a three dimensional scaffold directly, with 3DP, overcomes the problems of solvent or burnt debris left from a pyrolysis type process of mould cavity scaffold production techniques. Rapid prototyping techniques also in general have the ability to create much more complex internal geometries than conventional techniques.

3DP has been one of the most investigated RP techniques for tissue engineering applications [31, 70, 71, 73, 86-90]. Lam et al. demonstrated that natural biopolymers like starch with water as a binder can be used with 3DP [73]. In general the fabricated parts are having poor mechanical properties for bone scaffold applications, therefore post processing such as sintering or infiltration is required. Lee et al. described an indirect 3DP protocol, where moulds were printed and the final materials were cast into the mould cavity [87]. This was done in an effort to overcome the limited materials available for 3DP. In some more recent work, Gbureck et al. applied calcium phosphate based materials with 3DP to build drug delivery devices and implants by solidifying the materials with water based binders [91-93].

Despite the useful previous work already completed on the implementation of 3DP for bone scaffold fabrication there are many areas requiring more investigation. In this work, more detailed examination of the dimensional accuracy is presented for scaffold geometries. Factors that were investigated include feature size, saturation, orientation, and part location during fabrication in 3DP system. Dicalcium Phosphate Anhydrous (DCPA) and Calcium Hydroxide ($Ca(OH)_2$) with binder of sodium phosphate (Na_2HPO_4) were tested for the first time, in this work, for compatibility with the 3DP process. The processing and post processing parameters for this material system were analysed to examine their effect on the mechanical properties and porosity levels in the produced scaffolds using design of experiments methodology. Parameters investigated include saturation level, sintering temperature and sintering holding time. An investigation was also conducted to see if the strength and stiffness of various 3DP scaffold geometries agree with FEA results of the same structures.

2 Materials and Methods

Scaffold manufacturing is a complex process. The flow chart in Figure 2.1 shows inputs required to achieve a set of design goals. The first step is to design the internal geometry and to optimise it to provide the required mechanical properties and macro porosity. A general method for this is using FEA as per other typical engineering applications. In chapter 2.1 a practical example was presented on how to implement the designed geometries and what kind of difficulties are to be expected. Due to the nature of the printing process when manufacturing complex geometries on a small scale the dimensional accuracy is compromised. In order to establish a repeatable and stable process, the dependence of accuracy on process parameters and feature size was investigated in chapter 2.2. Calcium phosphate cements have a successful clinical history in bone replacement although their application in rapid prototyiping machines is not common. Chapter 2.3 presents a work conducted on CPCs to enable their application in the 3D printing machine. Both sintering and infiltration, as they are the two most commonly used post processing methods for traditional applications, were investigated briefly in the following chapters.

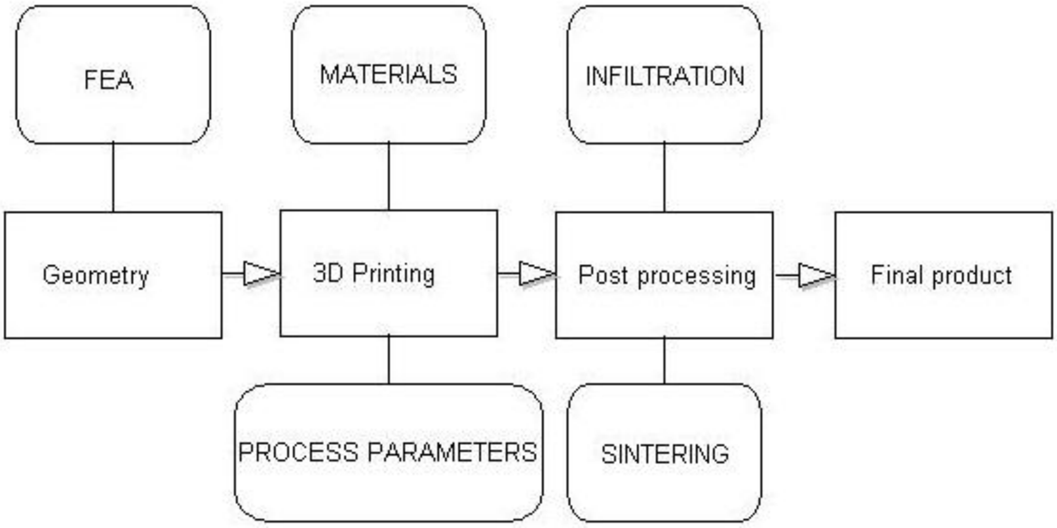

Figure 2.1 General process of scaffold manufacturing by 3DP.

2.1 Mechanical testing and FEA analysis of 3D Printed bone scaffolds

Tissue engineering scaffolds must fulfil the general requirements for mechanically functioning tissues: enhance tissue regeneration, cell nutrition and mass transport and provide mechanical support until the tissue can bear load. These requirements are conflicting since a scaffold which can optimally support tissue regeneration is extremely porous, while a scaffold that can provide sufficient mechanical support has low porosity. However at a given porosity, different microstructures result in different mechanical properties. The pore structure has to be interconnected to promote tissue integration and vascularisation [94].

When scaffolds are implanted to a defect site they have to withstand physiological loading that are generally multi-directional, therefore it is important to map the mechanical properties in different loading directions. At a given porosity level different geometrical patterns have different mechanical properties. By using rapid prototyping techniques in scaffold manufacturing both the external and internal geometry can be designed in advance using computer aided design (CAD) and mechanical properties can be analysed and optimised by FEA. Various RP techniques have been investigated in scaffold manufacturing [71, 73, 89, 95]. In general the dimensional accuracy, mechanical properties, and applicable materials are restricted by the particular technology.

This section presents work performed to test the abilities and limitations of the 3D Printing technology in manufacturing complex, intricate bone scaffold geometries and to determine what structures may provide improved scaffold mechanical properties. This included an examination of the ability of Finite Element Analysis (FEA) to accurately predict the relative stiffness and strengths of the 3D Printed structures.

The structure moduli of three different scaffold geometries (cubic, cylindrical and reinforced cubic) fabricated via 3 dimensional printing were examined. For this purpose compression testing was chosen as this is the most common bone loading type in the physiological environment. Since loading of the scaffold in the physiological environment is multi directional, the directional dependence of these moduli in the different scaffold geometries was also tested. For each of the three geometries, directional dependence of mechanical properties was examined and discussed. The results indicate the usefulness of FEA for designing new structure patterns and the ability to greatly increase scaffold strength. The effect of infiltration as one of the most widely applied post processing method has been also investigated and evaluated.

2.1.1 The designed geometry

Scaffold geometries were built using Solid Works (SolidWorks Inc., Concorde, MA) from 3 different unit cells, see Figure 2.2. These were cubic, cylindrical, and reinforced cubic. The dimensions and porosity of each unit cell were 7x7x7 mm and 80% respectively. In order to maintain the 80% porosity for each design different strut and pore sizes were used. The cross-section of the struts was 4 mm^2 (2 mm x 2 mm) for the cubic, and changed between 1.75 mm^2 (1 .32 mm x 1.32 mm) and 49 (7mm x 7mm) mm^2 for the cylindrical geometries. The cross sectional area of the cubic struts in the reinforced structures was 3 mm^2 (1.75 mm x 1.75 mm) while of the reinforcing beams was 2.26 mm^2 (0.72 mm in diameter).

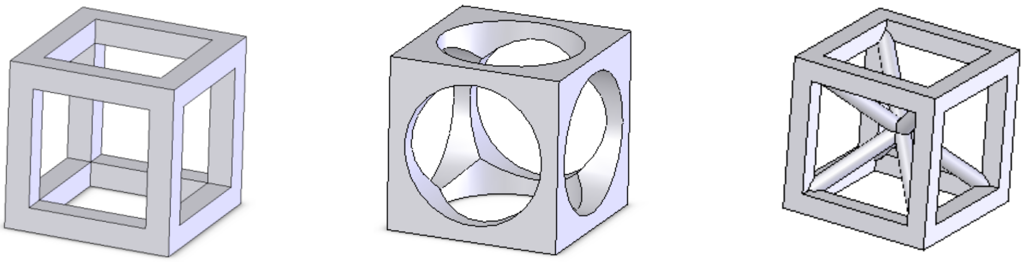

Figure 2.2 Cubic, cylindrical, and reinforced unit cells used for generating porous scaffolds.

2.1.2 Finite Element Analysis

Preliminary FEA simulations were run to find the minimum number of unit cells that would avoid significant bucking of the outer columns during compression. It was found that an increase in the number of unit cells increased the compressive modulus, (Figure 2.3). The target modulus value was determined by applying frictionless supports on the sides, that represents the case of infinite cells (confined case). The minimum number of cells (n=25) was chosen to be in the region, where the curve has almost reached the modulus of the confined case (0.0959). Increasing the number of cells in the vertical direction had no significant effect on the modulus obtained and it was not examined further [96].

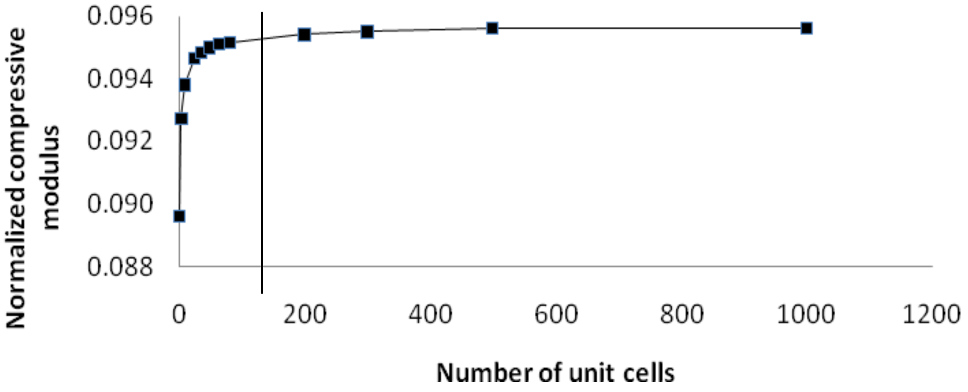

Figure 2.3 Increase of compressive modulus as a result of the increase in the number of unit cells perpendicular to loading.

Based on the preliminary simulations 5x5x5 unit cells were used, so the size of each model/specimen was 35x35x35 mm. The dependence of mechanical properties on loading direction was examined. The unit cell patterns were rotated within the macro envelope to allow loading on their surface, edge and vertex. To represent different loading types a 35x35x35 mm cubic-frame was generated that could accommodate the 125 unit cells. The unit cells were packed in to the cubic-frame so that the unit cells were loaded on their flat surfaces, their edges and their vertices, see Figure 2.4

ANSYS WB 9.0 (ANSYS Inc, Canonsburg, PA) was used to carry out the linear finite element analysis. In the simulations, a fixed support was used on the bottom surface of the cubic frame as the boundary condition. On the top surface, displacement controlled constraint was used to produce 1% of strain.

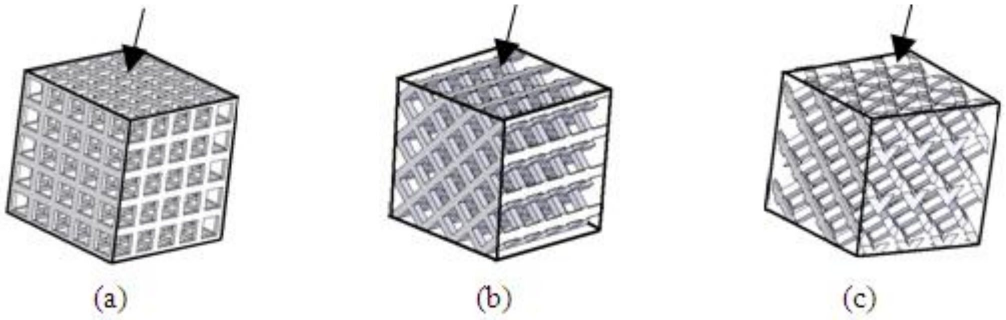

Figure 2.4 Different packing of cubic unit cells into the cubic frame showing loading direction on their (a) flat surfaces, (b) their edges, and (c) their vertices.

The reaction forces were obtained from the simulation and the compressive Young's modulus was calculated according to Hook's law. Before selecting the fineness of the mesh density for the analysis, a convergence study was carried out to ensure that there was a sufficient number of elements in the mesh. The structure was meshed with varying element numbers and subjected to linear perturbation tests with reaction force as the evaluation criteria. Accordingly size controls, and refinement on all edges were used to ensure the necessary number of elements. As a result, the number of elements for the cubic and cylindrical models was just over 125,000 for the cubic and cylindrical modules and 195,000 for the reinforced models[96].

2.1.3 Mechanical Testing

Fully solid control specimens (10x10x10) and the above described porous geometries (35x35x35) were exported to STL file format and built with the Z310 3 Dimensional Printer (Z-Corp, Burlington, MA). Three samples of each scaffold geometry and ten control specimens were fabricated, tested and average compressive and modulus results recorded. A layer thickness of 0.0875 mm was selected for the process. The raw materials used were the proprietary plaster powder, ZP102 and binder ZB56. The analysed structures were manufactured by 3DP, infiltrated with Z-Max epoxy resin and subjected to compression testing. After the build was ready, specimens were left to dry for 24 hours at room temperature before depowdering. The depowdering was conducted by using compressed air with a pressure of 2 bar for initial depowdering and 6 bar for final depowdering. Afterwards specimens were allowed to dry for another 24 hours at room temperature before infiltration with Z-Max epoxy resin (Z-Corp, Burlington, MA). Infiltration of the specimens was carried out using a vacuum chamber. Specimens were kept in the chamber for 60s before immersing them into the polymer resin for 90s while pressure was maintained at a constant 0.2 bar level (absolute pressure). Subsequently specimens were dipped for 60s into the polymer. The infiltrated specimens were then left to dry for 48 hours at room temperature. After mechanical testing it was noted that the infiltrant had fully penetrated all specimens. Uninfiltrated specimens were also prepared and tested. All specimens were measured using callipers with +/- 0.01mm resolution. Each dimension was taken three times and the average value was associated and checked against with the CAD file part dimension. Specimens were subjected to compression testing using an Instron 4204 (Instron Inc., Norwood, MA) vertical universal testing machine with 50 kN load cell with a test speed of 1 mm/min. Compressive modulus and yield strength were calculated for the structures using a 35 by 35 mm area (for the scaffold geometries) and from the linear elastic region of the specimen behaviour.

2.2 Dimensional accuracy of 3D printed bone scaffold geometries

It was shown previously [97] that it is possible to characterize the mechanical properties of the structure by changing the pore structure only and keeping the porosity constant. Furthermore, it was demonstrated that actual geometry solutions provided from FEA cannot fully be examined experimentally due to dimensional differences between the FEA geometry and that which can be produced from the actual RP technique. In this chapter process parameters including powder type, shell saturation, part position, and orientation were examined with the 3D printing technique. This was done in order to assess the potential for this technology to meet the small scale geometric requirements of hard tissue bone scaffold structures. The results may be compared in later studies with the biodegradable materials.

Useful scaffold geometries should have high porosity (60-80%) with small (100-500 μm) interconnected pores. Therefore dimensional accuracy on the micron level is one of the crucial parameters of the bone scaffolds. Previously it was shown that the behaviour of scaffold geometries can be approximately simulated using the Finite Element Modeling (FEM) however the prediction of actual strength and stiffness values are dependent on dimensional accuracy [97]. This accuracy is in turn dependent on several parameters including particle size and shape, powder-binder interaction, and machine setup. In this work different scaffold strut sizes (0.3 - 0.5 mm) have been fabricated using two different plaster powders (zp102 and zp130) with variations in shell saturation levels, part print position, and part print orientation. These are explained in detail in chapter 2.2.2. The parameters for each powder were analyzed using a full 3^5 factorial experimental design. It was found that the part size and orientation had a significant effect on the dimensional accuracy while the influence of the shell saturation and position was relatively small. The results allow for better dimensional specification for scaffold geometry fabrication by defining the process parameters in 3DP that may be used further in scaffold accuracy optimization.

2.2.1 The designed geometry

Figure 2.5 presents the specimen geometry that was fabricated in this work. The CAD file dimensions for the cross members were 300 x 300, 400 x 400 and 500 x 500 micrometers and 5 mm in length. Three beams with these dimensions were printed in each test sample. Screening experiments were performed by printing 0.1 to 1.2 mm square cross section beams. Printed beam cross sections of 200 x 200 micrometer and less were not stable enough after printing to support themselves. The minimum beam cross section of 300 x 300 was therefore chosen for this work. The beam sizes chosen are also typical of scaffold beam sizes used in tissue engineering. The geometries for the accuracy measurements were designed using the SolidWorks CAD (SolidWorks Inc., Concorde, MA, USA) program. A ZPrinter 310 (Z Corporation, Burlington, MA) was used to produce the 3DP structures.

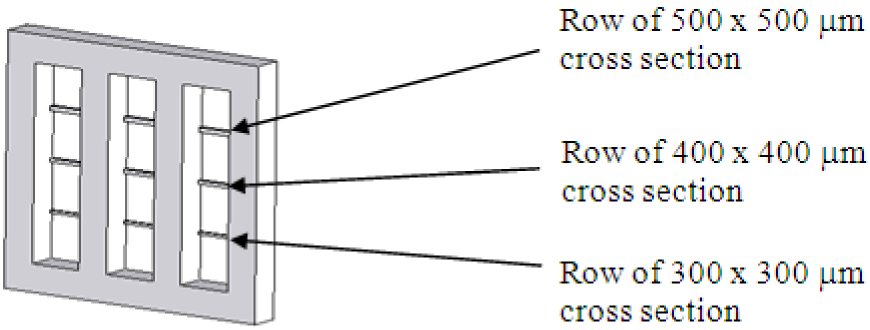

Figure 2.5 Schematic of the fabricated test frame geometry.

2.2.2 Investigated process parameters

Five different process parameters were investigated. These included location in the x and y axis on the 3DP build bed, the orientation with respect to the machine orthogonal axis, the saturation level, and the beam size (300, 400 and 500 micrometer). Three levels of each of these five parameters were chosen and used in a full factorial design of experiments. Table 2.1 summarizes the studied factors and the levels of these factors. For each powder, this resulted in 243 printed test frames fabricated with the associated process parameter combinations. An average value and confidence interval of the beams of similar size were calculated and recorded for each frame structure. In every case the specimens were printed with 0.0875mm layer thickness, bleed compensation set to off and they were left to dry for 24 hours before depowdering. Further description of the factors is presented below.

Levels	**Shell saturation**			**Size**	**Orientation**	**X position**	**Y position**
	Saturation level	Actual binder/volume ratio					
		zp 102	zp 130				
Level 1	75%	0.281747	0.172178	0.3 mm	X	Left	Left
Level 2	100%	0.229571	0.375662	0.4 mm	Y	Center	Center
Level 3	125%	0.469578	0.286964	0.5 mm	Z	Right	Right

Table 2.1 Factors and levels in the design space for the zp102 and zp130 powders.

Powder type

Two different plaster powders were used, the well known zp102 and the relatively new zp130 with the appropriate binders zb56 and zb58 respectively. According to the manufacturer's specification the zp130 provides improved feature definition that has been investigated in this work. The main difference in processing the two powders is that zp102 powder needs more time to reach its full strength since higher saturation levels are used for this powder both in the shell and the core. The printing speed is higher for the zp130 powder for the same reason. New batches of powder were used for this work and the particle size distributions were analyzed before being used for both powders using the Malvern Mastersizer S (Malvern Ltd., Malvern, UK) particle analyzer.

Shell saturation level

The saturation level determines the depth of binder penetration within the powder [98]. In general increasing the saturation level results in higher strength while lower saturation levels makes depowdering easier. Saturation levels can be set selectively for the shell and core of the part. The default level is noted as 100% for both the shell and the core however the actual saturation is noted as binder volume ratio. This ratio indicates that on default settings the printer head uses higher saturation on the shell. The recommended saturation settings vary with the powder type. In this work saturation levels of 75%, 100%, and 125% were analyzed for both powders. These settings automatically equate to different binder/powder volume ratios depending on the powder selected in the ZPrint software. The levels were selected such that the 125% saturation of the zp130 provided the same binder/powder ratio as the 75% level for the zp102.

Part position

Part accuracy may depend on the position of the part in the build chamber, although this effect may vary with machine type and actual condition. In this paper the parts were positioned to 9 different locations. The coordinates of the 9 specimens are depicted in Figure 2.6 and presented in Table 2.2. The origin used in this work is shown Figure 2.6.

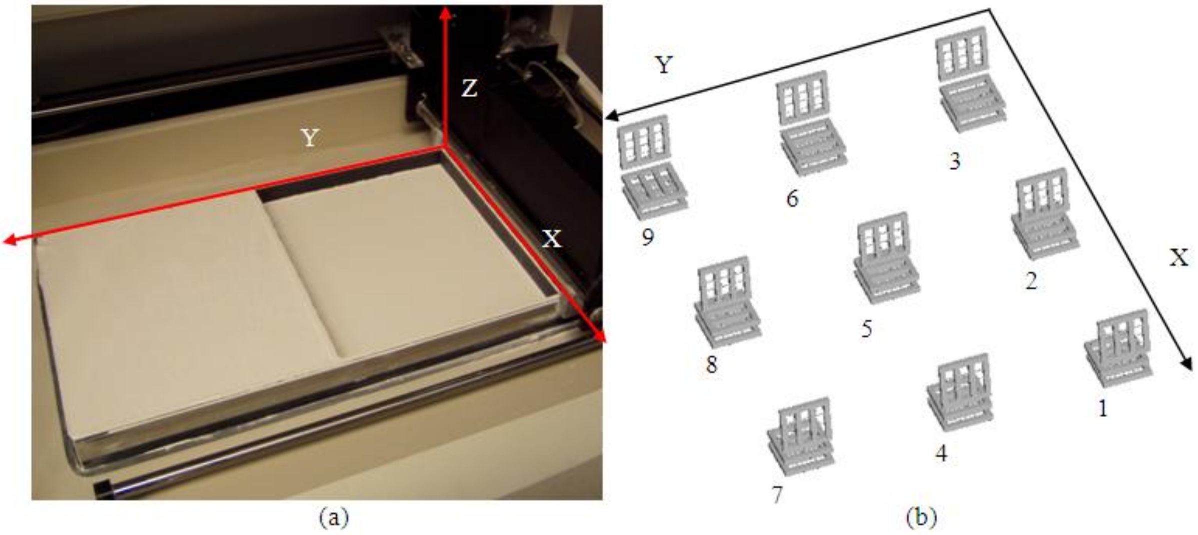

(a) (b)

Figure 2.6 (a) Picture of build chamber and co-ordinate system used and (b) indication of the locations of the specimens within the build chamber.

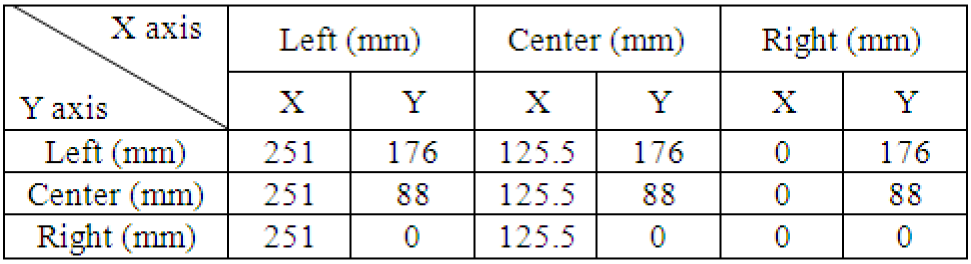

X axis / Y axis	Left (mm)		Center (mm)		Right (mm)	
	X	Y	X	Y	X	Y
Left (mm)	251	176	125.5	176	0	176
Center (mm)	251	88	125.5	88	0	88
Right (mm)	251	0	125.5	0	0	0

Table 2.2 Coordinates of the locations at which the parts were printed.

Orientation

Dimensional accuracy of the part is determined by the powder particle size in every direction but the accuracy in the x-y plane in more constrained by the hardware and control software. The resolution in the x (fast) and y (slow) axes depends on the printer head type (300 dpi) and the printing method. The actual size of the features in the z direction depends on their position along the z axis. If the feature size in the z direction is smaller than the layer thickness, the replicated size will either be the layer thickness or twice the layer thickness as the feature can be positioned within one or between two layers. This means printing a 0.4 mm thick feature with 0.0875mm layer thickness can result in five (5 x 0.875=4.375 mm) or six layers (6 x 0.875= 5.25 mm) according to its position along the z axis. The accuracy of the 3DP system in the x, y, and z directions was assessed by printing specimens with the examined dimensions in these directions as shown in Figure 2.7.

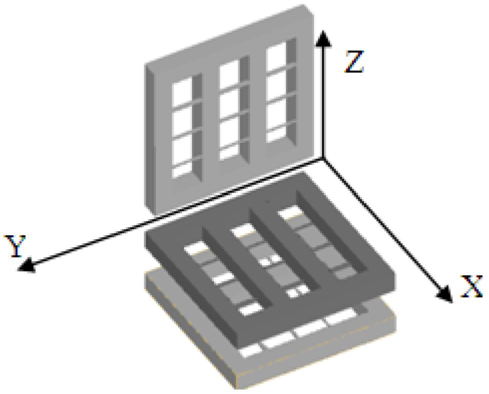

Figure 2.7 Schematic of the orientation of the printed test frames
in location three, six and nine

2.2.3 Measuring Accuracy

The beams were measured using image analysis of micrographs from a Reichert MeF2 (Reichert, Vienna, Austria) inverted light optical microscope from one direction, that is the beams that were oriented in the x and y directions were measured in the x-y plane while the beams in the z direction were measured in the y-z plane. First, the captured images were thresholded and then the average chord length in the horizontal direction was calculated using the Buehler Omnimet image analysis software (Buehler Ltd. Lake Bluff, IL, USA) (Figure 2.8). On each specimen the nine beams were measured separately, the average of the three measurements for beams of similar size was calculated and recorded. An accuracy value of comparison for the beams was calculated by dividing the measured values by the nominal dimensions. The results of the full factorial design were analyzed and evaluated with Design-Expert 7.0 design of experiments software (Stat-Ease Inc. Minneapolis, MN, USA).

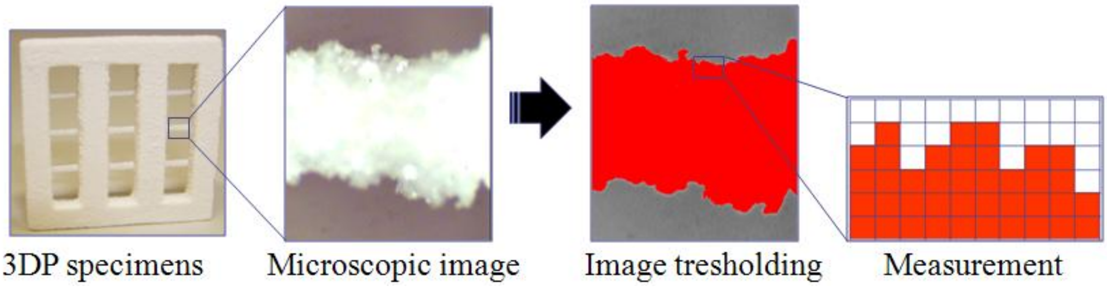

Figure 2.8 The process of measuring accuracy

2.3 3D Printing of Calcium Phosphate Cements (CPC)

A key advantage of 3DP is that a large variety of materials can be used given that they are available in the form of powder [82] Calcium phosphate ceramics were chosen due to their biocompatibility, bioactivity, successful clinical history and similarity to the mineral phase of natural bone. The use of calcium phosphate ceramics for 3DP was previously demonstrated by several authors [70, 71, 85, 92, 99]

This section investigates the possibility of using calcium phosphate based ceramics as raw materials in 3D Printing (3DP) to manufacture freestanding hydroxyapatite (HA) and β-Tricalcium Phosphate (β-TCP) composite scaffolds for bone replacement purposes. 3D Printing is a promising technology for fabricating scaffolds for tissue engineering applications as it enables the fabrication of porous materials with pre-designed internal and external geometry. Since hydroxyapatite is a natural constituent of bone it is a widely investigated and applied material for bone replacement and augmentation. In the current set of experiments calcium phosphate ceramic scaffolds were formed during the printing process as a result of a reaction of two calcium phosphate based ceramics and an aqueous sodium phosphate solution. The calcium phosphates powders used were Dicalcium Phosphate Anhydrous (DCPA, $CaHPO_4$) and calcium hydroxide ($Ca(OH)_2$) while aqueous sodium phosphate solution was used as binder and also as the initiator of the reaction. X-ray diffraction (XRD) was applied to confirm the presence of β-TCP in the fabricated scaffolds and to identify its percentage compared to the raw materials (DCPA and calcium hydroxide). Mechanical testing of the fabricated specimens was performed and the strength and stiffness characteristics were obtained. The effect of the sintering procedure was examined using Scanning Electron Microscopy (SEM) and thermal analysis (DTA/TGA).

2.3.1 Materials

Medical grade Dicalcium Phosphate Anhydrous (DCPA, $CaHPO_4$, Lianyungang Debang Fine Chemical Co., Lianyungang, China) – a biocompatible and biodegradable calcium phosphate and calcium hydroxide ($Ca(OH)_{2,}$ 12038 Sigma-Aldrich, Schnelldorf, Germany) were dried separately for 3 hours at 135 °C. Since the hydrophilicities of the two materials were different, it was important that these materials were weighed after removal of their water content. After drying, DCPA and $Ca(OH)_2$ were quantified stoichiometrically in a 5/3 molar ratio of Ca to P and then were mixed in a V-blender for 30 minutes at 40 rpm. For each batch of printing 500ml of 0.4M aqueous sodium phosphate solution (Na_2HPO_4,S7907 Sigma-Aldrich, Schnelldorf, Germany) was prepared.

2.3.2 3D Printing of CPC samples

The powder mixture was loaded into a Z310 3D Printer (Z-Corp, Burlington, MA, USA). To prepare the CPC, 0.4 ml solution of binder was necessary for each gram of powder. This ratio was calculated to be equal to a 0.3 binder/powder ratio, which was selected for the new powder settings. Samples were also produced with 0.4 binder/powder ratio since samples with a ratio of 0.3 were proven to be too fragile. These ratios were selected both for the shell and core of the specimens. Bleed compensation was turned off. The sodium phosphate solution was introduced to the printer immediately before the printing process started and purged out after the printing process was finished in order to prevent crystallisation within the printing system. Layer thickness was set to be 0.0875 mm for all fabricated specimens (Figure 2.9).

(a) (b)

Figure 2.9 Photographs of 3D Printed specimens after removal from the powder bed (a) solid block for mechanical testing and (b) test scaffold

2.3.3 Post processing

A sintering method was applied to enhance the mechanical property of printed samples. The samples were sintered at 1100 °C for 1 hour at atmospheric pressure using a heating rate of 4°C/min. All samples were kept in furnace to cool down slowly to room temperature over a 16 hour period.

2.3.4 Mechanical characterization

For the mechanical characterisation cubic samples (10x10x10mm) were manufactured and compressive strength and elastic modulus of the micro-porous samples were determined. Both sintered and un-sintered specimens were compressed with a 1mm/min test speed using a Zwick/Roell Z050 universal testing machine equipped with a 5kN load cell (Zwick GmbH, Ulm, Germany). The results were evaluated with TestXpert II (Zwick GmbH, Ulm, Germany).

2.3.5 Thermal analysis

Differential Thermal Analysis and Thermo-Gravimetric Analysis (DTA/TGA, PL Thermal Sciences Ltd., UK) were performed on the 3D Printed materials before subjecting them to thermal treatment/sintering in order to understand the mechanism of transformation of the calcium phosphate cement into polycrystalline calcium phosphate. The analyses were carried out in air atmosphere using heating rates of 4, 10 and 20 °C/min from room temperature to 1000 °C.

2.3.6 XRD analysis

Phases and phase transformations of the 3D Printed calcium phosphate powders and samples were analysed using X-ray diffraction. Bruker AXS D8 (Bruker GmbH, Karlsruhe, Germany). The diffractometer was operated at 40 kV and 40 mA at a 2θ range of 15–80° employing a step size of 0.02 and a 5s exposure.

The effect of cement powder to mixing liquid (P/L) ratio since it is the main determining factor of porosity and therefore of mechanical properties. Mechanical properties increase exponentially with decreasing porosity [24]. Furthermore, sintering as a post processing technology will be examined for increasing mechanical properties of printed scaffolds. Compressive mechanical properties of printed samples were examined as a function of saturation level that was inversely proportional to the powder to liquid ratio. To increase mechanical properties and obtain hydroxyapatite and β-TCP composites, the printed samples were sintered. The effect of sintering parameters including dwell time and sintering temperature were also examined. X-ray diffraction (XRD) was used to examine material composition at different stages of the manufacturing process and to confirm the presence of HA and β-TCP in the final stage.

The effect of sintering procedure on the surface topology of the samples was examined using scanning electron microscopy (SEM).

Three dimensional printing has the ability to fabricate customized 3-dimensional CaP scaffolds with pre-designed external and internal geometry using calcium phosphate ceramic (CPC) chemistry [85, 92, 93].

2.3.7 3D Printer modifications

To enable the 3D printer to manufacture small specimens with small amount of raw materials required the reduction of the build and feed chamber sizes by the application of a reduction chamber specially designed for this purpose (Appendix A).

To promote a complete reaction the calcium phosphate cements require a high sodium phosphate concentration therefore the original binder container and tubing has been replaced. A magnetic hotplate was used to keep the solution at a constant temperature. The temperature of the liquid was constantly monitored with a digital thermometer. For the overview of the assembly see Figure 2.10

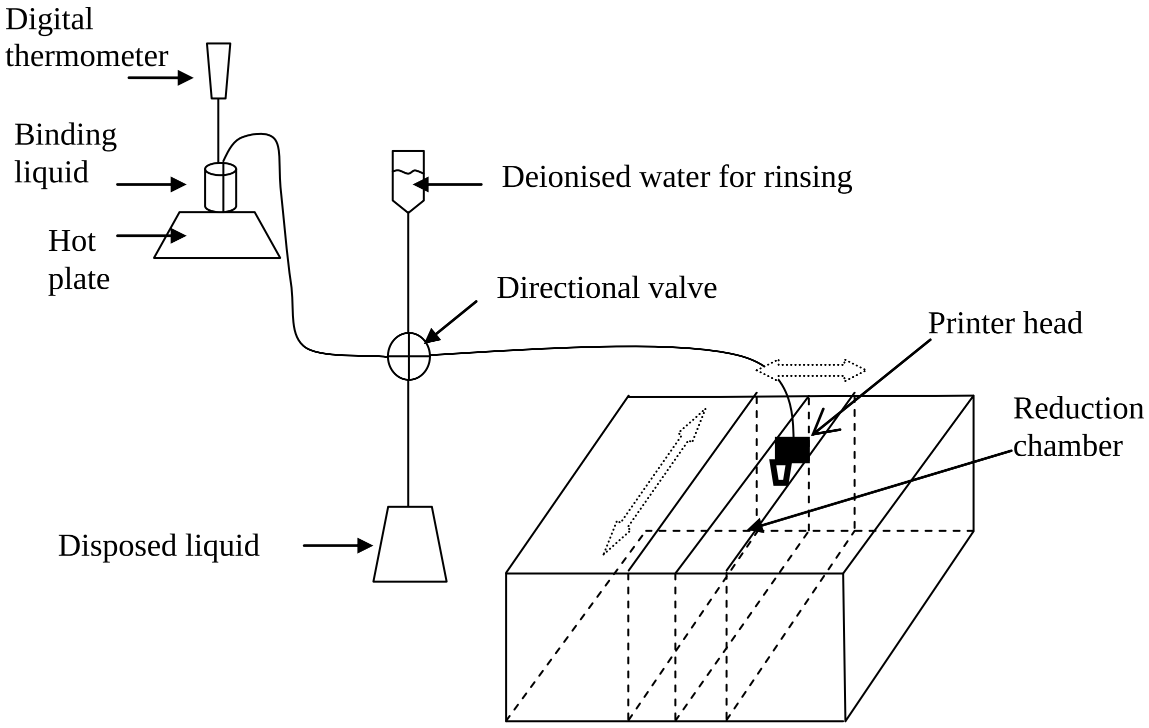

Figure 2.10 Schematic image of the modifications

2.4 Effects of saturation and post processing on porosity and mechanical properties of printed calcium phosphate scaffolds

This section investigates the effect of cement powder to mixing liquid (P/L) ratio since it is the main determining factor of microporosity and therefore of mechanical properties. Mechanical properties increase exponentially with decreasing porosity[24]. Furthermore, sintering as a post processing technology was examined for increasing mechanical properties of printed scaffolds. A homogeneous mixture of medical grade dicalcium phosphate anhydrous (DCPA, CaHPO4, 12038 Sigma-Aldrich) and calcium hydroxide (Ca(OH)2, Lianyungang Debang Fine Chemical Co., Lianyungang, China) was dried and then quantified stoichiometrically in a 5/3 molar ratio of Ca/P. The powders were mixed in a V-blender for 30 min at 40 rpm and then were loaded into a Z310 3 dimensional printer (Z-Corp, Burlington, MA). Sodium phosphate solution (Na2HPO4, S7907 Sigma-Aldrich, Schnelldorf, Germany) was introduced to the mixture through the print-head as the binder material and the initiator of the precipitation reaction.

The effect of P/L ratio and post processing on the porosity and mechanical properties of the scaffolds were examined. The effect of varying saturation levels of printing (i.e. the inverse of P/L ratio) were evaluated at two levels of 0.25 and 0.45. Printed specimens were subjected to sintering at different temperatures of 800, 1000, 1200 ºC for different dwell times of 1, 3, and 5 hours. The heating rate for all specimens was 5 ºC / min.

Phases prior and phase transformations after sintering were analyzed using XRD operated at 40 kV and 40 mA at a 2θ range of 15–60° employing a step size of 0.02 and a 5s exposure. Porosity of raw specimens was tested according to ISO 623-2 using Micrometrics AccuPyc 1330 helium pycnometer. Compressive modulus and yield strength were evaluated at 1 mm/min test speed using Zwick/Roell Z050 universal testing machine equipped with a 5kN load cell. Surface topology was qualitatively evaluated using Scanning Electron Microscopy (SEM, Zeiss EVO LS15).

3 Results

3.1 Mechanical testing and FEA analysis of 3D Printed bone scaffolds

Finitely periodic interconnected scaffolds structures have been fabricated by 3D printing using three different unit cells. The elastic behaviour of each unit cell in different directions was examined by FEA and by experimental compression testing. The same relative directional dependence was determined by both methods. Compressive moduli of all experimentally tested samples were however higher than those determined by the FEA. This could be partly due to dimensional differences between the CAD models and the actual printed geometries. This requires further examination. It is believed that a larger degree of variation however was due to variations in the degree of drying of the printed geometries leading to the observed variations in moduli. This was most noticeable with the control specimens clearly not having dried near the centre. Damper specimens would be expected to behave in a less stiff manner. In order to get a more reliable comparison between the FEA and the 3D printed scaffolds, the same measurements were carried out without infiltration on a more sensitive testing equipment.

3.1.1 FEA results

Solid control specimens were 3D printed and infiltrated. They were subjected to compression testing. The obtained compressive modulus was 490 MPa. This value was not used in the FEA to determine the necessary number of unit cells perpendicular to loading as, although the control specimens were completely infiltrated to their core (5 mm deep), they did not dry within 48 hours. Reported modulus of the epoxy resin is between 2 and 5 GPa [100]. A value of 2 GPa was therefore used for normalisation of the FEA and experimental results. The obtained normalised ($E_{\text{porous structure}}$ / $E_{\text{solid material}}$) elastic modulus values from the FEA for the three different scaffold geometries are presented as a function of loading direction in Figure 3.1.

The directional dependence of the elastic properties of the structures was in good agreement with the results of Luxner et al. [101]. The cubic structure exhibited high stiffness when the unit cells were loaded on their face surface. The normalised compressive modulus ($E_{porous\ structure}/\ E_{solid\ material}$) significantly decreased when the direction of loading was changed. In case of the cylindrical interconnectivity pattern the directional dependence was less significant. The reinforced cubic pattern was the least sensitive to directional loading. It can be observed that non-reinforced structures performed well in uni-axial compression, while the structures with body-centred reinforcements performed better in multi-directional loading cases.

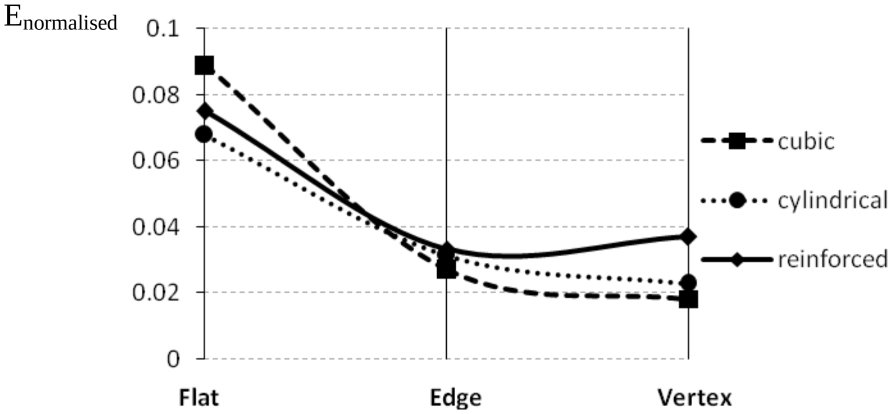

Figure 3.1 FEA determined normalized compressive modulus of all structures with relative density of 20% in three different directions with unit cells are loaded on their flat, edge and vertex surfaces.

3.1.2 Mechanical testing results

Figure 3.2 shows the 3DP geometries that were fabricated. The good macro dimensional resolution achieved can be seen in these pictures and was reflected in the dimensional measurements. Figure 3.3 shows the results of the experimental compression test normalised modulus results. Initial testing with the infiltrated samples showed a degree of variability in the results. This was probably due to the fact that the infiltrant, although present, was not fully hardened in the centre of the specimens. It was noted that the centre of the specimens was damper than their peripheries. As a result of this and to remove this degree of variability, uninfiltrated specimens were fabricated and tested. In all cases the normalised stiffness values from the compression testing with the infiltrated specimens were higher than the values obtained from the FEA, see Figure 3.1 and Figure 3.3. However the trend of decreasing modulus when going from flat to edge to vertex plane loading was obtained by both the FEA and compression experimental testing. Figure 3.3 also shows that the results from the testing of the uninfiltrated samples were more uniform and similar to the FEA results. (For typical stress stain diagrams, see Appendix B.) The infiltration of the different strut sizes may also have influenced the results. Smaller struts would be expected to dry faster after the infiltration and exhibit stiffer elastic behaviour.

	Flat surface loading	**Edge loading**	**Vertex loading**
Cubical	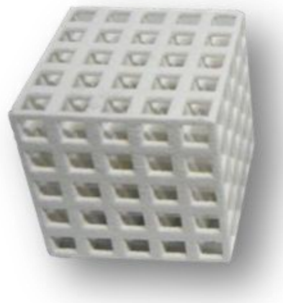		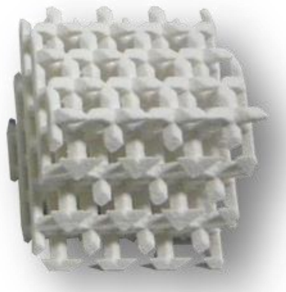
Cylindrical			
Reinforced	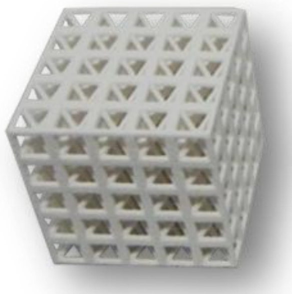	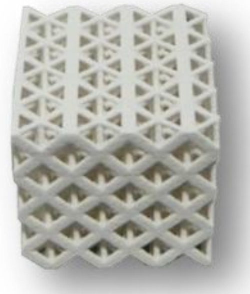	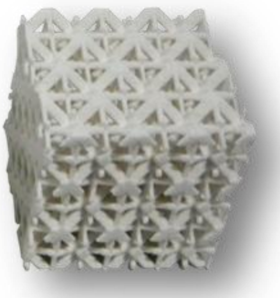

Figure 3.2 3DP scaffolds built from cubic, cylindrical and reinforced cubic unit cells, where the unit cells were loaded in three different directions (flat surface, edge plane, and vertex plane)

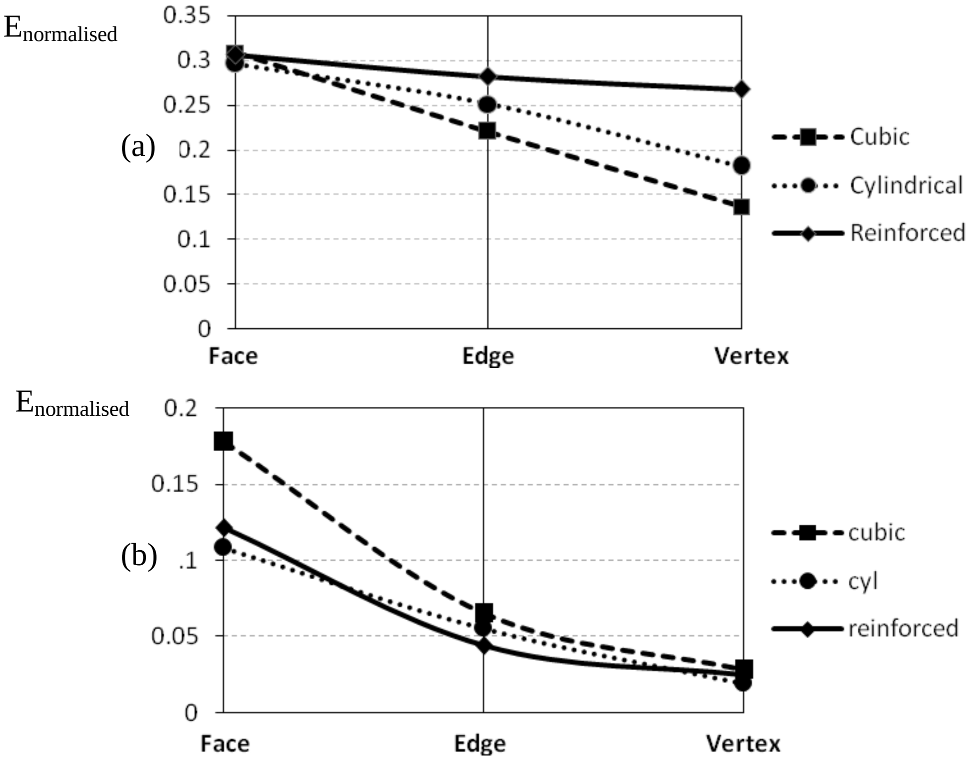

Figure 3.3 Mechanical testing results of the infiltrated (a) and uninfiltrated (b) loading the unit cell patterns in the three directions and for the cubic, cylindrical and reinforced structures. *Note: The values are only connected for better representation and there are no points between the discreet directions.*

3.2 Dimensional accuracy of 3D printed bone scaffold geometries

3.2.1 Particle size

The results for the particle size distribution measurement of both powders are shown in Figure 3.4. There was no significant difference between the mean particle size diameters: it was 41.03µm for the zp102 and 40.79µm for the zp130. The distribution curves showed a noted difference between 2 and 10 µm with a reduced amount of particles present in the zp130 powder. The zp102 had fewer particles between 10 µm and 40 µm but more particles below 10µm. For the zp102 19.3% of the powder particles were between 1 and 10 µm and 32.6% were between 10 and 40 µm. For the zp130 powder these figures were 11.2% and 43.3% respectively.

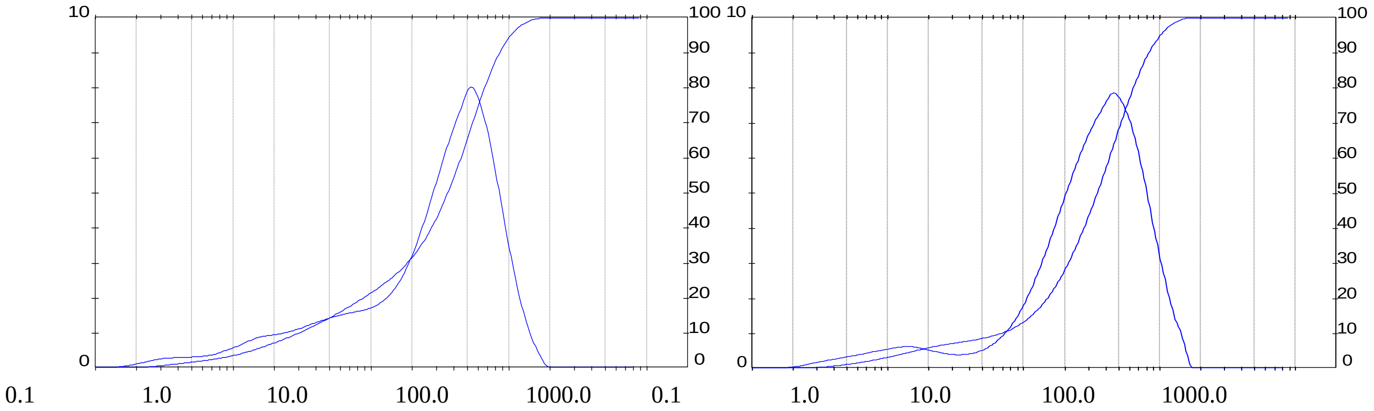

(a) (b)

Figure 3.4 Particle size distributions for (a) zp102 and (b) zp130 powders with the x-axis in micrometers and the secondary y axis shown in percentage.

3.2.2 Analysis of variance

To find the factors that have a significant influence on the accuracy, analysis of variance (ANOVA) was carried out. After eliminating the insignificant interactions the ANOVA results table for the two powders are presented separately in Table 3.1 and Table 3.2.

Source	Sum of squares	Degrees of freedom	Mean square	F value	P value
Model	532362.57	12	44363.55	168.56	< 0.0001
A-Saturation	2.23	1	2.23	0.01	0.9268
B-Size	123249.45	1	123249.45	468.29	< 0.0001
C-Orientation	388540.24	2	194270.12	738.14	< 0.0001
D-X position	183.27	1	183.27	0.70	0.4049
E-Y position	2701.25	1	2701.25	10.26	0.0015
AB	1269.73	1	1269.73	4.82	0.0291
AD	1997.97	1	1997.97	7.59	0.0063
CD	6061.70	2	3030.85	11.52	< 0.0001
A^2	4589.95	1	4589.95	17.44	< 0.0001
B^2	3766.78	1	3766.78	14.31	0.0002
Residual	60533.63	230	263.19	-	-
Total	592896.20	242	-	-	-

Table 3.1 ANOVA table for zp102

Source	Sum of squares	Degrees of freedom	Mean square	F value	P value
Model	867823.29	18	48212.41	311.35	< 0.0001
A-Saturation	6606.40	1	6606.40	42.66	< 0.0001
B-Size	155766.06	1	155766.06	1005.91	< 0.0001
C-Orientation	666043.07	2	333021.54	2150.59	< 0.0001
D-X position	34.15	1	34.15	0.22	0.6391
E-Y position	471.62	1	471.62	3.05	0.0823
AB	1085.68	1	1085.68	7.01	0.0087
AC	11894.83	2	5947.42	38.41	< 0.0001
BC	7958.98	2	3979.49	25.70	< 0.0001
CD	1740.73	2	870.36	5.62	0.0042
CE	1915.44	2	957.72	6.18	0.0024
B^2	13058.95	1	13058.95	84.33	< 0.0001
D^2	540.03	1	540.03	3.49	0.0631
E^2	707.35	1	707.35	4.57	0.0337
Residual	34686.67	224	154.85	-	-
Total	902509.97	242	-	-	-

Table 3.2 ANOVA table for zp130

From the results it can be concluded that the F value was high for both models which means the model was significant and there was only a 0.01% chance that this occurred due to noise. The F values for the factors were calculated by dividing the means square of the factor by the residual mean square. Results with p values less than 0.05 indicate that they are significant factors. According to this, significant factors for zp102 are size, orientation, and y position and for zp130 saturation, size, and orientation are. Several other model terms, interactions are also concerned significant.

3.2.3 Factors and their interaction

The contribution of the most significant factors in is presented at Figure 3.5

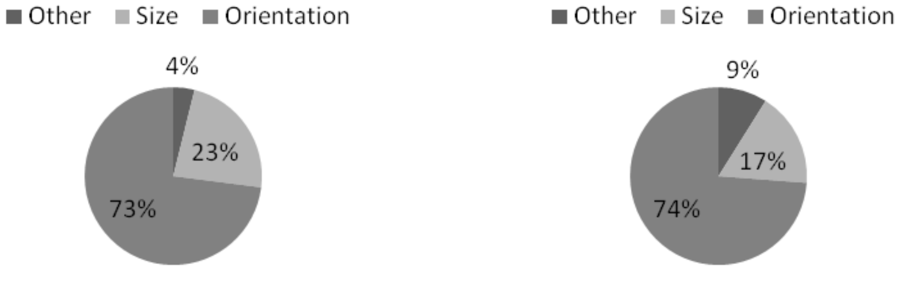

(a) (b)

Figure 3.5 Contribution of the factors in the model for (a) zp102 and (b) zp130.

Figure 3.6 represents the effect of the beam size and the saturation on the normalized accuracy which is noted as the percentage of measured divided by nominal on the y-axis of these graphs. This represents the percentage increase of the prototype dimension over the dimension set in the CAD file. It can be concluded that increasing the size considerably increased the accuracy for both powders. There was little difference between the zp102 and zp130 powder for the 0.3 mm beam size (Figure 3.6) The accuracy was 20% higher with the zp130 powder compared to zp102 powder for the 0.5 mm beam. According to the results of ANOVA in Table 3.1 saturation factor was not significant for the zp102. Using the zp130 powder the higher saturation improved the accuracy although its influence was very small compared to beam size.

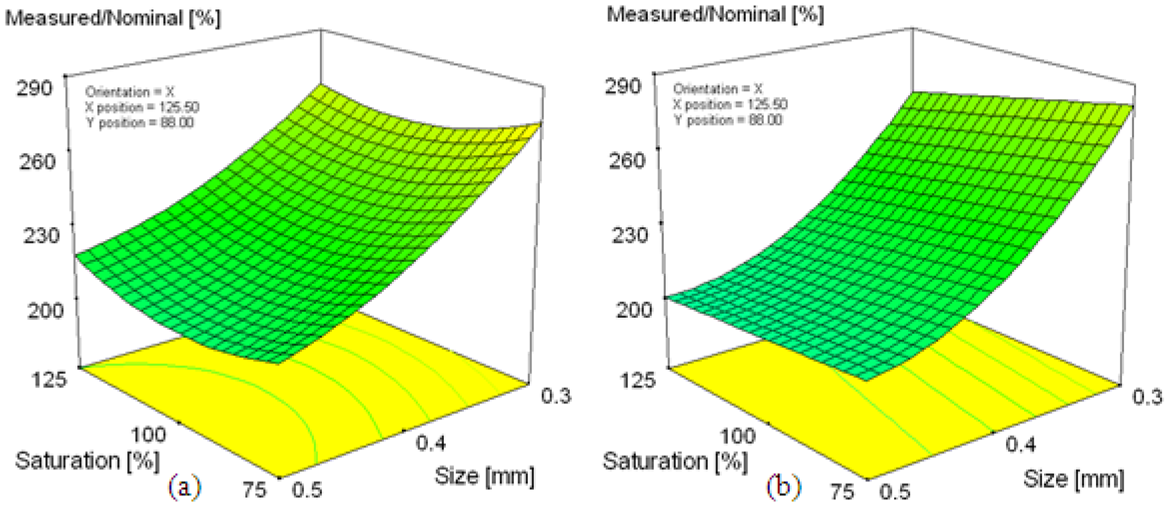

Figure 3.6 Size and saturation factor influence on accuracy for (a) zp102 and (b) zp130

The results that are presented in Figure 3.7 shows that the orientation had the most powerful influence in both powders but especially for the zp130. These results also indicate that there was no considerable difference in the x and y direction for the zp102 but there was 30% (measured/nominal) difference for the zp130. In the z direction the manufactured beam size was significantly lower and closer to the set size. However there was a very large difference between the x and y, and the z axis. This is probably due to the fact that manufacturing in the z direction is less sensitive to the printer head positioning which may be responsible for the higher inaccuracy in the x-y plane.

Figure 3.8 shows the actual sizes of the beams as measured with the Reichert microscope. Examining the actual average measured values for the sizes of 0.3 and 0.4

mm beams it can be established that there is no difference between the figures. The difference between the width of the 0.5 mm and the 0.3 - 0.4 mm beams was between 90 and 120 µm indicating that the machine used the same number of layers when it printed the 0.3 and 0.4 mm size beams and laid one extra layer to print the 0.5 mm beams. These results confirm that the accuracy of the beams in the z direction depends on their actual position along the z axis as described above.

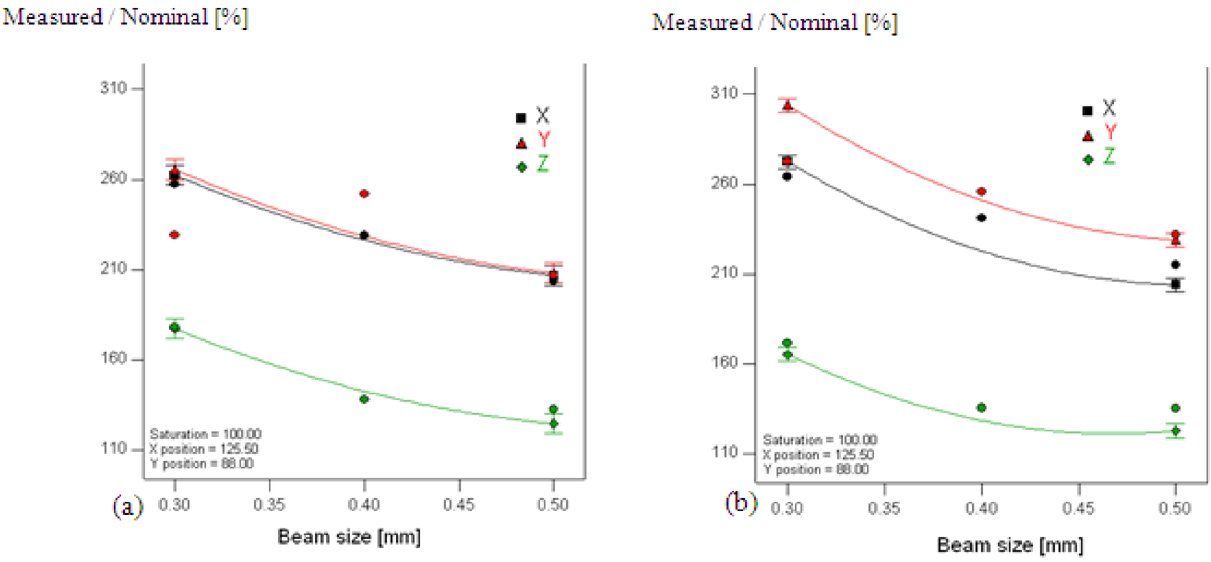

Figure 3.7 Percentage beam accuracy in relation to beam size and orientation at a saturation of 100% for (a) zp102 and (b) zp130.

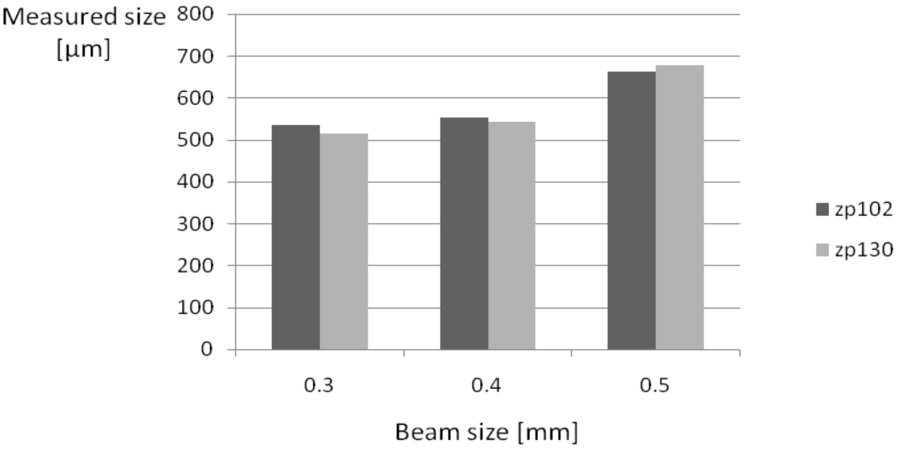

Figure 3.8 Actual measured beam sizes in the z direction at 100% saturation in position five.

Comparing the results for the two powders where the same binder/volume ratio was used (that is 75% for the zp102 and 125% for the zp130) no significant difference in accuracy was detected between the use of the two powders. The saturation settings parameter had very little influence on the accuracy in case of the zp102 powder The effect of saturation was however measurable for the zp130 (Figure 3.9).

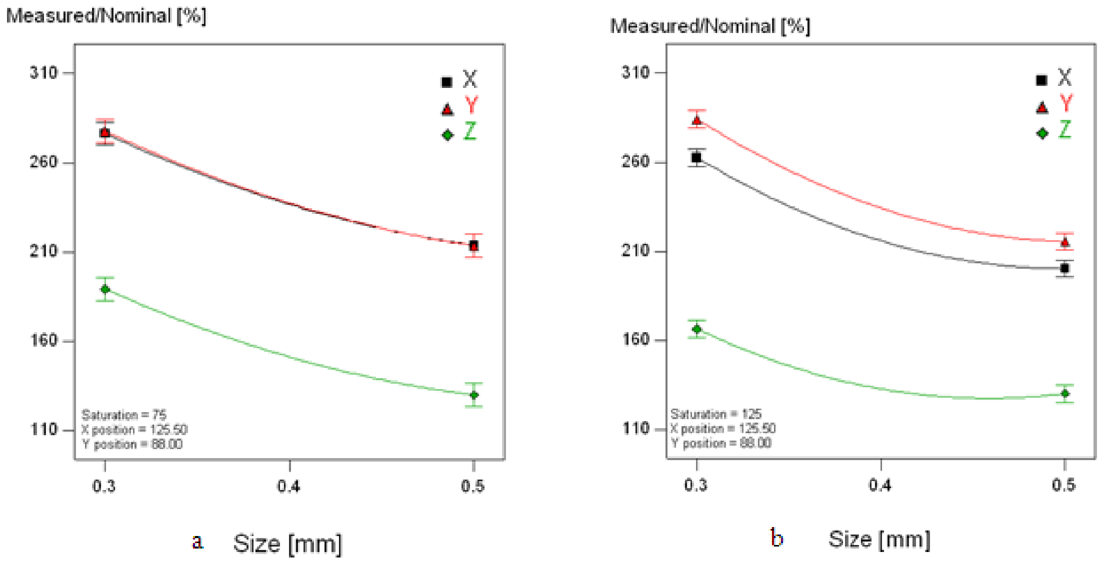

Figure 3.9 Percentage beam accuracy in relation to beam size and orientation at a saturation of 75% for (a) zp102 and at a saturation of 125% for (b) zp130

According to the ANOVA tables the x position is not a significant factor but the part position along the y axis may have some contribution in the final part accuracy. The accuracy maps of the 3D printer were drawn up from the results of the nine different locations, see Figure 3.10 and Figure 3.11

The positions of best accuracy are indicated with "+" symbol and the locations that provided the least accurate beams are noted with "–" symbol. The results did not show significant differences; however with the zp102 powder the positions closer to the x axis did show better accuracy.

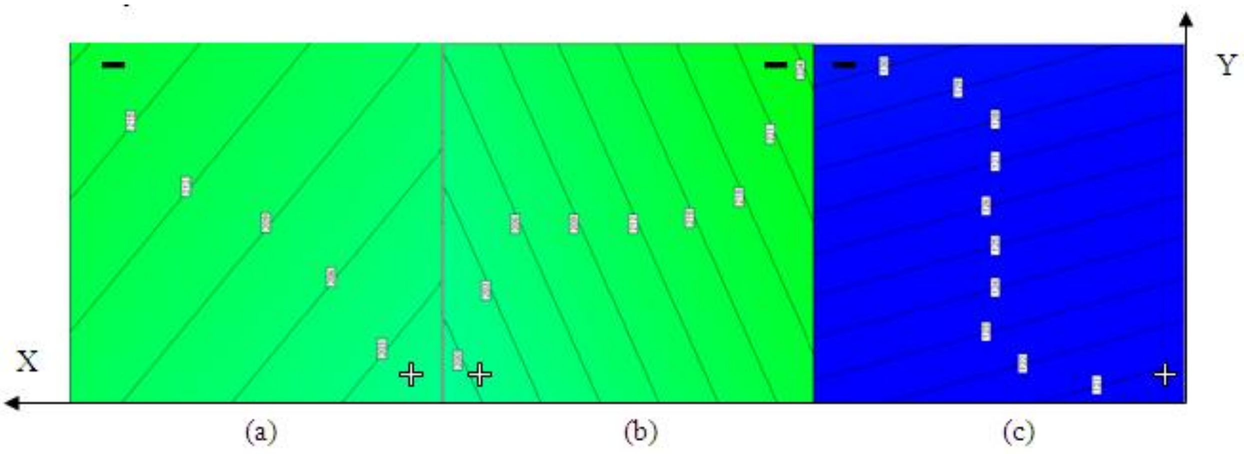

Figure 3.10 Accuracy map of the build chamber for zp102 in (a) x, (b) y, and (c) z orientations.

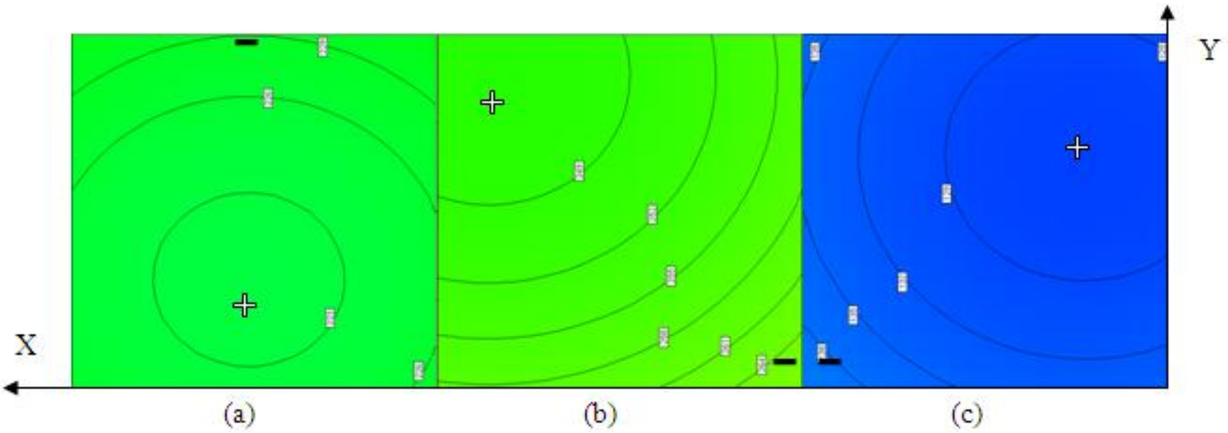

Figure 3.11 Accuracy map of the build chamber for zp130 in x (a), y (b), and z (c) orientations.

Saturation was not seen to have a significant effect for the zp102 powder but larger saturations were seen to increase the accuracy slightly for the zp130 powder. Changing the saturation showed very small influence on the accuracy but low shell saturation levels made the samples very fragile that rendered the specimen removal and depowdering difficult. Comparing the two powder types it can be concluded that there is no substantial difference in accuracy in the examined size range.

The sizes produced in the x and y direction were approximately 2.5 times their nominal dimensions and in the z direction were approximately 1.5 times their nominal dimensions. An improvement in accuracy was noted for larger beam sizes. The measurements in the x and y orientations showed were similar for the zp102 but were better in the x-direction compared to the y-direction for the zp130. The closest recorded result to the 300 μm size was 464 μm which was obtained at 75% saturation, in the z-direction, and with the zp130 powder. The zp130 powder, in the z-direction and with saturation at 75% and 100% produced the smallest deviations from the actual beam set dimension. The lowest percentage deviation was noted for the 0.5 mm with the zp130 powder at about 30%. The zp130 powder produced a deviation on average 51 μm better than with the zp102 in the z-direction. The much better accuracy in the z-direction indicates that the positioning of the printer head in the x and y direction may be the main boundary in manufacturing small features.

Two important factors however affecting the accuracy at this scale are the number of printer head nozzles that are firing and the actual size of the powder layer brought across during the process. The printer head nozzles are arranged in a zigzag pattern with diameters of 60 μm with approximately 25 μm spacing between them. The firing of three of these nozzles would equate to a line of binder of approximately 255 μm and four to a line of 340 μm. The discrete nature of this process results in a compromised resolution in the y direction on levels examined in this work. The powder layer will also be variable to the extent that the powder with particle sizes ranging from 0 to 200 μm will lead to a variable layer height somewhere in between depending on packing density and pressure that may also contribute to the accuracy in the z direction. The position along the z axis may also influence the accuracy however this effect can be easily accounted for as described above. Not withstanding these complications binder bleeding also presents a considerable possibility for deterioration in dimensional tolerances which could justify the oversized beams noted in this work.

The printed 500 μm beam size is viable for scaffold geometries although the accuracy especially in the x-y plane is not acceptable for tissue engineering applications. Part position in the build chamber changes the accuracy somewhat but significant trends could not be detected and its contribution in the results was negligible compared to the other factors.

3.3 3D Printing of Calcium Phosphate Cements (CPC)

3.3.1 SEM

Zeiss EVO LS15 Scanning Electron Microscope (Carl Zeiss SMT AG, Oberkochen, Germany) was used to analyse the effect of the sintering on the structure. Un-sintered specimen surface displays particles that are loosely bonded together and separate particles can be identified. From the image taken from a specimen that was sintered at 1100 ºC it is not possible to distinguish between the particles and the necks between the particles that have been formed during the sintering. The significant drop in the specific surface area after sintering is clearly observable on the SEM images (Figure 3.12). From a tissue engineering point of view it is more advantageous to have rough surfaces with high surface to volume ratio than smooth surfaces; rough surfaces facilitate cell attachment and resorption [82].

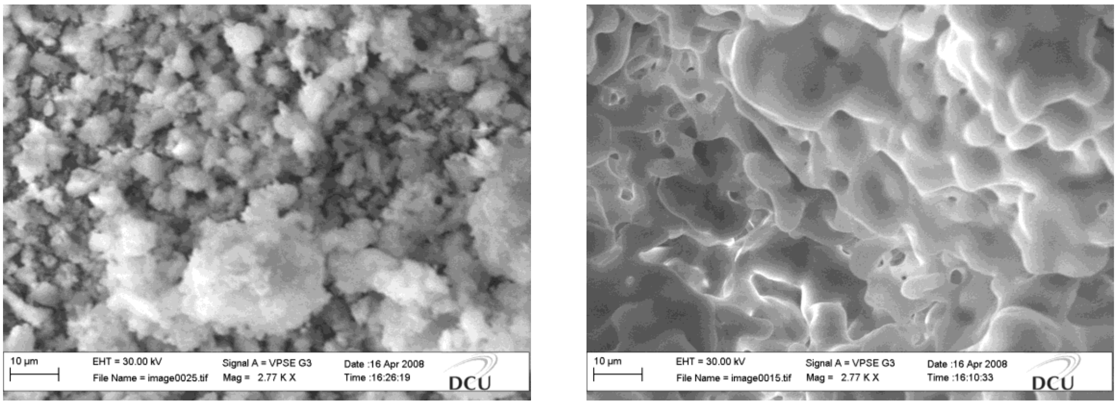

(a) (b)

Figure 3.12 SEM images of scaffold before (a) and after (b) sintering

3.3.2 Mechanical testing

The compressive modulus of natural cancellous bone is reported to be between 20-200 MPa depending on the physiological position, and age [102]. The compressive strength ranges from 1-15 MPa. Compressive modulus and yield strength were calculated for the sintered and raw specimens from the linear elastic region of the specimen behaviour. The Young's modulus for the raw specimens was 3.59 MPa (std. dev. = 0.713) while the yield strength was 0.147 MPa (std. dev. = 0.0429). After sintering these values increased to 9.15 MPa (std. dev. = 1.28) and 0.483 MPa (std. dev. = 0.184), respectively. Currently these results show that the 3DP printed parts are not as strong as natural bone and are therefore not suitable for load bearing applications. However these values can be increased by other post processing methods such as infiltration with biodegradable polymer solutions.

3.3.3 Thermal analysis

The TGA curve reveals a total of 13% decrease in the sample weight, which occurred through several stages. The first mass loss that is related to the dehydration of the specimen took place between 50 and 330 °C. The loss of initial humidity resulted in a 6.5% decrease in weight. The corresponding DTA curve in this temperature range shows a broad asymmetrical endothermic peak that confirms the intensive initial water loss during the rearrangement of the structure. The water loss is more intensive in the beginning and slows down as the endothermic peak is reached.

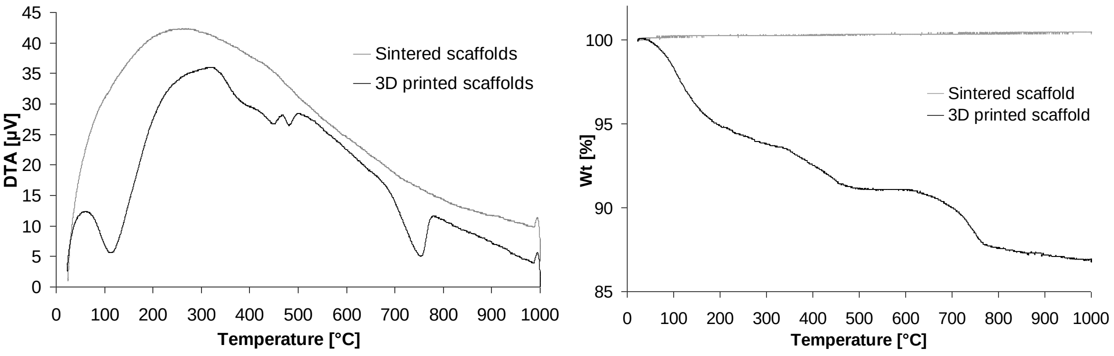

(a) (b)

Figure 3.13 (a) DTA and (b) TGA curve for the 3D printed CPC scaffolds and post-processed (sintered) β-TCP scaffold.

The elimination of free hydroxyl groups is followed by another broad and asymmetric endothermic peak in the DTA curve between 330 and 470 °C. In this region a weight loss of 2.5% at a constant rate is observed on the TGA curve. This thermal phenomena may be due to the dehydration of dicalcium-phosphate($CaHPO_4$) to calcium pyrophosphate (β -$Ca_2P_2O_7$) and the decomposition of $Ca(OH)_2$ to CaO. A similar peak was previously reported [103] at 470°C for CDPA and $Ca(OH)_2$ mixtures. In the next stage significant deceleration of weight loss was observed in the TGA resulting in less than 0.25% of weight loss, corresponding to the endothermic peak in the DTA between 470 °C and 500 °C. The following region starts at 500°C and ends at 630 °C, it lacks thermal events and weight loss. The last endothermic event takes place between 630 °C and ~750 °C. Depending on the heating this phase ends between 710°C and 780 °C, the higher value corresponding to higher heating rates. In TGA it is marked with a constant but intensive weight loss of 3.2% and in DTA with an intensive endothermic peak. The corresponding temperatures and peaks are varied due to the variances in heating rate. In general increased heating rate shifted the curve towards higher temperatures.

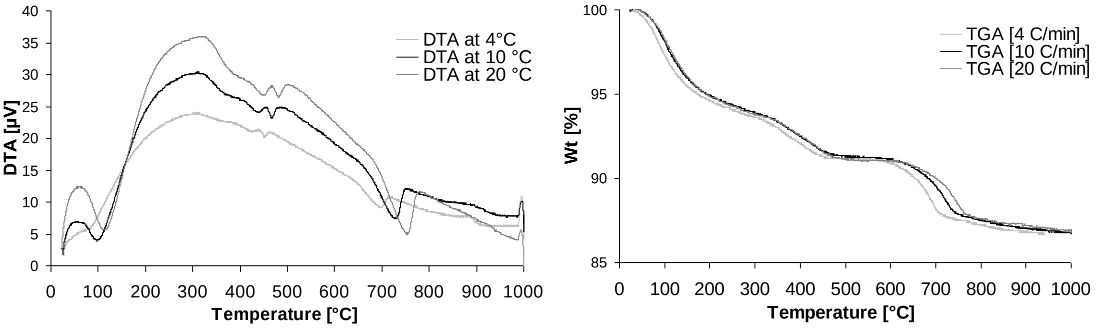

(a) (b)

Figure 3.14 DTA (a) and TGA (b) curve for 3D printed CPC scaffolds at different heating rate.

This last phenomenon indicates the transformation from poorly crystalline calcium phosphate cement to β-TCP. It is suggested that the observed weight loss is due to elimination of free hydroxyl groups indicating the formation of well crystallized β-TCP. After the β-TCP transformation a slight decrease in weight is still observed, however the process is slowed down significantly.

The significance of heating rate can be seen on the TGA/DTA curves. First of all increased heating rate shifted these curves towards higher temperatures and enhanced the heat exchange for each thermal phenomenon. It resulted in increased enthalpy changes indicated by increased peak areas enclosed by the peak and the baseline. These results support the statement that lower heating rates are favourable for the sintering of calcium phosphate cements. The above described thermal analysis confirmed the transformation of the 3D printed CPC to β-TCP below 800 °C for all heating rates. Therefore sintering of specimens was performed above this temperature.

3.3.4 XRD analysis of CaP phase evolution

X-ray diffraction was used as a method to detect phase evolution during the reaction. The XRD data for two starting chemicals (DCPA and $Ca(OH)_2$), printed samples and post-treated samples by sintering at 1100 °C are given in Figure 3.15. In wet-chemical synthesis, Precipitated Hydroxyapatite (PHA) was produced gradually with 3D printing sodium phosphate solution to the mixture of DCPA and $Ca(OH)_2$ powder (Equation 1).

$$CaHPO_4 + Ca(OH)_2 + HPO_4^{2-} \rightarrow Ca_{10-x}(HPO_4)_x(PO_4)_{6-x}(OH)_{2-x} \qquad (1)$$

Aside from PHA, remaining DCPA and $Ca(OH)_2$ phase presented in the printed samples which may have resulted from the limited contact between binder and powder during 3D printing. When heated to above 700 °C, PHA is able of decomposing into β-TCP and HA (1.67 > Ca/P > 1.50) [24]. The ratio of β-TCP and HA reflects the Ca/P of starting chemicals. In the post-treatment of this study, the printed samples were sintered to 1100 °C. Both β-TCP and HA phases were detected in these samples. The reaction that took place here may be described as follows (Equation 2):

$$Ca_{10-x}(HPO_4)_x(PO_4)_{6-x}(OH)_{2-x} \rightarrow \beta\text{-}Ca_3(PO_4)_2 + Ca_{10}(PO_4)_6(OH)_2 \qquad (2)$$

Meanwhile, the remaining DCPA and $Ca(OH)_2$ phase in the printed sample might follow different evolution path to form β-TCP as equation (3-5):

$2CaHPO_4 \rightarrow Ca_2P_2O_7 + H_2O$ (3)

$Ca(OH)_2 \rightarrow CaO + H_2O$ (4)

$Ca_2P_2O_7 + CaO \rightarrow \beta\text{-}Ca_3(PO_4)_2$ (5)

Equation (3) and (4) were evidenced by the endothermic peaks between 400-500 °C and the Equation (5) could be assigned to the endothermic peak at 700-800 °C. All these thermal events were consistent with previous study by Niu Jinlong [103].

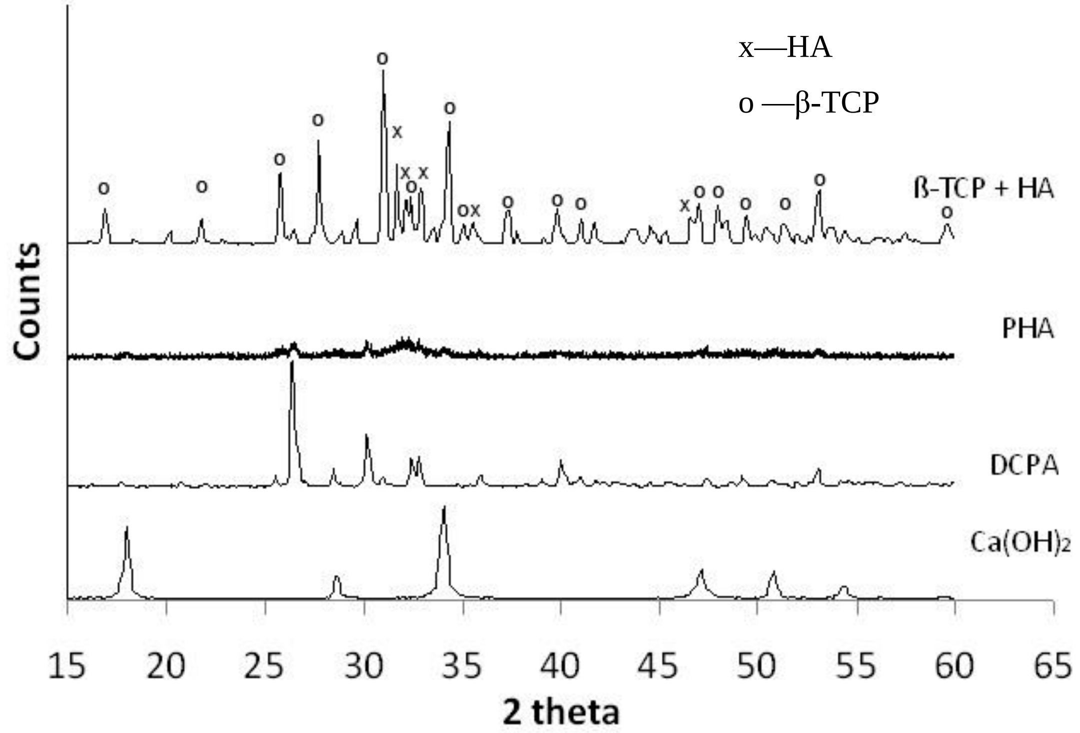

Figure 3.15 XRD patterns for raw materials and scaffold samples.

3.4 Effects of saturation and post processing on porosity and mechanical properties of printed calcium phosphate scaffolds

XRD data showed that precipitated hydroxyapatite (PHA) was produced gradually by 3D printing sodium phosphate solution to the mixture of DCPA and $Ca(OH)_2$ powder. Aside from PHA, remaining DCPA and $Ca(OH)_2$ phases were present in the printed samples. The presence of starting chemicals in the printed samples is an indicator of incomplete chemical reaction and limited contact between binder and powder during the printing. It was also observed that the sintered PHA specimens were able to decompose into β-Tricalcium Phosphate (β-TCP) and Hydroxyapatite (HA).

Additionally to the observed PHA, remaining DCPA and $Ca(OH)_2$ phases were also present in the printed samples. This was possibly due to limited contact between binder and powder during 3D printing and is an indicator of incomplete chemical reaction. Depending on the Ca/P ratio of the starting materials, when heated to above 700 °C, PHA is capable to decompose into β-TCP and HA ($1.67 > Ca:P > 1.50$)

Saturation was found to be the most significant parameter influencing compressive properties. Compressive strength of printed, unsintered samples increased from 0.06 to 0.21 MPa while their stiffness increased from 1.8 to 9.5 MPa by increasing saturation level from 0.25 to 0.45. Porosity values of 79% and 76.8% were recorded for saturation levels of 0.25 and 0.45 respectively. Results showed that when the saturation level was low mechanical properties deteriorated. This was not consistent with previous findings of Bohner e*t al*. [24]. It is believed that the poorer mechanical properties at the lower saturation level was due to incomplete wet chemical synthesis resulting from limited contact between the powder and the liquid phase. This assumption was supported by XRD results as remaining DCPA and $Ca(OH)_2$ phases were detected in printed specimens. The same tendency was observed for compressive modulus on specimens sintered at various temperatures as it increased from 0.09 to 0.356 MPa with increase from saturation level of 0.25 to 0.45.

Sintering significantly improved compressive behaviour of the samples printed at low saturation levels. The modulus, E, increased from 1.8 MPa up to a maximum of 4.3 MPa and compressive yield strength, σ_{cy}, increased from 0.06 MPa up to a maximum of 0.156 MPa. Smaller increases in modulus and strength were noted for the higher saturation level after sintering. The modulus increased from 9.5 MPa up to a maximum of 11.1 MPa and compressive yield strength increased from 0.21 MPa up to a maximum of 0.35 MPa. Sintering time had no significant effect within the examined range indicating that decomposition time to HA and β-TCP is less than 60 minutes. Increased sintering temperatures resulted in improved mechanical properties possibly suggesting that to complete decomposition of HA temperatures higher than 800 ºC are required.

It can be seen in the SEM images (Figure 3.16) that on the surface of un-sintered specimens' surface separate particles can be observed and particles are loosely bound together. On the sintered samples neck formation and particle coalescence are prevalent. The significant drop in the specific surface area after sintering is clearly visible on the images, however from tissue engineering point of view it is more advantageous to have rough surfaces with high surface to volume ratio than smooth surfaces. Rougher surfaces facilitate cell attachment [82].

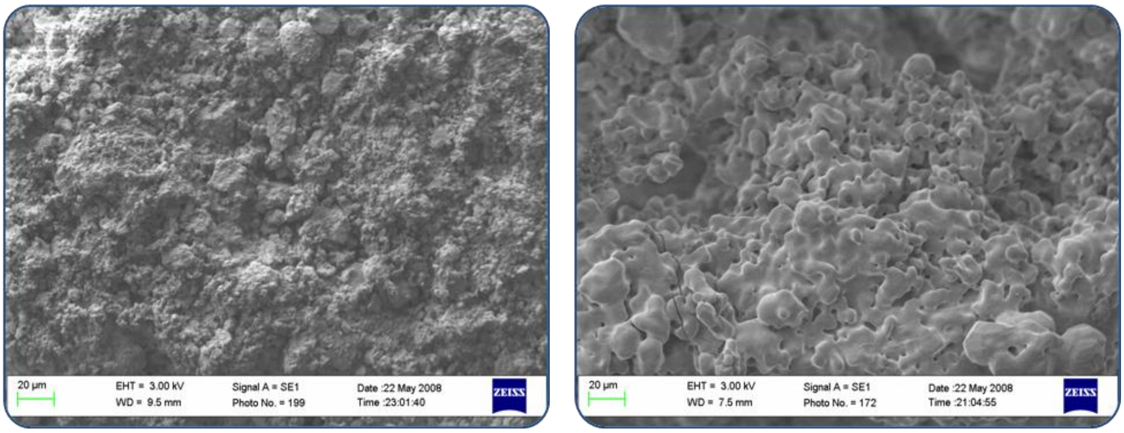

(a) (b)

Figure 3.16 SEM images before (a) and after (b) sintering

4 Discussion

Mechanical testing and FEA analysis

The first set of experiments demonstrated the abilities and the limitations of the 3D printing technique to manufacture complex geometries with intricate internal architecture. It was found that the pre-designed, directional dependent mechanical behaviour of the scaffold geometries can be implemented. However compressive moduli of all experimentally tested samples were higher than those determined by the FEA. As it was confirmed in chapter 3.2.3 this inaccuracy was due to dimensional differences between the CAD models and the actual printed geometries. Comparison of these results with more homogenous patterns produced with other RP techniques would allow further examination of this effect.

Infiltration of scaffold geometries can significantly increase the yield strength although uneven distribution of the resin and uneven drying might introduce some uncertainty into the process. However the efficiency of the infiltration can be improved by using a vacuum chamber. It is believed that a degree of the variation in mechanical properties was due to variations in the degree of drying between the printed geometries. This was most noticeable with the control specimens clearly not having dried near the centre. Damper specimens would be expected to behave in a less stiff manner.

For the uni-axial load testing, the cubic cell structure produced the highest stiffness when the loading was applied directly on the faces. However, if the scaffold is required to work in a multi-directional loading environment. It was shown in this work that reinforced unit cells provide better structural stability. In general, non-reinforced structures performed well in uni-axial compression, while the structures with body-centred reinforcements performed better when loaded from other directions. Infiltration significantly increased the yield strength (by 21 to 114 times), but reduced repeatability of the process. Although the measurements were conducted with proprietary raw materials, the values were normalised thus making it possible to apply the results to any other material of known bulk stiffness.

Dimensional accuracy

As it was mentioned before accuracy is a crucial factor when the scaffold models are to be implemented in practice. The dimensional accuracy of the 3D printer and its dependence on process parameters including: core and shell saturation levels, position within the part bed, designed part feature size and directional dependence on accuracy using two different powders (namely zp102 and zp130) was investigated in detail.

The sizes produced in the x and y direction were approximately 2.5 times their nominal dimensions and in the z direction were approximately 1.5 times their nominal dimensions. An improvement in accuracy was noted for larger beam sizes. The measurements in the x and y orientations were similar for the zp102 but were better in the x-direction compared to the y-direction for the zp130. The closest recorded result to the 300 μm size was 464 μm which was obtained at 75% saturation, in the z-direction, and with the zp130 powder. The zp130 powder, in the z-direction and with saturation at 75% and 100% produced the smallest deviations from the actual beam set dimension. The lowest percentage deviation was noted for the 0.5 mm with the zp130 powder at about 30%. The zp130 powder produced a deviation on average 51 μm smaller than with the zp102 in the z-direction. The much better accuracy in the z-direction indicates that the positioning of the printer head in the x and y direction may be the main boundary in manufacturing small features.

Two important factors however affecting the accuracy at this scale are the number of printer head nozzles that are firing and the actual size of the powder layer brought across during the process. The printer head nozzles are arranged in a zigzag pattern with diameters of 60 μm with approximately 25 μm spacing between them. The firing of three of these nozzles would equate to a line of binder of approximately 255 μm and four to a line of 340 μm. The discrete nature of this process results in a compromised resolution in the y direction on levels examined in this work. The powder layer will also be variable to the extent that the powder with particle sizes ranging from 0 to 200 μm will lead to a variable layer height somewhere in between depending on packing density and pressure that may also contribute to the accuracy in the z direction. The position along the z axis may also influence the accuracy however this effect can be easily accounted for as described above. Notwithstanding these complications binder bleeding also presents a considerable possibility for deterioration in dimensional tolerances which could justify the oversized beams noted in this work.

3D Printing of Calcium Phosphate Cements (CPC)

After exploring the capabilities of 3DP system, and mapping the effect of process parameters using the default powder, the next task was the introduction of a biocompatible material composition into the system. The aim was to demonstrate the ability of the 3DP to produce biocompatibe and biodegradable ceramic scaffolds using calcium phospahate cement chemistry.

Scaffolds were manufactured by printing aqueous sodium phosphate dibasic solution on the powder bed consisting of a homogeneous mixture of dicalcium phosphate and calcium hydroxide. The wet-chemical reaction of precipitation took place in the powder bed of the 3D printer. The manufactured samples were hard to handle as they were extremely fragile. Solid specimens were also fabricated in order to measure the bulk compressive mechanical properties of the fabricated CPC. Other approaches have been made to use biodegradable ceramic composition to print scaffolds for tissue engineering applications. Gbureck et al. used TCP powder with diluted phosphoric acid (H_3PO_4) solution as a binder [93]. The fabricated brushite/TCP implants were of high dimensional accuracy, although its value was not reported.

The average elastic modulus for the green parts after printing was 3.59 MPa and the average compressive strength was 0.147 MPa. In order to increase the mechanical properties of the fabricated materials, they were sintered at 1100 ºC for 1 hour. Sintering resulted in significantly increased compressive properties ($E = 9.15$ MPa, $\sigma_y = 0.483$ MPa), but it decreased the specific surface area of the material. As a result of sintering, the calcium phosphate cement decomposed to β-TCP and HA as confirmed by TGA/DTA and XRD. The mechanical properties reported by CPC producers are not documented so it is difficult to compare different apatite CPCs. Several authors have attempted to compare commercially available CPC cements. For example, Driessens obtained the following compression strength at the given porosity level [104]:

(i) Norian SRS: 33±5 MPa with 50% porosity

(ii) Cementek: 8±2 MPa (porosity not indicated)
(iii) Biocement D: 83±4 MPa with 40% porosity
(iv) a-BSM: 4±1 MPa with 80% porosity

The porosity of CPCs fabricated by 3DP and presented in this thesis was between 70 and 80 %, but their mechanical properties, even in case of the post processed (sintered) samples were one order of magnitude below the values indicated by Driessens et al. To efficiently produce CPCs from DCPA and $Ca(OH)_2$ mixtures, not only does the Ca/P ratio of the powders have to be kept at 1.67, but also as indicated by Takagi it is crucial that the reaction takes place in an environment with high phosphor concentration [105]. It was demonstrated by Driessens et al. that the effective way to keep the phosphate concentration high is to dissolve non-calcium containing salt of phosphoric acid in the liquid phase of the cement [106]. It was found that raising the pH to over 12.7 increased the solubility of DCPA, therefore releasing more phosphate ions. Gbureck et al. applied a similar basic-acid reaction to the manufacture of bioceramic drug delivery devices and implants [92]. It was found that higher concentration of the phosphoric acid solution should be used for more complete conversion of α/β- tricalcium phosphate to brushite (DCPD). Concentrations of the phosphoric acid between 5-30% in the binder solution were investigated and it was found that the compressive strength increased from 0.9 MPa to 8.7 MPa while porosity decreased form 53% to 41% [92]. In order to use the highest phosphor concentration for CPC scaffold fabrication in the current work, the binder feed system of the 3D printer was replaced with a heated container which allowed the binder solution (at 60 ºC) to be stirred ensuring the highest amount of phosphor in solution. The container was held one meter above the 3D printer device to ensure continuous binder flow and correct fluid temperature entering the printer head. For our case the highest concentration of Na_2HPO_4 was 14%. Any value higher than this resulted in immediate crystallization in the tubing and printer head.

Effects of saturation and post processing on porosity and mechanical properties

As indicated by Bohner et al. in terms of mechanical properties, the main determining factor when phosphate cements are fabricated by wet chemical synthesis is the ratio between the amount of cement powder (P) and mixing liquid (L). Bohner et al. found that with high P/L ratio, the porosity of the CPC is low and mechanical properties decrease exponentially with an increase in porosity [24]. When the 3DP technology is used the saturation level – that is the inverse of the powder to liquid ratio – can be accurately controlled. From this previous work, it was expected that an increase in the powder to liquid ratio (decreased saturation) would improve the mechanical properties as it reduces the porosity. However when CPCs were precipitated using the 3DP technology, it was noted that at low saturation levels the mechanical properties were poor. This was contradictory to previous expectations and published literature [24]. Increased saturation levels during printing substantially improved the mechanical properties of the samples. In the present study, this was considered to be due to the lower degree of reaction between the powders and the binder at the lower saturation levels. Takagi et al. indicated that in order to produce HA of 1 mol/*l* concentration, aqueous Na_2HPO_4 solution should be used with a 2.5 P/L ratio [105]. The present study demonstrated that this calculation in not valid for the process if the reaction between the materials was carried out with the 3D printing process.

5 Conclusions and future directions

It was demonstrated that it is possible to produce scaffolds geometries with different mechanical properties by changing merely the unit cell and its orientation. The designed geometries were of high porosity which is one of the main requirements when designing a bone scaffold. It has been also shown that it is possible to tune the stiffness by changing the geometry while keep the porosity on the same level. In this set of experiments the 3DP process parameters were kept constant and used at their default levels. In this initial work, no account of the effect of process parameters on the accuracy of the fabricated parts was considered.

Investigating the dimensional accuracy it was found that the printed 500 µm beam size is viable for scaffold geometries although the accuracy especially in the x-y plane is not acceptable for tissue engineering applications and should be further improved. The sizes produced in the x and y direction were approximately 2.5 times their nominal dimensions and in the z direction were approximately 1.5 times their nominal dimensions. Therefore orientation has been considered as the most significant factor. A considerable improvement in accuracy was noted for larger beam sizes. It was found that saturation was not seen to have a significant effect for the zp102 powder but larger saturations were seen to increase the accuracy slightly for the zp130 powder. Changing the saturation showed very small influence on the accuracy but low shell saturation levels made the samples very fragile that rendered the specimen removal and depowdering difficult. Comparing the two powder types it can be concluded that there was no substantial difference in accuracy within the examined size range. Part position in the build chamber changes the accuracy somewhat but significant trends could not be detected and its contribution in the results was negligible compared to the other factors.

Printing technology is capable to fabricate tissue engineering scaffold geometries made of calcium phosphate cements. Scaffolds were manufactured by printing aqueous sodium phosphate dibasic solution on the powder bed consisting of a homogeneous mixture of dicalcium phosphate and calcium hydroxide. The wet-chemical reaction of precipitation took place in the powder bed of the 3D Printer. The manufactured samples were hard to handle as they were extremely fragile. Solid specimens were also fabricated in order to measure the bulk compressive mechanical properties of the fabricated CPC. The average elastic modulus for the raw parts was 3.59 MPa, and the average compressive strength was 0.147 MPa. In order to increase the mechanical properties of the fabricated materials it was sintered at 1100 ℃ for 1 hour. Sintering resulted in significantly increased compressive properties ($E = 9.15$ MPa, $\sigma_y = 0.483$ MPa), but it decreased the specific surface area of the material. As a result of sintering, the calcium phosphate cement decomposed to β-TCP and HA as confirmed by TGA/DTA and XRD.

Compressive strength and modulus of the CPC scaffolds can be further improved by a controlled sintering process. This effect was more notable at the lower saturation levels with higher sintering temperatures. Furthermore, sintering decreased specific surface area and increased porosity of the specimens. It must be noted that obtained mechanical properties are still not sufficient for load bearing applications.

Further investigations should include other CPC material combinations in to improve the mechanical properties and dimensional accuracy of the raw scaffolds. Improving these would ensure that a smaller viable feature size hence enhancing the usability of the scaffold. Detailed investigation of the sintering process with and infiltration with biodegradable polymers may enable the 3D printing technology to manufacture bone scaffold for load bearing applications.

References

[1] A. C. Guyton, *Textbook of medical physiology*. Philadelphia: Saunders, 1991.

[2] S. Weiner, W. Traub, and H. D. Wagner, Lamellar Bone: Structure-Function Relations, *Journal of Structural Biology*, vol. 126, pp. 241-255, 1999.

[3] S. Dorozhkin, Calcium orthophosphates, *Journal of Materials Science*, vol. 42, pp. 1061-1095, 2007.

[4] S. Weiner and H. D. Wagner, THE MATERIAL BONE: Structure-Mechanical Function Relations, *Annual Review of Materials Science*, vol. 28, p. 271, 1998.

[5] H. Londish, *Molecular Cell Biology*. New York, 1995.

[6] P. Fratzl, H. S. Gupta, E. P. Paschalis, and P. Roschger, Structure and mechanical quality of the collagen–mineral nano-composite in bone, *Journal of Materials Chemistry*, vol. 14, pp. 2115-2123, 2004.

[7] J.D. Zioupos, A. J. Hamer,, The role of collagen in the declining mechanical properties of aging human cortical bone, *Journal of Biomedical Materials Research*, vol. 45, pp. 108-116, 1999.

[8] R. McCalden, J. McGeough, M. Barker, and C. Court-Brown, Age-related changes in the tensile properties of cortical bone. The relative importance of changes in porosity, mineralization, and microstructure, *J. Bone Joint Surg. Am.*, vol. 75, pp. 1193-1205, August 1, 1993.

[9] J.-Y. Rho, L. Kuhn-Spearing, and P. Zioupos, Mechanical properties and the hierarchical structure of bone, *Medical Engineering & Physics*, vol. 20, pp. 92-102, 1998.

[10] J. A. Buckwalter and R. R. Cooper, Bone structure and function, *Instructional course lectures*, vol. 36, pp. 27-48, 1987.

[11] US National Cancer Institute
http://training.seer.cancer.gov/module_anatomy/unit3_2_bone_tissue.html
Accessed on 04/08/2008

[12] E. B. Antonio Ascenzi, The compressive properties of single osteons, *The Anatomical Record*, vol. 161, pp. 377-391, 1968.

[13] E. N. Marieb, *Human anatomy and physiology*, 5th ed.: Benjamin-Cummings Publishing Company, 2001.

[14] J.Y. Rho, M. C. Hobatho, and R. B. Ashman, Relations of mechanical properties to density and CT numbers in human bone, *Medical Engineering & Physics*, vol. 17, pp. 347-355, 1995.

[15] D. T. Reilly and A. H. Burstein, The Mechanical Properties of Cortical Bone, *The Journal of Bone and Joint Surgery,* vol. 56, pp. 1001-1022, 1974.

[16] L. J. Gibson and M. F. Ashby, *Cellular Solids: Structure and Properties*: Cambridge University Press, 1997.

[17] J. Wolff, Uber die Bedeutung der Architektur der spongiosen Substanz, *Zentralblatt fur die medizinische Wissenschaft Jahrgang,* vol. VI, pp. 223-234, 1869.

[18] J. Currey, *The mechanical adaptations of bones*: Princeton University Press, Princeton, NJ, 1984.

[19] Bone mass changes, Osteoporosis Clinical Overview http://www.gcrweb.com/OsteoDSS/clinical/path/pages/path-bone-mass.html Accessed on 04/08/2008

[20] S. A. Goldstein, The mechanical properties of trabecular bone: Dependence on anatomic location and function, *Journal of Biomechanics,* vol. 20, pp. 1055-1061, 1987.

[21] S. Wenisch, J. P. Stahl, U. Horas, C. Heiss, O. Kilian, K. Trinkaus, A. Hild, and R. Schnettler, In vivo mechanisms of hydroxyapatite ceramic degradation by osteoclasts: Fine structural microscopy, *Journal of Biomedical Materials Research Part A,* vol. 67A, pp. 713-718, 2003.

[22] W. S. Koegler, "Fabrication of tissue engineering scaffolds with spatial control over architecture and cell–matrix interactions in 3D," in *Department of Chemical Engineering*. vol. PhD Cambridge: Massachusetts Institute of Technology, 2000.

[23] L. C. Chow and W. Brown, "Dental restorative cement pastes." vol. 4518430: US, 1985.

[24] M. Bohner, Calcium orthophosphates in medicine: from ceramics to calcium phosphate cements, *Injury,* vol. 31, pp. 37-47, 2000.

[25] K. Ishikawa, Y. Miyamoto, M. Kon, M. Nagayama, and K. Asaoka, Non-decay type fast-setting calcium phosphate cement: composite with sodium alginate, *Biomaterials,* vol. 16, pp. 527-532, 1995.

[26] J. E. Barralet, L. Grover, T. Gaunt, A. J. Wright, and I. R. Gibson, Preparation of macroporous calcium phosphate cement tissue engineering scaffold, *Biomaterials*, vol. 23, pp. 3063-3072, 2002.

[27] F. C. Driessens, M. G. Boltong, E. A. P. de Maeyer, R. Wenz, B. Nies, and J. A. Planell, The Ca/P range of nanoapatitic calcium phosphate cements, *Biomaterials*, vol. 23, pp. 4011-4017, 2002.

[28] B. D. Ratner, A. S. Hoffman, F. J. Schoen, and J. E. Lemons, *Biomaterials science: An introduction to Materials in Medicine*, 2nd ed. San Diego: Elsevier Acedemic press, 2004.

[29] K. H. Tan, C. K. Chua, K. F. Leong, C. M. Cheah, P. Cheang, M. S. Abu Bakar, and S. W. Cha, Scaffold development using selective laser sintering of polyetheretherketone-hydroxyapatite biocomposite blends, *Biomaterials,* vol. 24, pp. 3115-3123, 2003.

[30] D. W. Hutmacher, Scaffold design and fabrication technologies for engineering tissues - state of the art and future perspectives, *Journal of Biomaterials Science - Polymer Edition*, vol. 12, pp. 107-124, 2001.

[31] B. Y. Tay, S. X. Zhang, M. H. Myint, F. L. Ng, M. Chandrasekaran, and L. K. A. Tan, Processing of polycaprolactone porous structure for scaffold development, *Journal of Materials Processing Technology*, vol. 182, pp. 117-121, 2007.

[32] L. Freed, G. Vunjak-Novakovic, R. Biron, D. Eagles, D. Lesnoy, S. Barlow, and R. Langer, Biodegradable Polymer Scaffolds for Tissue Engineering, *Nature Biotechnology,* vol. 12, pp. 689-693, 1994.

[33] G. E. Zaikov, Quantitative aspects of polymer degradation in the living body, *Polymer Reviews*, vol. 25, pp. 551 - 597, 1985.

[34] R.S. Santerre, G. A. Adams,, Enzyme-biomaterial interactions: Effect of biosystems on degradation of polyurethanes, *Journal of Biomedical Materials Research*, vol. 27, pp. 97-109, 1993.

[35] S. S. Liao, F. Z. Cui, W. Zhang, and Q. L. Feng, Hierarchically biomimetic bone scaffold materials: Nano-HA/collagen/PLA composite*, Journal of Biomedical Materials Research,* vol. 69, pp. 158-165, 2004.

[36] C.V. Rodrigues, P. Serricella, A.B. Linhares, R. M. Guerdes, R. Borojevic, M. A. Rossi, M. E. L. Duarte, and M. Farina, Characterization of a bovine collagen–hydroxyapatite composite scaffold for bone tissue engineering, *Biomaterials,* vol. 24, pp. 4987-4997, 2003.

[37] R. Chandra and R. Rustgi, Biodegradable polymers, *Progress in Polymer Science*, vol. 23, pp. 1273-1335, 1998.

[38] R. L. Whistler, J. N. BeMiller, and E. F. Paschall, *Starch: chemistry and technology*: New York: Academic Press, 1967.

[39] A. J. Salgado, O. P. Coutinho, and R. L. Reis, Novel Starch-Based Scaffolds for Bone Tissue Engineering: Cytotoxicity, Cell Culture, and Protein Expression, *Tissue Engineering,* vol. 10, pp. 465-474, 2004.

[40] N. D. Miller and D. F. Williams, On the biodegradation of poly-beta-hydroxybutyrate (PHB) homopolymer and poly-beta-hydroxybutyrate-hydroxyvalerate copolymers, *Biomaterials,* vol. 8, pp. 129-37, 1987.

[41] S. Gogolewski, M. Jovanovic, S. M. Perren, J. G. Dillon, and M. K. Hughes, Tissue response and in vivo degradation of selected polyhydroxyacids: polylactides (PLA), poly (3-hydroxybutyrate)(PHB), and poly (3-hydroxybutyrate-co-3-hydroxyvalerate)(PHB/VA), *Journal of Biomedical Materials Research,* vol. 27, pp. 1135-48, 1993.

[42] E. A. Dawes and P. J. Senior, The role and regulation of energy reserve polymers in micro-organisms, *Advances in microbial physiology,* vol. 10, pp. 135-266, 1973.

[43] N. Kumar, R. S. Langer, and A. J. Domb, Polyanhydrides: an overview, *Advanced Drug Delivery Reviews,* vol. 54, pp. 889-910, 2002.

[44] I. Engelberg and J. Kohn, Physico-mechanical properties of degradable polymers used in medical applications: a comparative study, *Biomaterials,* vol. 12, pp. 292-304, 1991.

[45] K. E. Uhrich, S. E. M. Ibim, D. R. Larrier, R. Langer, and C. T. Laurencin, Chemical changes during in vivo degradation of poly (anhydride-imide) matrices, *Biomaterials*, vol. 19, pp. 2045-2050, 1998.

[46] A. K. Burkoth and K. S. Anseth, A review of photocrosslinked polyanhydrides: in situ forming degradable networks, *Biomaterials*, vol. 21, pp. 2395-2404, 2000.

[47] A. B. Scranton, C. N. Bowman, and R. W. Peiffer, *Photopolymerization: fundamentals and applications*: American Chemical Society, Washington, DC, 1997.

[48] J. Heller, J. Barr, S. Y. Ng, H. R. Shen, K. Schwach-Abdellaoui, S. Emmahl, A. Rothen-Weinhold, and R. Gurny, Poly (ortho esters)–their development and some recent applications, *European Journal of Pharmaceutics and Biopharmaceutics,* vol. 50, pp. 121-128, 2000.

[49] K. P. Andriano, Y. Tabata, Y. Ikada, and J. Heller, In Vitro and In Vivo Comparison of Bulk and Surface Hydrolysis in Absorbable Polymer Scaffolds for Tissue Engineering, *Journal of Biomedical Materials Research,* vol. 48, p. 602, 1999.

[50] N. M. K. Lamba, K. A. Woodhouse, and S. L. Cooper, *Polyurethanes in Biomedical Applications*: CRC Press, 1998.

[51] R. J. Zdrahala and I. J. Zdrahala, Biomedical Applications of Polyurethanes: A Review of Past Promises, Present Realities, and a Vibrant Future, *Journal of Biomaterials Applications,* vol. 14, p. 67, 1999.

[52] P. A. Gunatillake and R. Adhikari, Biodegradable synthetic polymers for tissue engineering, *European Cells and Materials Journal,* vol. 5, pp. 1-16, 2003.

[53] R. P. Lanza, R. Langer, and J. Vacanti, *Principles of Tissue Engineering*, 2nd ed. San Diego: Academic Press San Diego, CA, 2000.

[54] A. Reed and D. Gilding, Biodegradable polymers for use in surgery-poly (glycolic)/poly (lactic acid) homo and copolymers: 2, *vitro degradation. Polymer,* vol. 22, pp. 494-498, 1981.

[55] J. O. Hollinger, A Preliminary Report on the Osteogenic Potential of a Biodegradable Copolymer of Polylactide: Polyglycolide (PLA: PGA). Revised, *journal of Biomedical Materials Research,* pp. 71-82, 1982.

[56] J. M. Anderson and M. S. Shive, Biodegradation and biocompatibility of PLA and PLGA microspheres, *Advanced Drug Delivery Reviews,* vol. 28, pp. 5-24, 1997.

[57] J. Bronzino, *The Biomedical Engineering Handbook*: Springer-Verlag, 2000.

[58] J. C. Middleton and A. J. Tipton, Synthetic biodegradable polymers as orthopedic devices, *Biomaterials,* vol. 21, pp. 2335-2346, 2000.

[59] C. G. Pitt, "Poly--caprolactone and its copolymers," in *Biodegradable polymers as drug delivery systems*. vol. 71 New York: Marcel Dekker Inc., 1990, p. 120.

[60] L. Shor, S. Guceri, X. Wen, M. Gandhi, and W. Sun, Fabrication of three-dimensional polycaprolactone/hydroxyapatite tissue scaffolds and osteoblast-scaffold interactions in vitro, *Biomaterials,* vol. 28, pp. 5291-5297, 2007.

[61] Y. Lei, B. Rai, K. H. Ho, and S. H. Teoh, In vitro degradation of novel bioactive polycaprolactone--20% tricalcium phosphate composite scaffolds for bone engineering, *Materials Science and Engineering: C,* vol. 27, pp. 293-298, 2007.

[62] B. L. Seal, T. C. Otero, and A. Panitch, Polymeric biomaterials for tissue and organ regeneration, *Materials Science and Engineering: R: Reports,* vol. 34, pp. 147-230, 2001.

[63] M. H. Sheridan, L. D. Shea, M. C. Peters, and D. J. Mooney, Bioabsorbable polymer scaffolds for tissue engineering capable of sustained growth factor delivery, *Journal of Controlled Release,* vol. 64, pp. 91-102, 2000.

[64] J. R. Jones and L. L. Hench, Regeneration of trabecular bone using porous ceramics, *Current opinion in Solid State and Materials Science,* vol. 7, pp. 301-307, 2003.

[65] E. Sachlos and J. T. Czernuszka, Making tissue engineering scaffolds work. Review on the application of solid freeform fabrication technology to the production of tissue engineering scaffolds, *Eur Cell Mater,* vol. 5, pp. 29-39, 2003.

[66] I. C. Bonzani, J. H. George, and M. M. Stevens, Novel materials for bone and cartilage regeneration, *Current Opinion in Chemical Biology,* vol. 10, pp. 568-575, 2006.

[67] D. W. H. Monique Martina, Biodegradable polymers applied in tissue engineering research: a review, *Polymer International,* vol. 56, pp. 145-157, 2007.

[68] E. A. Botchwey, M. A. Dupree, S. R. Pollack, E. M. Levine, and C. T. Laurencin, Tissue engineered bone: Measurement of nutrient transport in three-dimensional matrices, *Journal of Biomedical Materials Research Part A,* vol. 67A, pp. 357-367, 2003.

[69] S. J. Hollister, Porous scaffold design for tissue engineering, *Nat Mater,* vol. 5, pp. 590-590, 2006.

[70] B. Leukers, H. Gülkan, S. Irsen, S. Milz, C. Tille, M. Schieker, and H. Seitz, Hydroxyapatite scaffolds for bone tissue engineering made by 3D printing, *Journal of Materials Science: Materials in Medicine,* vol. 16, pp. 1121-1124, 2005.

[71] H. Seitz, W. Rieder, S. Irsen, B. Leukers, and C. Tille, Three-dimensional printing of porous ceramic scaffolds for bone tissue engineering, *J Biomed Mater Res B Appl Biomater,* vol. 74, pp. 782-788, 2005.

[72] D. W. Hutmacher, Scaffolds in tissue engineering bone and cartilage, *Biomaterials,* vol. 21, pp. 2529-2543, 2000.

[73] C. X. F. Lam, X. M. Mo, S. H. Teoh, and D. W. Hutmacher, Scaffold development using 3D printing with a starch-based polymer, *Materials Science and Engineering: C,* vol. 20, pp. 49-56, 2002.

[74] A. Mikos , Y. Bao, L. Cima, D. Ingber, J. Vacanti, and R. Langer, Preparation of poly (glycolic acid) bonded fiber structures for cell attachment and transplantation, *Journal of Biomedical Materials Research,* vol. 27, pp. 183-189, 1993.

[75] S. S. Kim, H. Utsunomiya, J. A. Koski, B. M. Wu, M. J. Cima, J. Sohn, K. Mukai, L. G. Griffith, and J. P. Vacanti, Survival and function of hepatocytes on a novel three-dimensional synthetic biodegradable polymer scaffold with an intrinsic network of channels, *Ann Surg,* vol. 228, pp. 8-13, 1998.

[76] A. G. Mikos and J. S. Temenoff, Formation of highly porous biodegradable scaffolds for tissue engineering, *Electronic Journal of Biotechnology,* vol. 3, pp. 114-9, 2000.

[77] C. K. Chua, K. F. Leong, and C. S. Lim, *Rapid Prototyping: Principles and Applications*: World Scientific, 2003.

[78] R. Ippolito, L. Iuliano, and A. Gatto, Benchmarking of Rapid Prototyping Techniques in Terms of Dimensional Accuracy and Surface Finish, *CIRP Annals - Manufacturing Technology*, vol. 44, pp. 157-160, 1995.

[79] V. Mironov, T. Boland, T. Trusk, G. Forgacs, and R. R. Markwald, Organ printing: computer-aided jet-based 3D tissue engineering, *Trends in Biotechnology*, vol. 21, pp. 157-161, 2003.

[80] Rapid Product Development Resource Centre http://rpdrc.ic.polyu.edu.hk/content/rp_misc/sls_introduction.htm Accessed on 14/08/08

[81] T. M. G. Chu, J. W. Halloran, S. J. Hollister, and S. E. Feinberg, Hydroxyapatite implants with designed internal architecture, *Journal of Materials Science: Materials in Medicine*, vol. 12, pp. 471-478, 2001.

[82] W.-Y. Yeong, C.-K. Chua, K.-F. Leong, and M. Chandrasekaran, Rapid prototyping in tissue engineering: challenges and potential, *Trends in Biotechnology*, vol. 22, pp. 643-652, 2004.

[83] L. Hao and R. Harris, "Customised Implants for Bone Replacement and Growth," in *Bio-Materials and Prototyping Applications in Medicine*, 2008, pp. 79-107.

[84] Custompart.net http://www.custompartnet.com/wu/fused-deposition-modeling Accessed on 25/09/2008

[85] A. Khalyfa, S. Vogt, J. Weisser, G. Grimm, A. Rechtenbach, W. Meyer, and M. Schnabelrauch, Development of a new calcium phosphate powder-binder system for the 3D printing of patient specific implants, *Journal of Materials Science: Materials in Medicine*, vol. 18, pp. 909-916, 2007.

[86] W. S. Koegler and L. G. Griffith, Osteoblast response to PLGA tissue engineering scaffolds with PEO modified surface chemistries and demonstration of patterned cell response, *Biomaterials*, vol. 25, pp. 2819-2830, 2004.

[87] M. Lee, J. C. Y. Dunn, and B. M. Wu, Scaffold fabrication by indirect three-dimensional printing, *Biomaterials*, vol. 26, pp. 4281-4289, 2005.

[88] H. Seitz, W. Rieder, S. Irsen, B. Leukers, and C. Tille, Three-dimensional printing of porous ceramic scaffolds for bone tissue engineering, *Journal of Biomedical Materials Research Part B: Applied Biomaterials*, vol. 74B, pp. 782-788, 2005.

[89] D. A. Wahl, Z. W. Han, and J. T. Czernuszka, On the manufacturability of scaffold mould using a 3D printing technology The Authors CZ Liu, Department of Materials, University of Oxford, Oxford, UK E. Sachlos, Department of Materials, University of Oxford, Oxford, UK, *Rapid Prototyping Journal*, vol. 13, pp. 163-174, 2007.

[90] C. Weinand, I. Pomerantseva, C. M. Neville, R. Gupta, E. Weinberg, I. Madisch, F. Shapiro, H. Abukawa, M. J. Troulis, and J. P. Vacanti, Hydrogel-[beta]-TCP scaffolds and stem cells for tissue engineering bone, *Bone*, vol. 38, pp. 555-563, 2006.

[91] U. Gbureck, T. Hölzel, I. Biermann, J. Barralet, and L. Grover, Preparation of tricalcium phosphate/calcium pyrophosphate structures via rapid prototyping, *Journal of Materials Science: Materials in Medicine,* vol. 19, pp. 1559-1563, 2008.

[92] U. Gbureck, T. Hölzel, U. Klammert, K. Würzler, F. A. Müller, and J. E. Barralet, Resorbable Dicalcium Phosphate Bone Substitutes Prepared by 3D Powder Printing, *Advanced Functional Materials*, vol. 17, pp. 3940-3945, 2007.

[93] U. Gbureck, E. Vorndran, F. A. Muller, and J. E. Barralet, Low temperature direct 3D printed bioceramics and biocomposites as drug release matrices, *Journal of Controlled Release,* vol. 122, pp. 173-180, 2007.

[94] S. J. Hollister, Porous scaffold design for tissue engineering, *Nat Mater,* vol. 4, pp. 518-524, 2005.

[95] F.E. Wiria, K.F. Leong, C.K. Chua, and Y. Liu, Poly-e-caprolactone/hydroxyapatite for tissue engineering scaffold fabrication via selective laser sintering, *Acta Biomaterialia,* vol. 3, pp. 1-12, 2007.

[96] S. Eösöly, "Mechanical Testing and Finite Element Modeling of Bioresorbable, Cellular Polymers," in *Mechanical Engineering*. vol. Masters Budapest: Budapest University of Technology and Economics, 2006.

[97] T. D. Szucs, Eosoly, S., Brabazon, D., and Olah, L., " FEA and experimental mechanical property comparison of 3DP bone scaffold geometries," in *Rapid Design, Prototyping, and Manufacture,* 8th Ed., 2007, pp. 23-30.

[98] A. W. L. Yao and Y. C. Tseng, A robust process optimization for a powder type rapid prototyper, *Rapid Prototyping Journal,* vol. 8, pp. 180-189, 2002.

[99] R. Chumnanklang, T. Panyathanmaporn, K. Sitthiseripratip, and J. Suwanprateeb, 3D printing of hydroxyapatite: Effect of binder concentration in pre-coated particle on part strength, *Materials Science and Engineering: C,* vol. 27, pp. 914-921, 2007.

[100] D. Lide, *CRC Handbook of Chemistry and Physics*: CRC Press, 1993.

[101] M. Luxner, J. Stampfl, and H. Pettermann, Finite element modeling concepts and linear analyses of 3D regular open cell structures, *Journal of Materials Science,* vol. 40, pp. 5859-5866, 2005.

[102] D. R. Carter and W. C. Hayes, The compressive behavior of bone as a two-phase porous structure, *J. Bone Joint Surg. Am.,* vol. 59, pp. 954-962, October 1, 1977 1977.

[103] N. Jinlong, Z. Zhenxi, and J. Dazong, Investigation of Phase Evolution During the Thermochemical Synthesis of Tricalcium Phosphate, *Journal of Materials Synthesis and Processing*, vol. 9, pp. 235-240, 2001.

[104] F. C. M. Driessens, "Chemistry and applied aspects of calcium orthophosphate bone cements. Concepts and clinical applications of ionic cements.," 1999.

[105] S. Takagi, L. C. Chow, and K. Ishikawa, Formation of hydroxyapatite in new calcium phosphate cements, *Biomaterials*, vol. 19, pp. 1593-1599, 1998.

[106] F. Driessens, M. Boltong, J. Planell, O. Bermúdez, M. Ginebra, and E. Fernández, A new apatitic calcium phosphate bone cement: preliminary results, *Bioceramics*, vol. 6, pp. 469-473, 1993.

Appendices

Appendix A

Reduction chamber assembly drawing

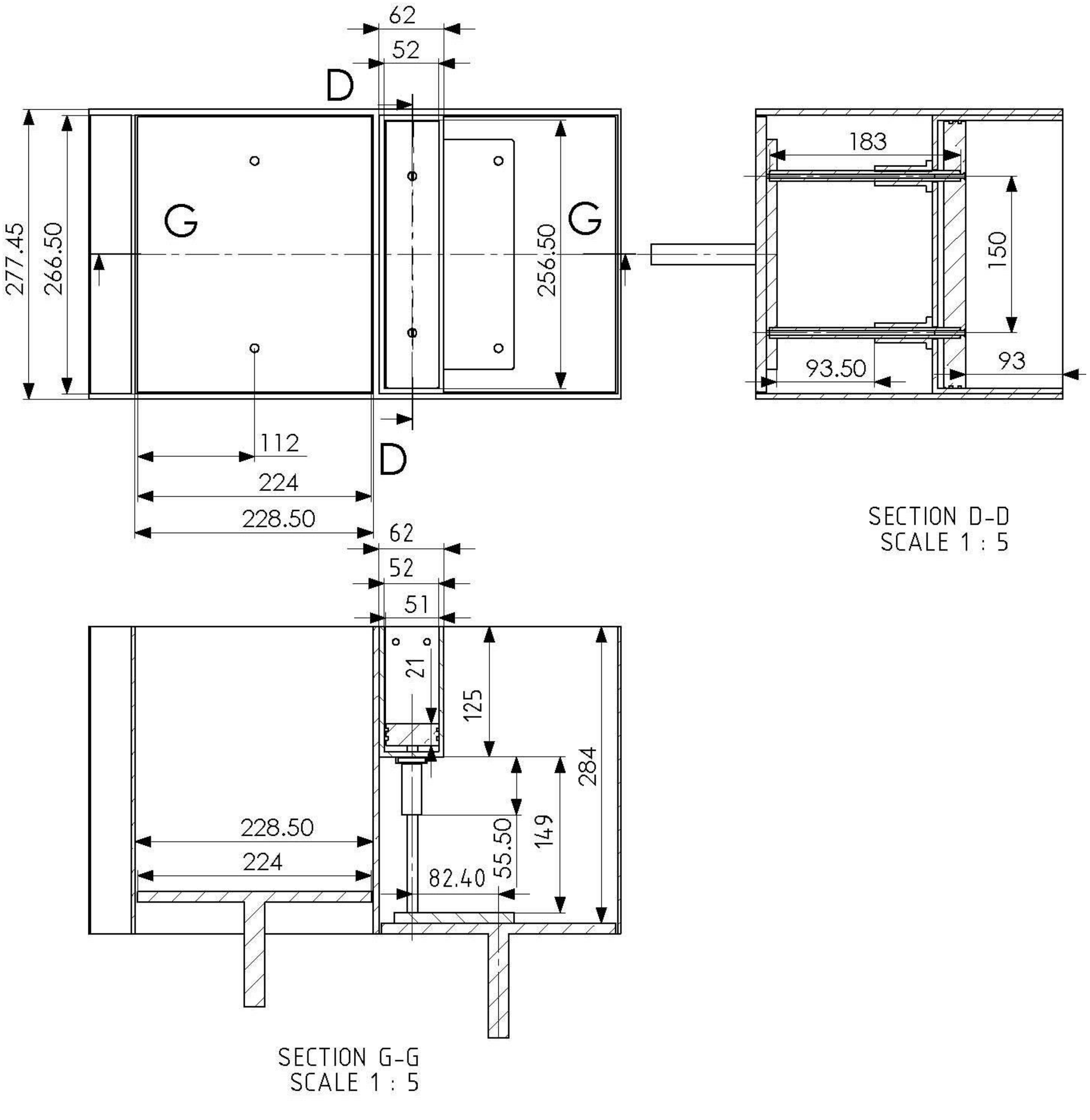

Appendix B

Stress-strain diagrams for uninfiltrated scaffold geometries. Loading direction, unit cell type are indicated next to the diagrams.

Cubic Edge	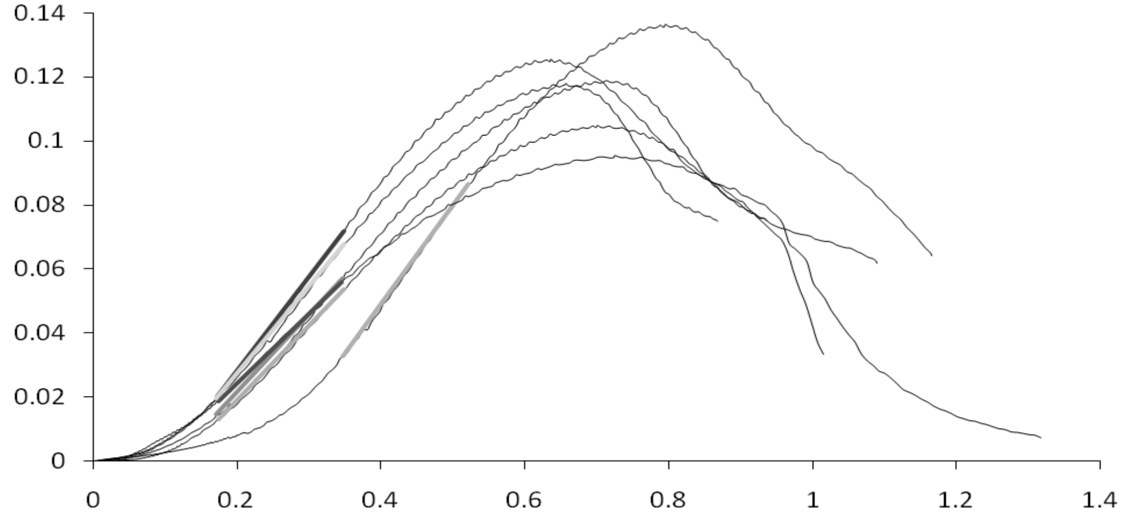
Cubic Face	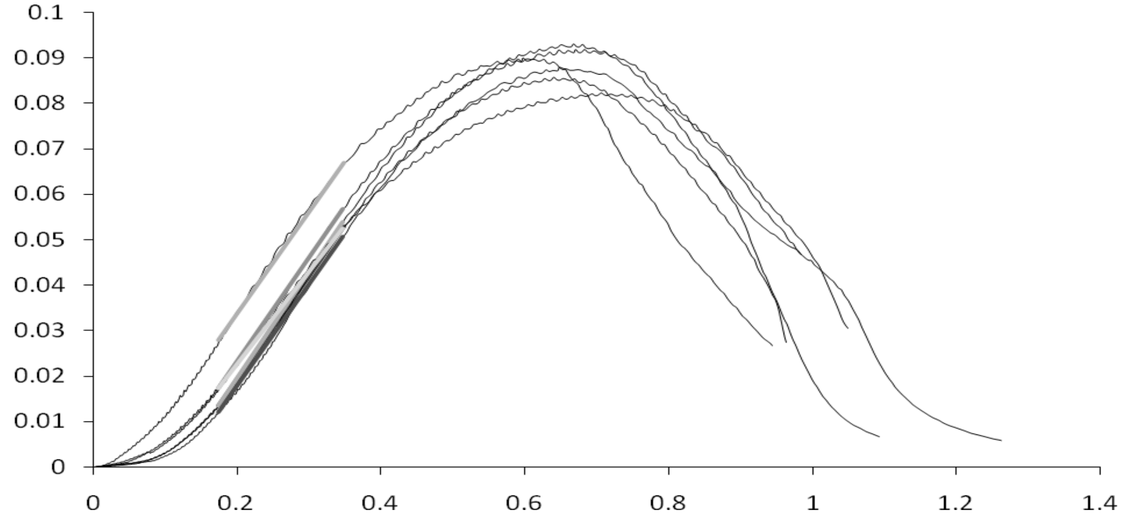
Cubic Vertex	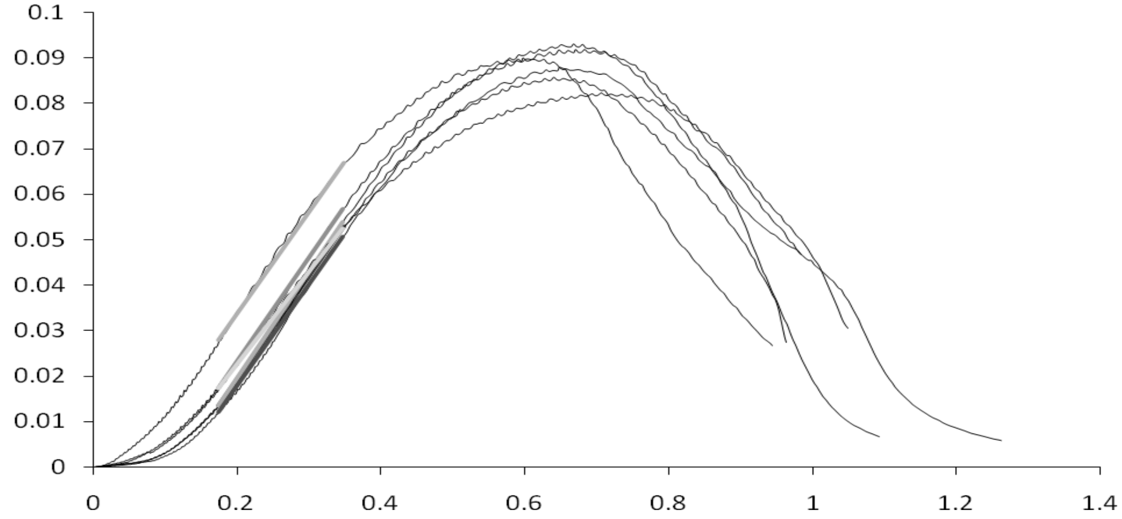

Cylindrical Edge	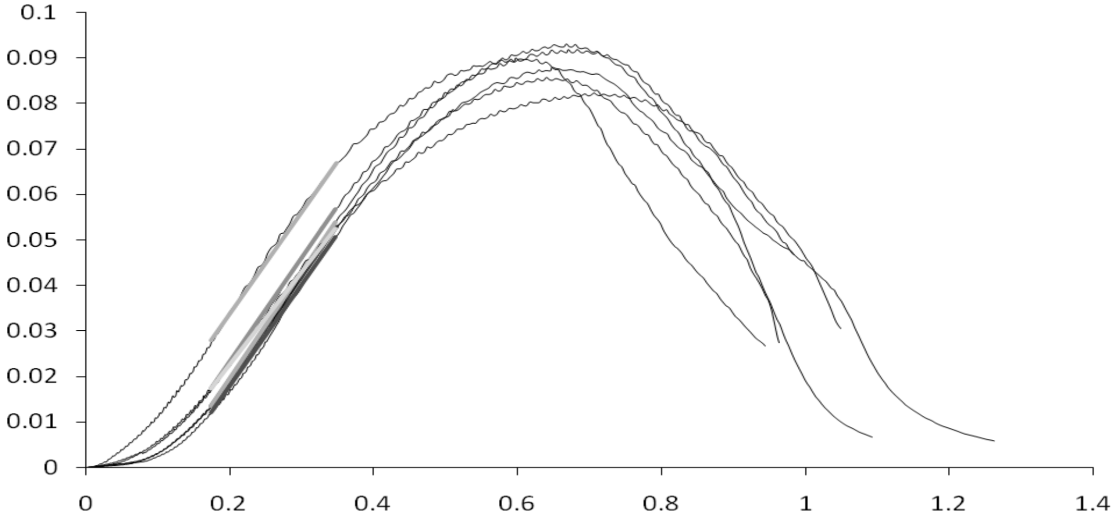
Cylindrical Face	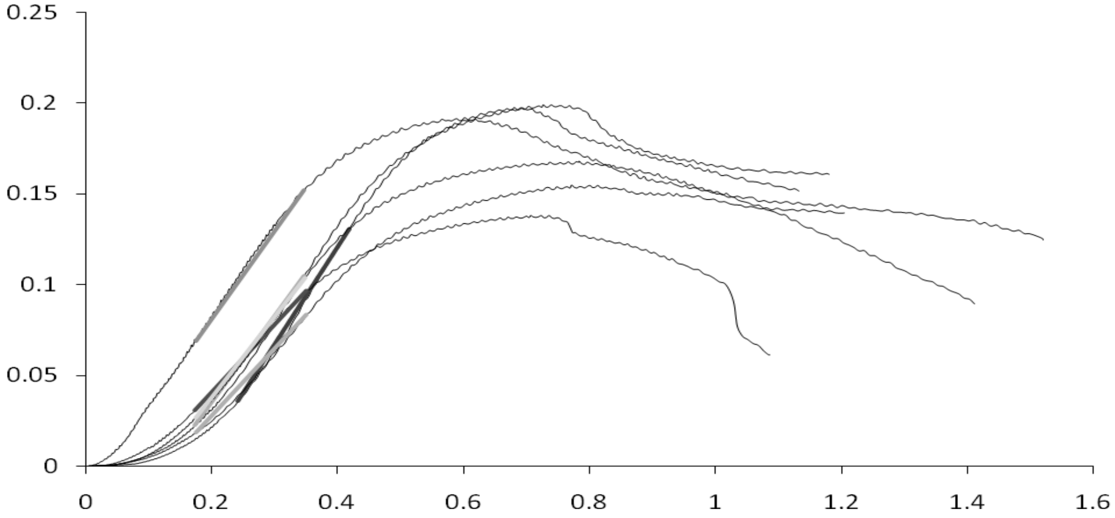
Cylindrical Vertex	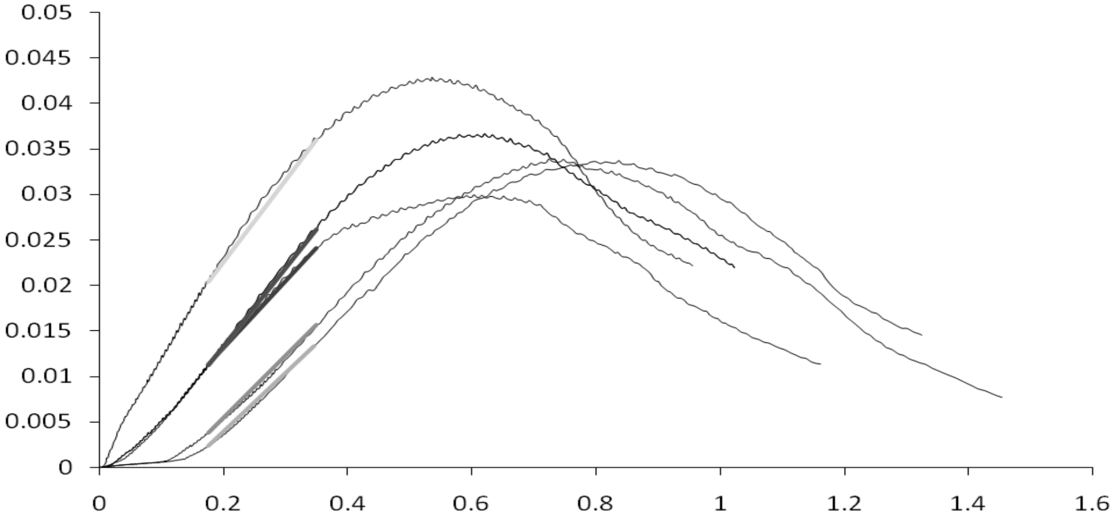

Reinforced Edge	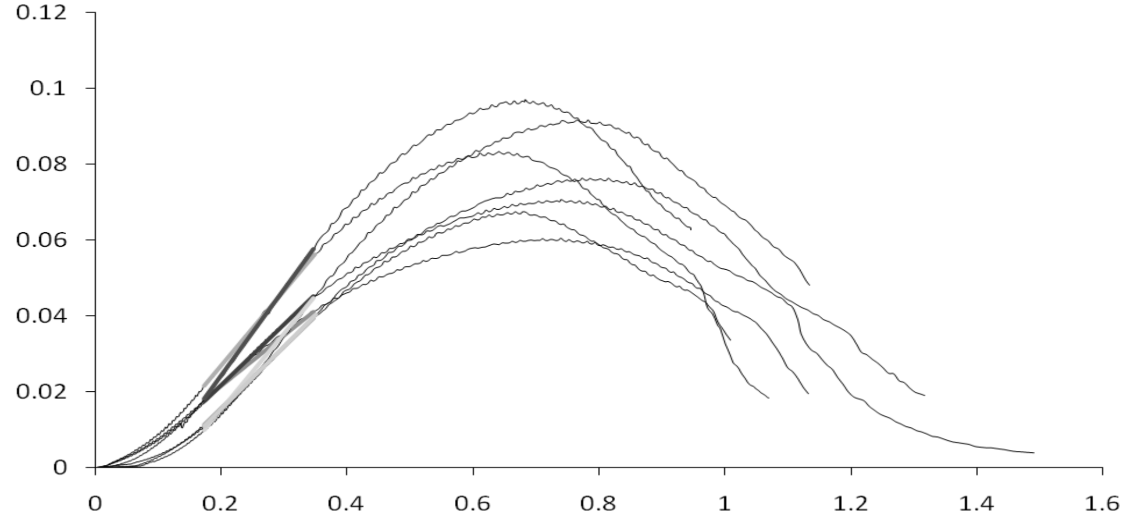
Reinforced Face	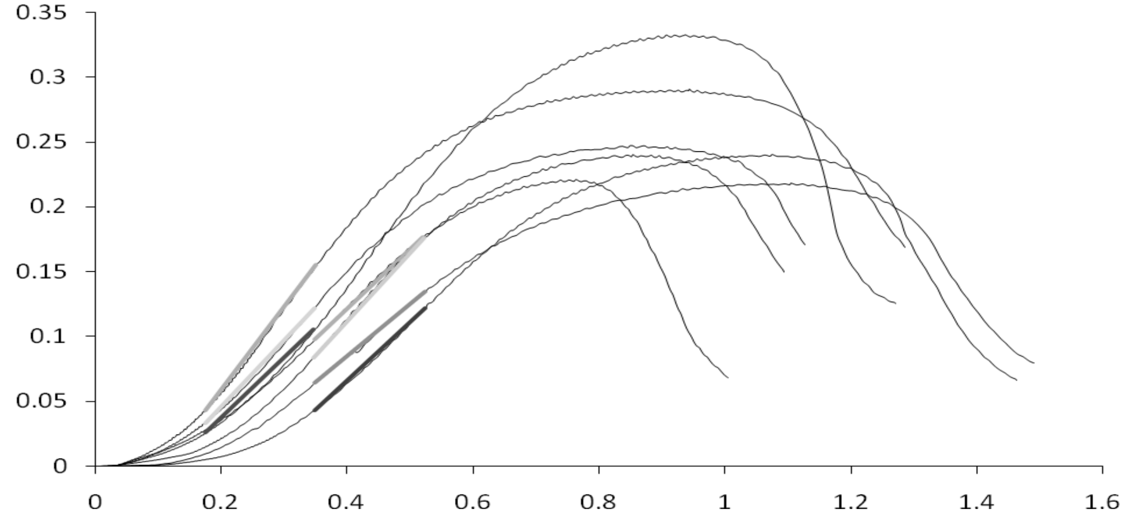
Reinforced Vertex